SIMULATING RELATIVISTIC LASER MATTER INTERACTIONS

by

NICOLA IJI

A thesis submitted to the University of Plymouth

in partial fulfillment for the degree of

DOCTOR OF PHILOSOPHY

School of Computing and Mathematics

Faculty of Science and Technology

September 2012

Nicola Iji

Simulating Relativistic Laser Matter Interactions

Abstract

With recent advances in laser technology we have seen laser intensities reach the order of 10^{22} W/cm^2, with higher intensities anticipated in the near future. This thesis concerns a classical approach to the simulation of laser matter interactions for intensities above the relativistic threshold of 10^{18} W/cm^2. A pulsed plane wave model is used to simulate the laser fields. In particular this thesis aims to determine the effect of radiation reaction on relativistic interactions as well as proposing an effective method of vacuum laser acceleration from rest. We consider the equations of motion accounting for radiative effects and present their analytic plane wave solution. A novel numerical scheme to solve the equations of motion for arbitrary field configurations is presented. The method is manifestly covariant and exact for constant fields. Radiative reaction effects are explored using the numerical method and we find that the electron gains energy from the radiation field produced by its acceleration. Methods of vacuum laser acceleration are studied and we predict a significant acceleration using two co-propagating lasers where the frequency of the two lasers differ significantly. We also look at analytic and numerical solutions of the radiation spectrum, observing an increase in oscillations in the spectrum for larger intensities. We see more photons radiated when we include radiative terms in our calculations.

Contents

List of Figures

List of Tables

Acknowledgements

First and foremost I would like to thank my supervisors Kurt Langfeld and Tom Heinzl for their unstinting support and guidance throughout my studies. Without them this thesis would not have been possible.

Special thanks to my fellow research students for freely providing inspiration and help whenever I turned to them, and for enriching my experience at the university. Sincere gratitude to all the staff in the School of Computing and Mathematics for all their help over the years and for providing such a friendly environment in which to work and study.

I would also like to express immense gratitude to the Engineering and Physical Sciences Research Council for the financial support received through their generous doctoral training grant.

Finally I would like to thank my family. In particular I thank my husband Jason and daughter Amy for their constant support and faith in me; and my parents who have always supported my education and have helped me to continue this far.

Author's declaration

At no time during the registration for the degree of Doctor of Philosophy has the author been registered for any other University award.

This study was financed with the aid of a studentship from the Engineering and Physical Sciences Research Council.

Relevant scientific seminars and conferences were attended at which work was presented. A paper has been published in a refereed journal.

Publications:

Covariant Worldline Numerics for Charge Motion with Radiation Reaction.
C. Harvey, T. Heinzl, N. Iji, and K. Langfeld.
Phys. Rev. D **83**, 076013 (2011)

Presentations given:

Impact of radiative damping on laser accelerated particles.
Rutherford Appleton Laboratory/The Guildhall, Abingdon, UK.
16 December 2011

Conferences attended:

Christmas High Power Laser Science Community User Meeting.
Rutherford Appleton Laboratory/The Guildhall, Abingdon, UK.
14 - 16 December 2011.

2nd UK - Japan Winter School in High Energy Density Science.
Edinburgh - The Royal Observatory, UK.
5 - 7 January 2011.

Word count for the main body of this thesis: 18,100

Signed: .....

Date: .....

Chapter 1

Introduction

1.1 Background and Motivation

The idea of the laser traces back to the work of Albert Einstein in 1917. His theoretical understanding of the interaction between light and matter paved the way for the first laser. In his paper "On the Quantum Mechanics of Radiation" [1], Einstein introduced the concept of stimulated emission. This is the physical principle that allows light amplification in a laser, hence its name "laser" - an acronym for Light Amplification by Stimulated Emission of Radiation. The idea of stimulated emission is closely linked to spontaneous emission whereby an excited atom or ion may spontaneously drop to its lower energy level, emitting its energy in the form of a photon in a random direction. Stimulated emission occurs when a photon with the correct wavelength passes by the excited atom, stimulating it to release its photon. The emitted photon travels in the same direction as the original photon and has the same frequency and phase. If we have a large collection of atoms then as the photons pass by the rest of the atoms, more and more photons of the same mode are emitted to join them, effectively amplifying the power of the incoming radiation [2]. One of the main components of a laser is its gain medium, which has the required properties that allow for light to be amplified by stimulated emission. Using mirrors at either end of this medium allows light to be bounced back and forth, being amplified each time. A pump source is required to excite the particles in the gain medium [3]. Despite having the basic information to build such a device, it was not until 1960 that

the first working laser was built. However since then the laser has evolved considerably. Initially described as a 'solution looking for a problem', their extreme versatility means that they are now being applied to a wide range of problems. Lasers are now being used in the areas of medicine, measurement, defence, energy and entertainment, to list just a few [4, 5].

Since the technological breakthrough of chirped pulse amplification in the mid 80s, laboratories have been able to produce lasers of higher intensities than ever before. Chirped pulse amplification is a technique for amplifying pulses to very high optical intensities while avoiding excessive pulse distortions or damage to the gain medium or any of the other optical elements. It works by stretching out the pulse in time before passing it through the gain medium, thus reducing its peak power and avoiding any damage. This stretched pulse then safely passes through the laser optics where it is amplified. Finally the pulse is temporally compressed back to its original length, allowing for ultra-high intensities [4]. Much progress has been made in the reduction of pulse duration and in the focusing of lasers over smaller areas, increasing intensities further. High power lasers have become increasingly accessible, now small enough to enable their use in many university laboratories [6].

Applications of high intensity lasers include thermonuclear fusion, fundamental science, particle acceleration and medical applications [4]. Using the laser's electromagnetic field it is possible to accelerate charged particles allowing for the idea of kilometre sized linear accelerators being replaced by table-top laser systems [7]. Schemes for laser acceleration have largely relied on plasmas, however Singh [8] claims that there are a number of advantages of vacuum acceleration over plasma acceleration. Using a vacuum avoids problems such as instabilities, which occur with laser-plasma interaction. The duration of interaction between the laser pulse and electron is potentially longer in vacuum, which in theory increases the energy gain. It is also easier to inject preaccelerated electrons in vacuum than in plasma and peak energy increases with initial electron energy. These claims suggest it would be worthwhile to investigate the potential of vacuum acceleration schemes. In addition our calculations are simplified by eliminating additional background

effects of the plasma. Despite these advantages it seems that vacuum laser acceleration has so far been unable to compete with plasma acceleration, one of the main disadvantages of working in vacuum being that a high threshold power is required for substantial acceleration [9]. However the results shown in [9, 10] suggest that direct acceleration of electrons in vacuum is within reach of the current technology and that schemes of vacuum laser acceleration are still being explored. Methods of vacuum laser acceleration and their potential for large energy gains will be explored in more detail in Chapter 3.

The advances in table-top, ultra-high intensity lasers also sparked a renewed interest in Thomson scattering, with applications such as ultra-short pulse duration X-rays [11]. Thomson scattering, the classical limit of Compton scattering, describes the scattered electromagnetic radiation by an electron that is accelerated by an external field. As laser intensities exceed the relativistic threshold of $10^{18}\mathrm{W/cm}^2$ the process becomes nonlinear. This 'nonlinear' Thomson scattering is the process that may be used for table-top X-ray sources [12].

There are currently a number of facilities for high powered lasers all over the world. The UK is world-leading in this field with its Central Laser Facility at the Rutherford Lab, in particular the Astra-Gemini and Vulcan lasers. The Plymouth Particle Theory Group is part of teams supporting experiments at Astra-Gemini and the Vulcan 10 Petawatt Upgrade Project [4]. The most powerful laser facilities, NIF (LLNL, USA) and LMJ (Bordeaux, France), are intended primarily for inertial thermonuclear fusion. Future exawatt scale facilities HiPER (High Power laser Energy Research) and ELI (Extreme Light Infrastructure) are intended for fundamental science. Laboratory astrophysics is one of the main motivations for the ELI project, which plans intensities of 10^{25} $\mathrm{W/cm}^2$ [13].

Experimentalists are now routinely able to achieve laser intensities high enough to accelerate particles close to the speed of light. We therefore turn our attention to Einstein's earlier work "On the Electrodynamics of Moving Bodies" [14] in 1905, which introduced the special theory of relativity. This theory is based on the two main principles:

- The laws of physics are the same for all observers in uniform motion relative to one another (postulate of relativity).

- The speed of light in vacuum is the same for all observers, regardless of their relative motion or the motion of the light source (postulate of the constancy of the speed of light).

These two principles require the modification of the laws of mechanics for high speed motions. Newton's laws hold as long as the velocities involved remain much smaller than the speed of light, however as particles approach the extreme velocities now achieved through acceleration by modern lasers we must use the relativistic alternative equations. We find for example that we must use the relativistic form of Newton's second law, $F = ma$, where we interpret F and a as four-vectors. We will use this relativistic version of Newton's law in Chapter 2. The form of the equations of motion needs further consideration when we account for radiation reaction (RR). It is well known that accelerated charges radiate, but problems arise when we consider that the electromagnetic fields created by an accelerated charge can act upon that same charge, effectively causing a self-interaction.

The issue of RR has a history spanning more than a century, but there has recently been a renewed interest in this subject. Lorentz [15] and Abraham [16] developed the equation of motion for an accelerated charge including the effect of the backreaction of the emitted electromagnetic radiation. This equation was put into its final covariant form by Dirac [17], giving a third-order equation for the particle trajectory. It is now known as the Lorentz-Abraham-Dirac (LAD) equation. This equation is known for its unphysical solutions explored in [18, 19] and many other texts and has been referred to as "...one of the most controversial equations in the history of physics" [20]. It has been shown [21] that the unphysical behaviour of the LAD equation, can be removed by eliminating the triple derivative term by iteration, resulting in the Landau-Lifshitz (LL) equation [22].

Radiation reaction is often neglected as it does not significantly affect the motion of a particle in most situations. The recent technological advances however have seen the problem of RR come back into the limelight. Accelerating charges in such strong fields suggests that RR (which is normally a tiny effect) may become physically relevant and, hence, experimentally observable [23]. It is therefore important that this radiative effect is accounted for when modelling the behaviour of particles in strong laser fields. The effects

of RR will be considered throughout this thesis.

Having established the motivations for this research and reviewed some of the latest developments we are now in a position to begin modelling the laser matter interactions of interest. However before we begin to look into the equations of motion in any detail we must first decide upon how our laser fields will be modelled. The next section therefore briefly discusses the properties of laser light and how they may be incorporated into a model for the laser fields.

1.2 Modelling a Laser Beam

Laser light differs from normal light due to its unique properties [3]:

- Monochromaticity - lasers emit only a very narrow range of wavelengths.
- Directionality - lasers can emit light in one direction, which spreads only very little with distance. However, all laser beams eventually diverge as they move through space.
- Coherence - lasers have a high degree of spatial and temporal coherence.

In most cases, a laser emits electromagnetic radiation in the form of a laser beam. A laser beam can be emitted continuously as an infinite wave or in the form of a fast sequence of pulses. The latter allows for extremely high peak powers. The electric and magnetic field components of a laser field oscillate in phase perpendicular to each other and perpendicular to the direction of energy propagation. A laser may be linearly or circularly polarised (or something in between - elliptic polarisation) [2]. To simulate the properties of the laser we must incorporate the shape of the laser field, its strength and how it is polarised into our description of the field. Our model will therefore consist of a shape function and a strength parameter, as well as polarisation and propagation vectors.

Plane wave models are commonly used when modelling laser-electron interactions since they are simple enough to allow for the analytic calculation of many of the physical behaviours associated with such interactions, but also provide a reasonable model for the laser field in certain regimes [24]. The simplest choice of the laser field model would be

to use an infinite plane wave. Fig 1.1a shows the pulse shape as a function of the laser phase for an infinite plane wave. To create a pulsed plane wave a suitable envelope is chosen. Fig 1.1b shows the effect of using a Gaussian envelope, although similar alternatives may be used. This is still unphysical due to its infinite transverse extent. Gaussian beams provide a realistic model for a laser beam since they are restricted by a beam radius. Gaussian functions are used in [25, 26] for example to model a laser beam. Fig 1.1c shows the beam radius as a function of the position in the direction of propagation; w_0 is the waist size which is the beam diameter at the point of minimum radius. We obtain plane wave fields in the limit where the beam waist becomes large.

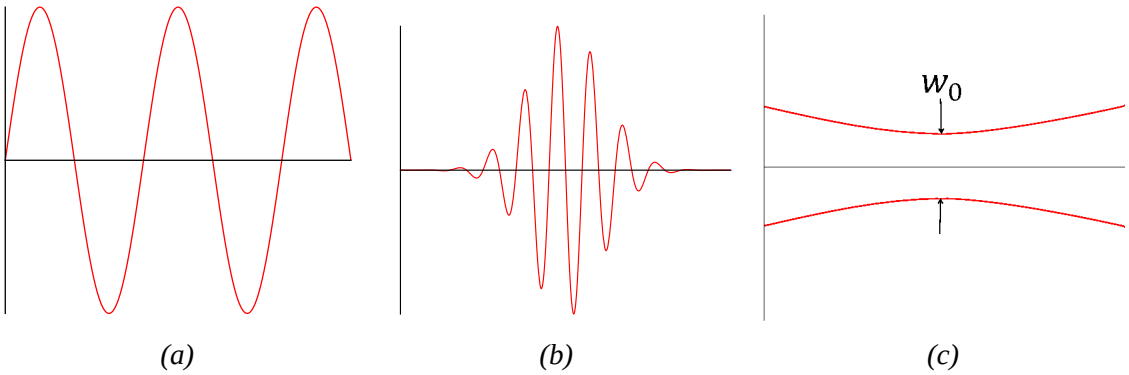

Figure 1.1: Models of a laser beam; (a) Infinite plane wave, (b) Pulsed plane wave using a Gaussian envelope, and (c) Beam radius as a function of position in the direction of propagation; w_0 is the waist size.

As our model becomes more realistic it also becomes more complex. For this reason for the majority of this thesis a pulsed plane wave model will be used. Despite the addition of a pulse envelope to the infinite plane wave model, its null field properties still allow for the analytic calculations required. We shall see in Chapter 2 that the analytical solution to the LL equation is known for plane waves; this can be used as a benchmark for our numerical codes. However, we must take into account the assumptions made by using a pulsed plane wave model.

To model the intensity of our laser field we use the laser strength parameter a_0, defined by

$$a_0 = \frac{e\,E\,\lambda\!\!\!^{-}_L}{m\,c^2} \sim I^{1/2}\,, \tag{1.1}$$

where E is the amplitude of the laser field, e is the electron charge, m is the electron mass and $\lambda\!\!\!^{-}_L = c/\omega$ is the laser wavelength. This strength parameter is therefore the energy gain of the electron per laser wavelength and a_0^2 is proportional to the laser intensity. When a_0 is greater than 1 it will describe relativistic behaviour. To give an idea of the magnitude of a_0 for intense lasers, the current record for an optical laser is of the order of 10^2 (intensity of the order 10^{22} W/cm^2) [27]. The laser system of the Berkeley Lab Laser Accelerator (BELLA) in the U.S., has the potential to achieve $a_0 = 280$ [28]. We will be using the values $a_0 = 10$ for an XFEL and $a_0 = 3000$ for an optical laser (the kind of a_0 value envisaged for ELI) throughout this thesis.

Now that we have decided upon how we shall model our laser field we are in a position to study the behaviour of particles in such a field. The structure of this thesis is outlined in the following section.

1.3 Organisation of the Thesis

The topics covered in this thesis fall nicely under three main headings: motion, vacuum acceleration and radiation. Chapter 2 explores the equations of motion and methods of their solution. Chapters 3 and 4 apply these results to acceleration and radiation.

We begin in Chapter 2 by considering the equations of motion in both their 3-dimensional and covariant forms. The covariant Maxwell equations and relativistic Newton's second law are derived using the action principle. We then include radiative effects in our equations and review the issues that occur when including radiative terms. The equations of motion are solved analytically for a pulsed plane wave and a numerical method is introduced, which can solve the equations in arbitrary fields. The method is tested using constant fields and the analytic plane wave solution; it is then extended to a higher order of accuracy. This method is used to study the impact of radiation reaction on the motion of a charged particle in a laser field.

Having established methods for calculating the motion of charged particles, we look at the application of these results. Chapter 3 uses the methods and equations introduced in Chapter 2 to explore laser acceleration of charged particles in vacuum. The methods

of acceleration considered in this chapter are short pulse acceleration, using a chain of pulses to accelerate a charge, searching for an optimum pulse shape and lastly using two co-propagating lasers to get a net acceleration.

Chapter 4 looks at the radiation produced by the accelerated charged particles. The radiation spectrum is calculated for crossed fields analytically. We consider the spectrum of radiation as a method of tracing RR in experiments. Numerical integration is used to calculate the spectrum for a pulsed plane wave initially without RR. The effect of increasing a_0 is then explored. The oscillations observed for large a_0 prompt us to check for chaotic behaviour in the spectrum. Then having ruled this out we consider the impact of RR on the spectrum of radiation.

Highlights of the research are summarised and discussed in Chapter 5. Possible areas of future work are also considered in this final chapter.

Chapter 2

Motion

This chapter is devoted to exploring the motion of charged particles in electromagnetic fields. We first consider the foundations of classical electrodynamics in the familiar 3-dimensional notation and then rederive the equations of motion using a covariant formalism. Both analytic and numerical methods are used to solve these equations and these methods shall be used in the subsequent chapters to investigate acceleration and radiation. In this chapter we shall also introduce a pulsed plane wave model for our laser field, the structure of which will again be used in the remaining chapters. It is well known that accelerating charges radiate. The effect of this electromagnetic radiation on the motion of the charges will be explored in Section 2.4.

2.1 From Maxwell's Equations to Particle Motion

We begin our discussion on motion by stating Maxwell's equations and the Lorentz force law, which together form the foundations of classical electrodynamics. There exists a set of four partial differential equations describing the behavior of electric and magnetic fields; how they relate to their sources, charge density ρ and current density $\mathbf{j}$, and how they develop with time. This set of fundamental equations is known as Maxwell's equa-

tions, which in Heaviside-Lorentz units read as follows,

$$\begin{aligned} \nabla \cdot \mathbf{E}(\mathbf{x},t) &= \rho(\mathbf{x},t), \\ \nabla \times \mathbf{B}(\mathbf{x},t) - \frac{\partial \mathbf{E}(\mathbf{x},t)}{c\,\partial t} &= \frac{1}{c}\mathbf{j}(\mathbf{x},t), \\ \nabla \times \mathbf{E}(\mathbf{x},t) + \frac{\partial \mathbf{B}(\mathbf{x},t)}{c\,\partial t} &= 0, \\ \nabla \cdot \mathbf{B}(\mathbf{x},t) &= 0, \end{aligned} \tag{2.1}$$

where $\mathbf{E}(\mathbf{x},t)$ is the electric field and $\mathbf{B}(\mathbf{x},t)$ is the magnetic field, $\mathbf{x}$ and t denote the location and time respectively, and c, the speed of light is a universal constant ($c =$ 299792458 m/s). The continuity equation for charge density and current density follows from combining $\partial/\partial t$ of the first of Maxwell's equations with the divergence of the second

$$\frac{\partial \rho(\mathbf{x},t)}{\partial t} + \nabla \cdot \mathbf{j}(\mathbf{x},t) = 0\ . \tag{2.2}$$

The Lorentz force equation gives the force acting on a charge e in the presence of electromagnetic fields:

$$\mathbf{F}_L(\mathbf{x},t) = e\mathbf{E}(\mathbf{x},t) + \frac{e}{c}\mathbf{v}(t) \times \mathbf{B}(\mathbf{x},t), \tag{2.3}$$

where $\mathbf{F}_L$ is the Lorentz force and $\mathbf{v}$ denotes the particle's velocity. For a single charge e the rate of doing work (the power) by external electromagnetic fields is $\mathbf{v} \cdot \mathbf{F}_L = e\mathbf{v} \cdot \mathbf{E}$; the magnetic field does not contribute since it is perpendicular to the velocity.

2.1.1 Covariant Formulation of Classical Electrodynamics

The equations above show the equations of motion and Maxwell's equations in their 3-dimensional form, however it is convenient to use an explicitly covariant formalism based on four-vectors so that all equations are valid in any reference frame. Let us first introduce the four-velocity u^μ, $\mu = 0...3$, a contravariant vector of Minkowski space. Its covariant components can be found using the Minkowski metric $g_{\mu\nu}$:

$$u_\mu = g_{\mu\nu}u^\nu, \quad g = diag(1,-1,-1,-1). \tag{2.4}$$

We denote the position of the particle by x^μ, $x^0 = ct$, $x^i = (\mathbf{x})^i$. The infinitesimal line element (distance) is

$$ds = \sqrt{dx_\mu dx^\mu} = \sqrt{1 - \frac{1}{c^2}\left(\frac{d\mathbf{x}}{dt}\right)^2}\, c\, dt \equiv c\, d\tau\ , \tag{2.5}$$

where τ is the proper time. $d\tau$ is Lorentz invariant and is equal to the particle's time in its rest frame where $d\mathbf{x}/dt = 0$. It will be useful to introduce the Lorentz gamma factor, which is defined as

$$\gamma = \frac{1}{\sqrt{1 - \frac{1}{c^2}\left(\frac{d\mathbf{x}}{dt}\right)^2}} = \frac{1}{\sqrt{1-\beta^2}} = \frac{dt}{d\tau}, \tag{2.6}$$

where β is the ratio of the velocity of the particle to the speed of light. The four-velocity and current density are given by

$$u^\mu(\tau) = \frac{dx^\mu}{d\tau}, \quad j^\mu(x) = e\int d\tau\, u^\mu(\tau)\delta^4(x - x(\tau))\ , \tag{2.7}$$

where the charge density and current density have been combined to form the 4-vector $j^\mu = (c\rho, \mathbf{j})$. The continuity equation (2.2) takes the covariant form

$$\partial_\mu j^\mu = 0, \tag{2.8}$$

where

$$\partial_\mu \equiv \frac{\partial}{\partial x^\mu} = \left(\frac{\partial}{\partial x^0}, \nabla\right). \tag{2.9}$$

For what follows we will need to introduce the four-potential A_μ, of an electromagnetic field, which characterises the properties of the field. The three space components of the four-vector A^μ form the vector potential of the field $\mathbf{A}$ and the time component is the scalar potential $A^0 = \Phi$, i.e. $A^\mu = (\Phi, \mathbf{A})$. The electric and magnetic fields relate to A^μ via

$$\mathbf{E} = -\frac{1}{c}\frac{\partial \mathbf{A}}{\partial t} - \nabla\Phi\ ; \quad \mathbf{B} = \nabla \times \mathbf{A}\ . \tag{2.10}$$

We will also be working with the electromagnetic field tensor, $F_{\mu\nu}$, which is related to the

four-potential via

$$F_{\mu\nu} = \frac{\partial A_\nu}{\partial x^\mu} - \frac{\partial A_\mu}{\partial x^\nu} \equiv \partial_\mu A_\nu - \partial_\nu A_\mu \ . \tag{2.11}$$

In order to rewrite the equations of motion in their four-dimensional form, we start from the principle of least action. This principle states that for each mechanical system the motion between two points is such that the action S, an integral describing the overall motion of the system, is minimised, i.e. $\delta S = 0$. The action function for a system consisting of an electromagnetic field as well as the particles located in it must contain three parts:

- the action for the field in the absence of charges,

$$S_f = -\frac{1}{4}\int d^4x F_{\mu\nu}F^{\mu\nu} \ ; \tag{2.12}$$

- the action depending only on the particles (for a single free particle),

$$S_p = -mc^2 \int d\tau \ ; \tag{2.13}$$

- the interaction between the particles and the field (for a single particle),

$$S_i = -\frac{e}{c}\int dx^\mu A_\mu \ . \tag{2.14}$$

Together these make up the action for the whole system

$$S = -mc^2 \int d\tau - \frac{e}{c}\int dx^\mu A_\mu - \frac{1}{4}\int d^4x F_{\mu\nu}F^{\mu\nu} \ . \tag{2.15}$$

This may be rewritten in its alternative version in "field language" by noting that $\int dx^\mu A_\mu = \int d\tau u_\mu A^\mu$ and using $j^\mu(x) = e\int d\tau \ u^\mu(\tau)\delta^4(x - x(\tau))$. We have

$$S = -mc^2 \int d\tau - \frac{1}{c}\int d^4x j^\mu A_\mu - \frac{1}{4}\int d^4x F_{\mu\nu}F^{\mu\nu} \ . \tag{2.16}$$

To find the equations of motion we assume that the field is given and vary the trajectory. Noting that the field term variation is zero, we find according to the principle of least

action that

$$\delta S = -\int \left(m\frac{dx_\mu d\delta x^\mu}{d\tau} + \frac{e}{c}A_\mu d\delta x^\mu + \frac{e}{c}\delta A_\mu dx^\mu \right) = 0 \ , \tag{2.17}$$

where we have used $c\, d\tau = \sqrt{dx_\mu dx^\mu}$. Following careful manipulation of the expression detailed in [22], we obtain

$$\int \left[m\frac{du_\mu}{d\tau} - \frac{e}{c}\left(\frac{\partial A_\nu}{\partial x^\mu} - \frac{\partial A_\mu}{\partial x^\nu} \right) u^\nu \right] \delta x^\mu d\tau \ . \tag{2.18}$$

It follows that the integrand must be zero, hence

$$m\frac{du_\mu}{d\tau} = \frac{e}{c}\left(\frac{\partial A_\nu}{\partial x^\mu} - \frac{\partial A_\mu}{\partial x^\nu} \right) u^\nu = 0 \ . \tag{2.19}$$

Further simplification results from replacing the term in brackets with the electromagnetic field tensor according to (2.11). The equations of motion in their four-dimensional form may therefore be written as

$$m\frac{du^\mu}{d\tau} = m\dot{u}^\mu = \frac{e}{c}F^{\mu\nu}u_\nu \equiv F^\mu \ , \tag{2.20}$$

where the Lorentz four-force F^μ appears on the right-hand side and where, from now on, the over-dot is used to denote derivatives with respect to the proper time τ. By multiplying (2.20) by u_μ we find that $u_\mu \dot{u}^\mu = 0$, which implies that $d(u_\mu u^\mu)/d\tau = 0$. Therefore $u_\mu u^\mu = u^2$ is a constant which can be set in relation to the speed of light, using (2.5), as $u^2 = c^2$. This implies the on-shell condition $p^2 = m^2\, c^2$, where $p^\mu = mu^\mu$ is the four-momentum of the particle.

By substituting the values $A_\mu = (\Phi, -\mathbf{A})$ into (2.11), according to the definitions of (2.10) we see that $F^{\mu\nu}$ may be expressed in terms of $\mathbf{E}$ and $\mathbf{B}$ as follows

$$F_{0i}(x) = -F_{i0}(x) = E_i(x), \quad F_{ik}(x) = -\varepsilon_{ikm}B_m(x) \ . \tag{2.21}$$

Converting (2.20) back to three-dimensional notation we obtain (2.3) from the three space components and the work done ($e\mathbf{v}\cdot\mathbf{E}$) from the time component.

Similarly Maxwell's equations can be written in covariant form by two tensor equations. The homogeneous Maxwell equations may be rewritten using the definition of the electromagnetic field tensor as

$$\frac{\partial F_{\mu\nu}}{\partial x^{\rho}} + \frac{\partial F_{\nu\rho}}{\partial x^{\mu}} + \frac{\partial F_{\rho\mu}}{\partial x^{\nu}} = 0 \,, \tag{2.22}$$

or in its compact form

$$\partial^{\mu} \varepsilon_{\mu\nu\rho\sigma} F^{\rho\sigma} = 0 \quad \Rightarrow \quad \partial_{\mu} \widetilde{F}^{\mu\nu} = 0 \,, \tag{2.23}$$

where $\varepsilon_{\mu\nu\rho\sigma}$ is the Levi-Civita symbol and $\widetilde{F}^{\mu\nu}$ is the dual field strength tensor $\widetilde{F}^{\mu\nu} = \varepsilon^{\mu\nu\rho\sigma} F_{\rho\sigma}/2$. This equation can easily be shown to correspond to the homogeneous Maxwell equations by using (2.21).

As for the inhomogeneous pair of Maxwell equations, we consider again the principle of least action. Now we assume the motion of the charge to be given and vary only the potentials. Therefore there is no variation in the particle term of (2.16) and we do not vary j^{μ} in the interaction term. According to the principle of least action we have

$$\delta S = -\int \left(\frac{1}{c} j^{\mu} \delta A_{\mu} + \frac{1}{2} F^{\mu\nu} \delta F_{\mu\nu} \right) d^4x = 0 \,, \tag{2.24}$$

where the result $F^{\mu\nu} \delta F_{\mu\nu} = F_{\mu\nu} \delta F^{\mu\nu}$ has been used. Again following [22] we obtain

$$\int \left(\frac{1}{c} j^{\mu} + \frac{\partial F^{\mu\nu}}{\partial x^{\nu}} \right) \delta A_{\mu} d^4x = 0. \tag{2.25}$$

Hence the two inhomogeneous equations of motion may be written as

$$\frac{\partial F^{\mu\nu}}{\partial x^{\nu}} = -\frac{j^{\mu}}{c} \quad \Rightarrow \quad \partial_{\mu} F^{\mu\nu} = \frac{j^{\nu}}{c} \,. \tag{2.26}$$

This when written in its three-dimensional form gives the remaining equations in (2.1). With the Lorentz gauge condition ($\partial_{\mu} A^{\mu} = 0$) this becomes the inhomogeneous wave

equation

$$\Box A^{\mu} = \frac{j^{\mu}}{c} \ , \tag{2.27}$$

where $\Box$ is the d'Alembert operator. Solving this equation gives the Liénard-Wiechert potentials, that show us that accelerating particles radiate. Following [29] we define A^{in}_{μ} and A^{out}_{μ} to be the incoming and outgoing radiation respectively. The formula for the energy radiated is given by

$$P^{rad}_{\mu} = P_{\mu}(A^{out}) - P_{\mu}(A^{in}) \ , \tag{2.28}$$

which is found in [29] to be

$$P^{\mu}_{rad} = \frac{2}{3}\frac{e^2}{4\pi c^5}\int d\tau \dot{u}_{\lambda}\dot{u}^{\lambda}u^{\mu} \ . \tag{2.29}$$

The integrand may be considered the momentum four-vector rate of radiation, hence

$$\frac{dP^{\mu}_{rad}}{d\tau} = \frac{2}{3}\frac{e^2}{4\pi c^5}\dot{u}_{\lambda}\dot{u}^{\lambda}u^{\mu} = \frac{2}{3}\frac{e^2}{4\pi c^5}a_{\lambda}a^{\lambda}u^{\mu} \ , \tag{2.30}$$

where $\dot{u}^{\mu} = a^{\mu}$ is the acceleration four-vector. The energy rate of radiation or radiated power is proportional to $\dot{P}^{rad}_{\mu} \cdot u^{\mu}$ [19]. It may be expressed using the zero component of $P^{\mu}_{rad} = (W_{rad}/c, \mathbf{P}_{rad})$, where W_{rad} is the radiated energy,

$$P = \frac{dW_{rad}}{dt} = \frac{dP^0_{rad}c}{\gamma d\tau} = \frac{2}{3}\frac{e^2}{4\pi c^5}a_{\lambda}a^{\lambda}\frac{u^0 c}{\gamma} = \frac{2}{3}\frac{e^2}{4\pi c^3}a_{\lambda}a^{\lambda} \ . \tag{2.31}$$

This is the relativistic generalisation of the famous non-relativistic Larmor formula which expresses the radiated power P as

$$P = \frac{2}{3}\frac{e^2}{4\pi c^3}\mathbf{a}^2. \tag{2.32}$$

It is now clear that radiation is proportional to the acceleration squared. There is no radiation if $a = 0$. We are considering a charged particle acted on by an external field.

Since the particle is accelerated it will emit radiation at a rate proportional to the square of this acceleration. The emitted radiation changes the external field, which modifies the motion of the particle - a 'backreaction' on the particle. To account for the effect of the backreaction on the motion of the particle we must modify the equations of motion.

2.1.2 The Relativistic Equations of Motion with Radiation Reaction

We have established that an accelerated charge radiates; this radiation exerts a force back on the charge. We will call this force F^{μ}_{rad}, the radiation reaction force and use the associated field strength tensor $F^{\mu\nu}_{rad}$ such that $F^{\mu}_{rad} = eF^{\mu\nu}_{rad}u_{\nu}/c$. To ensure energy conservation, the work done by the RR force on the particle must be equal and opposite to the energy radiated [30]. Taking account of RR, we replace $F^{\mu\nu}$ in (2.20) with $F^{\mu\nu}_{\text{in}} + F^{\mu\nu}_{\text{rad}}$ and after a mass renormalisation (outlined in [29]) we obtain the LAD equation in the form first presented by Dirac [17].

$$m\dot{u}^{\mu} = \frac{e}{c}F^{\mu\nu}_{\text{in}}u_{\nu} - \frac{2}{3}\frac{e^2}{4\pi c^5}(u^{\mu}\ddot{u}^{\nu} - u^{\nu}\ddot{u}^{\mu})\,u_{\nu} \tag{2.33}$$

By taking the second derivative of u^2, we see that $\ddot{u}\cdot u = -\dot{u}\cdot\dot{u}$, and hence (2.33) may be equivalently written as

$$m\dot{u}^{\mu} = \frac{e}{c}F^{\mu\nu}u_{\nu} + \frac{2}{3}\frac{e^2}{4\pi c^3}(\ddot{u}^{\mu} + \dot{u}^2\,u^{\mu}/c^2)\,, \tag{2.34}$$

where we now omit the subscript "in". Notice the $\ddot{u} \equiv \dddot{x}$ term, which means we have a third-order differential equation. This causes problems such as runaway solutions [29], where even with a constant force we end up with the acceleration growing exponentially with time. One method of dealing with this problem is to choose the initial conditions such that the runaways are eliminated. However this leads to another issue, pre-acceleration, where there is acceleration before the force sets in. If the higher order terms are replaced with the Lorentz term in the equation of motion, i.e. $\dot{u}^{\mu} = e\,F^{\mu\nu}u_{\nu}/mc$ and $\ddot{u}^{\mu} = e\,\dot{F}^{\mu\nu}u_{\nu}/mc + e^2\,F^{\mu\alpha}F_{\alpha}{}^{\nu}u_{\nu}/m^2c^2$, we end up with the much better behaved

Landau-Lifshitz equation [22]:

$$m\dot{u}^{\mu} = \frac{e}{c}F^{\mu\nu}u_{\nu} + \frac{2}{3}\frac{e^2}{4\pi c^3}\left\{\frac{e}{mc}\dot{F}^{\mu\nu}u_{\nu} + \frac{e^2}{m^2c^2}F^{\mu\alpha}F_{\alpha}{}^{\nu}u_{\nu} - \frac{e^2}{m^2c^4}u_{\alpha}F^{\alpha\nu}F_{\nu}{}^{\beta}u_{\beta}\,u^{\mu}\right\} . \tag{2.35}$$

The LAD and LL equations may be simplified by using the projection $\mathbb{P}^{\mu\nu} = g^{\mu\nu} - u^{\mu}u^{\nu}/c^2$ [31]. The LAD equation becomes

$$m\dot{u} = F_L + \tau_0 \mathbb{P} m\ddot{u} , \tag{2.36}$$

where $\tau_0 = (2/3)\, e^2/4\pi mc^3$. Using $m\ddot{u} = \dot{F}_L + O(\tau_0)$ from the LAD equation we replace $m\ddot{u}$ and obtain the LL equation in its simplified form

$$m\dot{u} = F_L + \tau_0 \mathbb{P}\dot{F}_L . \tag{2.37}$$

This makes it much clearer to see how we get the LL equation from the LAD equation. For the study of laser-matter interactions it will be useful to use dimensionless variables, particularly for the numerical approach which will follow, and to adopt natural units, $c = 1$. We will assume that our laser beam is described by a light-like wave vector $k = (\omega, \mathbf{k})$, $k^2 = \omega^2 - \mathbf{k}^2 = 0$, with ω and $\mathbf{k}$ being lab frame coordinates. To combine this with the electron motion we follow Wald [32] and define a frequency by dotting k into the initial velocity, u_0,

$$\Omega_0 \equiv k \cdot u_0 . \tag{2.38}$$

If the particle is initially at rest we have $u_0^{\mu} = \delta^{\mu}_0$ and $\Omega_0 = \omega_0$, where ω_0 denotes the laser frequency in the initial rest frame. We also define a dimensionless proper time, $s \equiv \Omega_0 \tau$ and denote s-derivatives by an over-dot. Rescaling $eF^{\mu\nu}/me\Omega_0 \to F^{\mu\nu}$ makes $F^{\mu\nu}$ dimensionless. In this new notation we use the following invariant definition for a_0, which was introduced in (1.1),

$$a_0^2 = u_{0\mu}\langle F^{\mu\alpha}F_{\alpha}{}^{\nu}\rangle u_{0\nu} , \tag{2.39}$$

where the brackets $\langle \ldots \rangle$ at this point denote a *typical* value such as the root-mean-square (proper time average) or the amplitude (cycle maximum). This implies that $F^{\mu\nu}$ is proportional to a_0 (the strength parameter) which will be made explicit in Section 2.2. We define the dimensionless energy variable v_0 and the effective coupling parameter r_0 by

$$v_0 \equiv \frac{\Omega_0}{m} , \tag{2.40}$$

$$r_0 \equiv \frac{2}{3}\alpha v_0 , \tag{2.41}$$

where $\alpha = e^2/4\pi = 1/137$ is the fine structure constant. Finally we introduce a dimensionless energy density $w = u_\mu F^{\mu\alpha} F_\alpha{}^\nu u_\nu$. We may then rewrite the LAD and LL equations in compact form:

$$\begin{aligned} \dot{u}^\mu &= F^{\mu\nu}\, u_\nu + r_0(\ddot{u}^\mu + \dot{u}^2 u^\mu) , \\ \dot{u}^\mu &= F^{\mu\nu}\, u_\nu + r_0(\dot{F}^{\mu\nu} + F^{\mu\alpha}F_\alpha{}^\nu - w\, g^{\mu\nu})u_\nu . \end{aligned} \tag{2.42}$$

The LL equation is an expansion in powers of r_0 (or α), with coefficients being proportional to powers of field strength, hence a_0. The leading order (r_0^0) is the Lorentz term while the LL term is $O(r_0)$. By solving the LL equation for a given external field we may study the motion of a charged particle subject to that field.

2.2 Analytic Solution of the Equations of Motion

We may solve the LL equation in order to find the four-velocity and also the trajectory of a particle in a laser field. We model the laser beam by a plane wave. In this case the field strength, $F^{\mu\nu} = F^{\mu\nu}(k\cdot x)$, is assumed to be transverse, $k_\mu F^{\mu\nu} = 0$. The null-plane properties of the plane wave allow for an analytic solution, which can be used as a benchmark for the numerical results. Defining $\phi = k\cdot x$, we will consider the field strength of the form

$$F^{\mu\nu}(\phi) = a_0\, f_i(\phi)\, f_i^{\mu\nu} , \qquad f_i^{\mu\nu} = n^\mu \varepsilon_i^\nu - n^\nu \varepsilon_i^\mu . \tag{2.43}$$

where a_0 is the strength parameter. We specialise to linear polarisation,

$$f_2 = 0, \qquad f_1 \equiv f, \qquad n^\mu = (1, \hat{\mathbf{z}}), \qquad \varepsilon_1^\mu = (0, \hat{\mathbf{x}}) \,, \tag{2.44}$$

and choose a pulse with a Gaussian envelope,

$$f(\phi) \equiv -\exp\left\{-\frac{(\phi-\phi_0)^2}{N^2}\right\} \sin(\phi) \,, \tag{2.45}$$

where ϕ_0 denotes the centre of the pulse and N is the half-width of the pulse. N also controls the number of cycles within the pulse as we shall see in Chapter 3. If we plug (2.43) into (2.42) we may rewrite the LL equation in the following form

$$\dot{u}^\mu \quad = \quad \left[a_0 f \, f^\mu{}_\nu + r_0 a_0 \, u_\parallel \left\{ f' \, f^\mu{}_\nu + a_0 f^2 (n^\mu u_\nu - n_\nu u^\mu) \right\}\right] \, u^\nu \,, \tag{2.46}$$

where $u_\parallel = n \cdot u$ and where the prime denotes differentiation with respect to ϕ. If we take the scalar product with n and use the fact that $n_\mu \, f^\mu{}_\nu = 0$ we find that

$$\dot{u}_\parallel = -r_0 a_0^2 f^2(\phi) u_\parallel^3 \,. \tag{2.47}$$

Using the initial condition $u_\parallel = 1$, we can solve (2.47) using separation of variables,

$$u_\parallel(\phi) = \frac{1}{1 + r_0 \, I(\phi)} \,, \qquad I(\phi) \equiv a_0^2 \int_0^\phi f^2(\varphi) \, d\varphi \,. \tag{2.48}$$

Since $\dot{\phi} = u_\parallel(\phi)$ we may use the relationship

$$s(\phi) = \int_0^\phi \left[1 + r_0 \, I(\varphi)\right] \, d\varphi \tag{2.49}$$

to trade proper time s for the invariant phase ϕ. Following [33], we introduce a rescaled velocity v^μ by

$$u^\mu(s) = u_\parallel(\phi) v^\mu(\phi) \,, \quad \dot{u}^\mu = -r_0 a_0^2 f^2(\phi) u_\parallel^3 v^\mu(\phi) + u_\parallel^2(\phi) v'^\mu \,. \tag{2.50}$$

Plugging this in (2.46) we find that

$$v'^{\mu} = \left[\frac{a_0 f(\phi)}{u_{\parallel}(\phi)} + r_0 a_0 f'(\phi)\right] f^{\mu}{}_{\nu} v^{\nu} + \frac{r_0 a_0^2 f^2(\phi)}{u_{\parallel}(\phi)} n^{\mu} \ . \tag{2.51}$$

Since $f^{\mu}{}_{\nu} n^{\nu} = 0$ we can solve this for v using the exponential ansatz

$$v^{\mu}(\phi) = [\exp(I_1(\phi) f)]^{\mu}{}_{\nu} \, v_0^{\nu} + I_2(\phi) n^{\mu} \ , \tag{2.52}$$

where

$$I_1(\phi) = \int_0^{\phi} d\varphi \, \left[\frac{a_0 f(\varphi)}{u_{\parallel}(\varphi)} + r_0 a_0 f'(\varphi)\right], \quad I_2(\phi) \ = \ \int_0^{\phi} d\varphi \, \frac{r_0 a_0^2 f^2(\varphi)}{u_{\parallel}(\varphi)} \ , \tag{2.53}$$

subject to the initial condition $v(0) = v_0 = u_0$. The null field properties lead to

$$(f^2)^{\mu}{}_{\nu} = n^{\mu} n_{\nu} \ , \quad (f^n)^{\mu}{}_{\nu} = 0 \ , \ n \geq 3 \ , \tag{2.54}$$

which allows us to simplify (2.52) considerably

$$v^{\mu}(\phi) \ = \ v_0^{\mu} \ + \ I_1(\phi) \, f^{\mu}{}_{\nu} v_0^{\nu} \ + \ \left[I_2(\phi) + \frac{1}{2} I_1^2(\phi) \right] n^{\mu}. \tag{2.55}$$

The exact solution is therefore

$$u^{\mu}(s) \ = \ \frac{v^{\mu}(\phi)}{1 + r_0 I(\phi)}, \tag{2.56}$$

where proper time s is given in (2.49). To calculate the exact solution without radiative corrections, we simply set $r_0 = 0$ in (2.56) and (2.53) to give

$$u^{\mu}(s) \ = \ u_0^{\mu} \ + \ I_1(s) \, f^{\mu}{}_{\nu} u_0^{\nu} \ + \ \frac{1}{2} I_1^2(s) \, n^{\mu}, \qquad I_1(s) \ = \ a_0 \int_0^s d\varphi \ f(\varphi) \, . \tag{2.57}$$

Setting the initial conditions

$$u_0^{\mu} = (1, \mathbf{0}), \tag{2.58}$$

we find

$$u^0 = 1 + \frac{1}{2}I_1^2\,, \quad u^1 = -I_1\,, \quad u^2 = 0\,, \quad u^3 = \frac{1}{2}I_1^2\,. \tag{2.59}$$

We see that $u_\parallel = u^0 - u^3 = 1$ is conserved when we "switch off" RR. Neglecting the radiative effects greatly simplifies our equations. We may calculate (2.59) easily and use the results to evaluate the numerical method that will be introduced in the next section.

2.3 Covariant Matrix Method as an Approach to Particle Motion

To solve the equation of motion (2.20) numerically, a typical approach would be to use a finite difference scheme. Such schemes can introduce discretisation errors that violate the on-shell condition and lead to Lorentz violations. To avoid this, we introduce a novel numerical scheme for the calculation of the motion of classical charges in electromagnetic fields. Our method maintains explicit covariance and preserves the on-shell condition, $u^2 = 1$ (using natural units). Details of this method are presented in [34] and reproduced below.

To begin we introduce the matrix basis $\sigma_\mu \equiv (\mathbb{I}, \boldsymbol{\sigma})$ where $\boldsymbol{\sigma}$ denotes the three Pauli matrices

$$\sigma^1 = \begin{pmatrix} 0 & 1 \\ 1 & 0 \end{pmatrix}\,, \quad \sigma^2 = \begin{pmatrix} 0 & -i \\ i & 0 \end{pmatrix}\,, \quad \sigma^3 = \begin{pmatrix} 1 & 0 \\ 0 & -1 \end{pmatrix}\,, \tag{2.60}$$

which satisfy $\sigma^a\sigma^b = \delta_{ab} + i\varepsilon_{abc}\sigma^c$, where ε_{abc} is the Levi-Civita tensor in three-dimensions. We associate the four-velocity u^μ with the hermitian matrix

$$U \equiv u^\mu\sigma_\mu = \begin{pmatrix} u^+ & v_- \\ v_+ & u^- \end{pmatrix}\,, \quad u^\pm = u^0 \pm u^3\,, \quad v_\pm \equiv u^1 \pm iu^2 = v_\mp^*\,. \tag{2.61}$$

We have $\det(U) = u_0^2 - \mathbf{u}^2 = u^2 = 1$.

Let $F^a = \frac{1}{2}(E^a - iB^a)$ and $\mathbb{E} = F^a\sigma_a \quad \in su(2)$. We may write the equation of motion in

matrix form is as follows:

$$\dot{U} = \mathbb{E}^\dagger U + U\mathbb{E}\,. \tag{2.62}$$

In general $\mathbb{E}$ (or $F_{\mu\nu}$) will depend on s, $u^\mu(s)$ and $x^\mu(s)$. If $\mathbb{E} = \mathbb{E}(s)$ only then (2.62) is similar to a (linear) Schrödinger equation with time-dependent Hamiltonian. It can therefore be solved by introducing the time ordered product

$$L(s) \equiv \mathcal{T}\exp\left\{\int_0^s ds'\,\mathbb{E}^\dagger(s')\right\} \in SL(2,\mathbb{C})\,. \tag{2.63}$$

The solution of (2.62) becomes

$$U(s) = L(s)U(0)L^\dagger(s)\,. \tag{2.64}$$

If however $\mathbb{E} = \mathbb{E}(s;x(s),u(s))$ the equation of motion becomes non-linear, but an iterative scheme is still expected to work. The solution (2.64) is ideally suited for the required numerical computations. To do this we introduce a discrete set of $n+1$ equally spaced proper time values s_k, $k = 0\ldots n$, such that

$$s_0 = 0\,, \qquad s_k = k\,ds\,, \qquad s_n = s\,, \qquad \mathbb{E}_k := \mathbb{E}\left(x(s_k)\right)\,. \tag{2.65}$$

We then approximate (with an error of order ds^2)

$$L \approx \exp\{\mathbb{E}_n^\dagger\, ds\} \times \ldots \times \exp\{\mathbb{E}_1^\dagger\, ds\} =: L_n\,, \tag{2.66}$$

where "$\times$" denotes matrix multiplication. For the solution (2.64) this implies

$$U(s) \;=\; U_n(s) + \;\mathcal{O}(ds)\,, \quad \text{where} \quad U_n(s) = L_n U(0) L_n^\dagger\,, \tag{2.67}$$

i.e. our method corresponds to a first-order scheme.

For a numerical solution, we evaluate (2.67) iteratively. To calculate the approximate solution of the matrix $U_n(s)$ we need to know the matrix fields $\mathbb{E}_k$. These fields depend on

the particle's position. We assume that the approximate values $u(s_i)$ have been determined and then use the trapezium rule to calculate the position of the particle. The position is used to find values for $\mathbb{E}_k$, which in turn is used to find an improved set $u(s_i)$ of four-velocities. This is repeated for each given proper time s_i until $x(s_i)$ and $u(s_i)$ settle within given error margins. To start the iteration, we use $u(s_i) = u_0$, for all $i = 0, \ldots, n$.

We can show that the on-shell condition is exactly maintained by the approximate solution. Using (2.67) we have

$$U(s\ +\ ds) = e^{\mathbb{E}^\dagger ds} U(s) e^{\mathbb{E} ds} \quad \left(+O(ds^2)\right). \tag{2.68}$$

Noting that since $\mathbb{E}$ is a hermitian matrix, $\det(\exp(\mathbb{E}ds)) = 1$, we find therefore that

$$\begin{aligned} \det(U(s+ds)) &= \det(e^{\mathbb{E}^\dagger ds})\ \det(U(s))\ \det(e^{\mathbb{E} ds}) \\ &= 1 \times (u_0^2 - \mathbf{u}^2) \times 1 = 1. \end{aligned} \tag{2.69}$$

So for all n

$$\det U_n(s) = \det U(0) = 1\ . \tag{2.70}$$

Hence we are preserving the on-shell condition exactly.

2.3.1 Constant Fields

Using our new method to solve the equations of motion we refer back to (2.63) and (2.64). In the simple case of time-independent fields the method is exact since there is no path ordering needed and therefore no need to approximate $L(s)$ in (2.63). We will consider the four cases discussed by Taub [35]; constant E field only, constant B field only, crossed fields and parallel fields. We expect to observe hyperbolic, elliptic, parabolic and loxodromic (spiraling) motion respectively.

2.3.1.1 Constant Electric Field

Firstly consider the case of a charged particle in a constant electric field (e.g. in a particle accelerator). We will use the case where the electric field points in the x^1 direction only and there is no magnetic field present, i.e. $\mathbf{E} = E\mathbf{e}_1 = const$, $\mathbf{B} = 0$. We find that this

simplifies our expression for $L(s)$:

$$L(s) = L^{\dagger}(s) = \exp\left\{\frac{1}{2}\mathbf{E}\cdot\boldsymbol{\sigma}s\right\}. \tag{2.71}$$

The particle four-velocity can now be obtained as follows,

$$U(s) = \exp\left\{\frac{1}{2}\mathbf{E}\cdot\boldsymbol{\sigma}s\right\}U(0)\exp\left\{\frac{1}{2}\mathbf{E}\cdot\boldsymbol{\sigma}s\right\}. \tag{2.72}$$

Assuming that the particle is initially at rest simplifies things further and using hyperbolic identities we find the components of the four-velocity easily,

$$U(s) = \exp\{\mathbf{E}\cdot\boldsymbol{\sigma}s\} = \cosh(Es) + \sinh(Es)\frac{\mathbf{E}}{E}\cdot\boldsymbol{\sigma}. \tag{2.73}$$

The electric field is in the x^1 direction only and so the components of velocity are

$$u^0 = \cosh(Es), \;\; u^1 = \sinh(Es), \;\; u^2 = u^3 = 0. \tag{2.74}$$

By integration the particle's trajectory can also be found,

$$x^0 = \frac{1}{E}\sinh(Es), \;\; x^1 = \frac{1}{E}\cosh(Es), \;\; x^2 = x^3 = 0. \tag{2.75}$$

The left panel of Figure 2.1 shows the velocity in the direction of the electric field and the right panel shows the trajectory in the direction of the electric field as a function of s. There is no acceleration in the directions perpendicular to the electric field so the motion remains constant in those directions. We see hyperbolic motion as expected since the particle moves with constant proper acceleration.

2.3.1.2 Constant Magnetic Field

Now consider the case of a charged particle in a constant magnetic field (e.g. in a synchrotron) in the x^1 direction, and there is no electric field present, i.e. $\mathbf{B} = B\mathbf{e}_1 = const$,

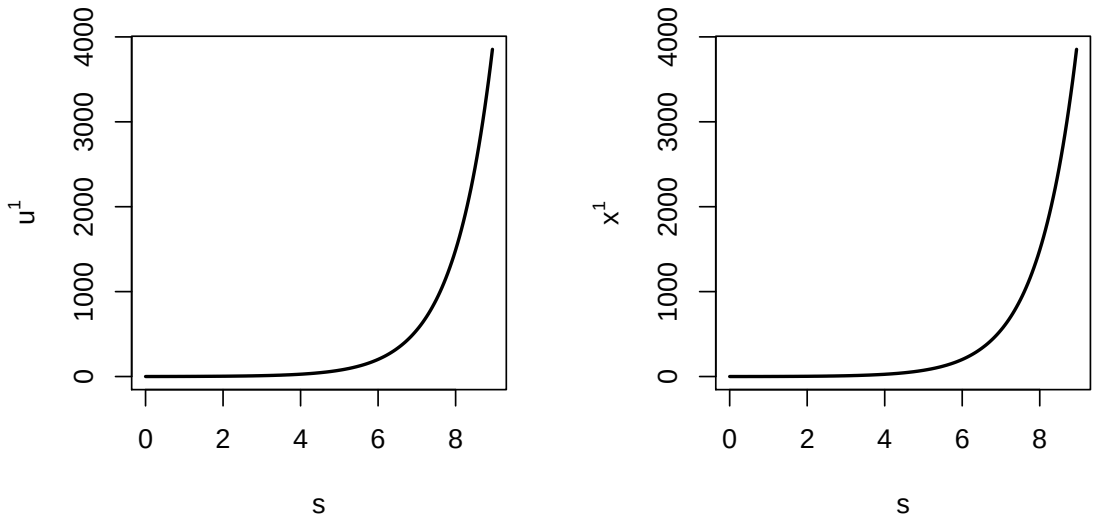

Figure 2.1: Left: Velocity, *Right:* Trajectory, for constant electric field ($E = 1$) in the x^1 direction.

$\mathbf{E} = 0$. (2.63) now becomes

$$L(s) = \exp\left\{\frac{1}{2}i\mathbf{B}\cdot\boldsymbol{\sigma}s\right\},\ \ L^{\dagger}(s) = \exp\left\{-\frac{1}{2}i\mathbf{B}\cdot\boldsymbol{\sigma}s\right\}. \tag{2.76}$$

This results in the following expression for $U(s)$:

$$U(s) = \exp\left\{\frac{1}{2}i\mathbf{B}\cdot\boldsymbol{\sigma}s\right\}U(0)\exp\left\{-\frac{1}{2}i\mathbf{B}\cdot\boldsymbol{\sigma}s\right\}. \tag{2.77}$$

It is useful to write this in terms of its trigonometric identities,

$$U(s) = \left(\mathrm{c} + i\mathrm{s}\frac{\mathbf{B}}{B}\cdot\boldsymbol{\sigma}\right)(u_0(0)\mathbb{I} + \mathbf{u}(0)\cdot\boldsymbol{\sigma})\left(\mathrm{c} - i\mathrm{s}\frac{\mathbf{B}}{B}\cdot\boldsymbol{\sigma}\right), \tag{2.78}$$

where $\mathrm{c} = \cos(Bs/2)$ and $\mathrm{s} = \sin(Bs/2)$. Assuming an initial velocity, $u^{\mu}(0) = (u_0, 0, 0, u_z)$ and a constant magnetic field $\mathbf{B} = B\mathbf{e}_1$, Eq. (2.78) is greatly simplified. $\mathbf{B}\cdot\boldsymbol{\sigma}/B$ is simply σ_1 and $\mathbf{u}(0)\cdot\boldsymbol{\sigma}$ is simply $u_z\sigma_3$. We may rewrite the above equation in matrix form:

$$U(s) = \begin{pmatrix} \mathrm{c} & i\mathrm{s} \\ i\mathrm{s} & \mathrm{c} \end{pmatrix}\begin{pmatrix} u_0 + u_z & 0 \\ 0 & u_0 - u_z \end{pmatrix}\begin{pmatrix} \mathrm{c} & -i\mathrm{s} \\ -i\mathrm{s} & \mathrm{c} \end{pmatrix}. \tag{2.79}$$

After multiplying out the matrices and simplifying, the expression for $U(s)$ can now be written as

$$U(s) = \begin{pmatrix} u_0 + u_z\cos(Bs) & -iu_z\sin(Bs) \\ iu_z\sin(Bs) & u_0 - u_z\cos(Bs) \end{pmatrix}. \tag{2.80}$$

Therefore the components of the velocity can be deduced:

$$u^0 = u_0,\ \ u^1 = 0,\ \ u^2 = u_z\sin(Bs),\ \ u^3 = u_z\cos(Bs). \tag{2.81}$$

Note that $u^0(s) = u_0$ is conserved as there is no energy transfer in the magnetic field. By integration the trajectory of the particle is found,

$$x^0 = u_0 s,\ \ x^1 = 0,\ \ x^2 = -\frac{u_z}{B}\cos(Bs),\ \ x^3 = \frac{u_z}{B}\sin(Bs). \tag{2.82}$$

The left panel of Figure 2.2 shows the velocity and the right panel shows the trajectory in the transverse directions. We observe elliptic motion as expected, with the particle in this

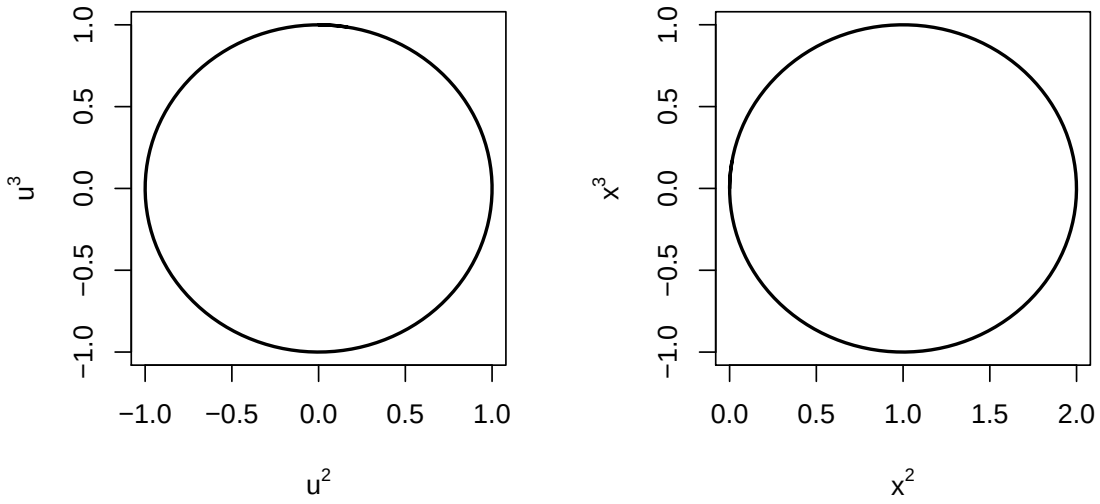

Figure 2.2: Left: Velocity, *Right:* Trajectory, for constant magnetic field ($B = 1$) in the x^1 direction.

case following a circular path.

In order to calculate the trajectory for a particle in crossed fields or in perpendicular electromagnetic fields a little more effort is required. We wish to find the components of velocity $u_0(s)$ and $\mathbf{u}(s)$ given

$$U(s) = u_0(s) + \mathbf{u}(s)\cdot\boldsymbol{\sigma} = L(s)U(0)L^{\dagger}(s) \tag{2.83}$$

and

$$L(s) = \exp\left\{\frac{1}{2}(\mathbf{E}+i\mathbf{B})\boldsymbol{\sigma}s\right\},\ \ L^{\dagger}(s) = \exp\left\{\frac{1}{2}(\mathbf{E}-i\mathbf{B})\boldsymbol{\sigma}s\right\}. \tag{2.84}$$

Our general expression for $U(s)$ given constant fields is

$$U(s) = \exp\left\{\frac{1}{2}(\mathbf{E}+i\mathbf{B})\boldsymbol{\sigma}s\right\}U(0)\exp\left\{\frac{1}{2}(\mathbf{E}-i\mathbf{B})\boldsymbol{\sigma}s\right\}. \tag{2.85}$$

Let $E_+ = \frac{1}{2}|\mathbf{E}+i\mathbf{B}\ s|$ and $E_- = \frac{1}{2}|\mathbf{E}-i\mathbf{B}\ s|$. Now $\exp((1/2)(\mathbf{E}+i\mathbf{B})\boldsymbol{\sigma}s) = C_\pm + S_\pm\hat{E}_\pm\boldsymbol{\sigma}$, where $C_\pm = \cosh(E_\pm)$, $S_\pm = \sinh(E_\pm)$ and $\hat{E}_\pm = \mathbf{E}\pm i\mathbf{B}/\left|\mathbf{E}\pm i\mathbf{B}\right|$. We therefore have

$$(C_+ + S_+\hat{E}_+\boldsymbol{\sigma})\ (u_0(0)+\mathbf{u}(0)\cdot\boldsymbol{\sigma})\ (C_- + S_-\hat{E}_-\boldsymbol{\sigma}). \tag{2.86}$$

Taking the first two brackets of this equation and expanding gives

$$C_+u_0 + C_+\mathbf{u}\cdot\boldsymbol{\sigma} + u_0S_+\hat{E}_+\boldsymbol{\sigma} + S_+\hat{E}_+(\boldsymbol{\sigma}\cdot\mathbf{u})\boldsymbol{\sigma} \tag{2.87}$$

Note that (2.87) can be written in the form $v_0 + \mathbf{v}\cdot\boldsymbol{\sigma}$. Using this idea repeatedly on expanding the brackets and using well known vector properties we end up with the messy looking expressions for $u_0(s)$ and $\mathbf{u}(s)$:

$$\begin{aligned}
u_0 &= u_0(0)C_+C_- + \hat{E}_+\mathbf{u}(0)C_-S_+ + \mathbf{u}(0)\hat{E}_-C_+S_- + \hat{E}_+\hat{E}_-u_0(0)S_+S_-\ ,\\
\mathbf{u} &= u_0(0)C_+S_-\hat{E}_- + S_+\hat{E}_+\mathbf{u}(0)S_-\hat{E}_- + C_+C_-\mathbf{u}(0) + i\mathbf{u}(0)\times\hat{E}_-C_+S_-\\
&\quad + u_0(0)S_+C_-\hat{E}_+ + i\hat{E}_+\times\hat{E}_-u_0(0)S_+S_- + iS_+C_-\hat{E}_+\times\mathbf{u}(0)\\
&\quad - (\hat{E}_+\times\mathbf{u}(0))\times\hat{E}_-S_+S_-\ .
\end{aligned} \tag{2.88}$$

This is the most general case for constant E and B fields however this expression dramatically simplifies for the four special cases considered.

Take for example the case of a constant electric field only in the x^1 direction. Assuming $U(0) = \mathbb{I}$ as before and using the fact that $\mathbf{E}\cdot\mathbf{B} = 0$ and $\mathbf{B} = 0$, the expressions for u_0 and $\mathbf{u}$ agree with those obtained in (2.74). Similarly, substituting $\mathbf{B} = B\mathbf{e}_1$, $\mathbf{E} = 0$, and $U(0) = u_0\,\mathbb{I} + u_z\,\sigma_3$, we get back the results from (2.81).

2.3.1.3 Crossed Fields

We may use (2.88) to find the trajectory for a particle in crossed fields. Let us consider the case where $\mathbf{E} = E\mathbf{e}_1$ and $\mathbf{B} = B\mathbf{e}_2$, it follows that $\mathbf{E}\cdot\mathbf{B} = 0$. To simplify matters we assume that the particle is initially at rest. Eq. (2.88) reduces to

$$\begin{aligned} u_0 &= \cosh^2(a\,s) + \sinh^2(a\,s)\frac{\mathbf{E}^2+\mathbf{B}^2}{\mathbf{n}^2} \\ \mathbf{u} &= 2\sinh(a\,s)\cosh(a\,s)\frac{\mathbf{E}}{(\mathbf{n}^2)^{1/2}} + 2\sinh^2(a\,s)\frac{\mathbf{E}\times\mathbf{B}}{\mathbf{n}^2}, \end{aligned} \tag{2.89}$$

in agreement with [36] where $\mathbf{n} = \mathbf{E} + i\mathbf{B}$ and $a = (1/2)(\mathbf{n}^2)^{1/2}$. For crossed fields where $E = B$ we see that $\mathbf{n}^2 = 0$. Taking the limiting case of Eq. (2.89) where $\mathbf{n}^2 = 0$, we get the resulting expressions for the four-velocity in crossed fields:

$$u^0 = 1 + \frac{1}{2}E^2\,s^2,\;\; u^1 = E\,s,\;\; u^2 = 0,\;\; u^3 = \frac{1}{2}E^2\,s^2, \tag{2.90}$$

and corresponding trajectory:

$$x^0 = s + \frac{E^2}{6}\,s^3,\;\; x^1 = \frac{E}{2}\,s^2,\;\; x^2 = 0,\;\; x^3 = \frac{E^2}{6}\,s^3. \tag{2.91}$$

We note that $u^0 - u^3$ is conserved, a feature that will come in useful in Chapter 4 when we calculate the spectrum of radiation for crossed fields. The left panel of Figure 2.3 shows the velocity and the right panel shows the trajectory in the $x-z$ plane. We observe parabolic motion in the velocity as expected with the particle forming a parabola shaped path.

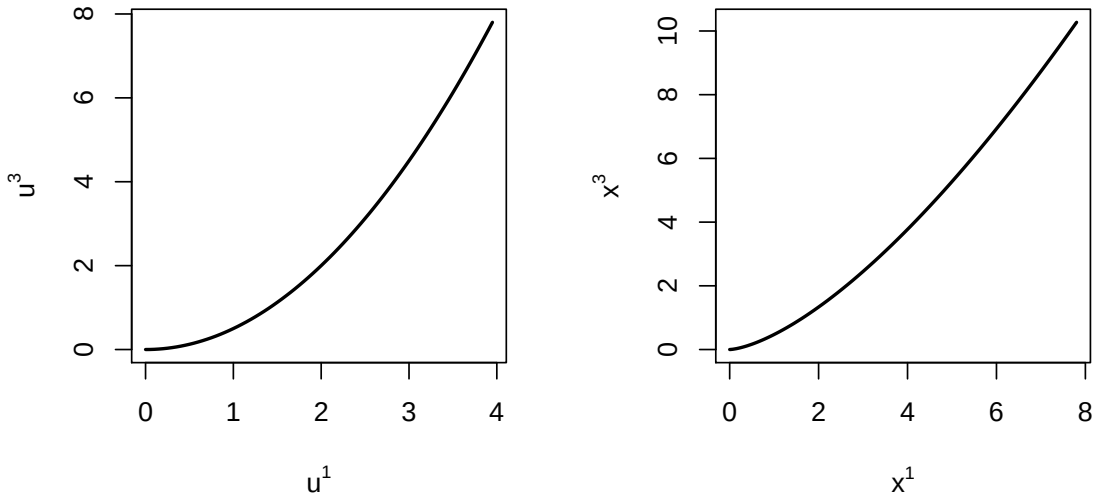

Figure 2.3: Left: Velocity, *Right:* Trajectory, for crossed fields ($E = 1$ and $B = 1$) where the electric field is in the x^1 direction and the magnetic field is in the x^2 direction.

2.3.1.4 Parallel Fields

Finally for the case of parallel fields we shall use $\mathbf{E} = \mathbf{B} = E\mathbf{e}_1$ and initial velocity $u^\mu(0) = (u_0, 0, 0, u_z)$. We can therefore reduce (2.88) using the fact that $\mathbf{E}\cdot\mathbf{B} = E^2$ and $\mathbf{E}^2 - \mathbf{B}^2 = 0$. Making use of several trigonometric and hyperbolic identities we end up with the four-velocity

$$u^0 = u_0\cosh(Es), \;\; u^1 = u_0\sinh(Es), \;\; u^2 = u_z\sin(Es), \;\; u^3 = u_z\cos(Es). \qquad (2.92)$$

and upon integration

$$x^0 = \frac{u_0}{E}\sinh(Es), \;\; x^1 = \frac{u_0}{E}\cosh(Es), \;\; x^2 = -\frac{u_z}{E}\cos(Es), \;\; x^3 = \frac{u_z}{E}\sin(Es). \qquad (2.93)$$

Notice that the parallel fields case is the sum of the constant electric field case and the constant magnetic field case. This can be seen visually in Figure 2.4 as a superposition of the corresponding plots (see Figures 2.1 and 2.2). We observe loxodromic motion as expected, the motion following a spiraling path.

Our new approach to particle motion allows us to calculate the trajectories and velocities

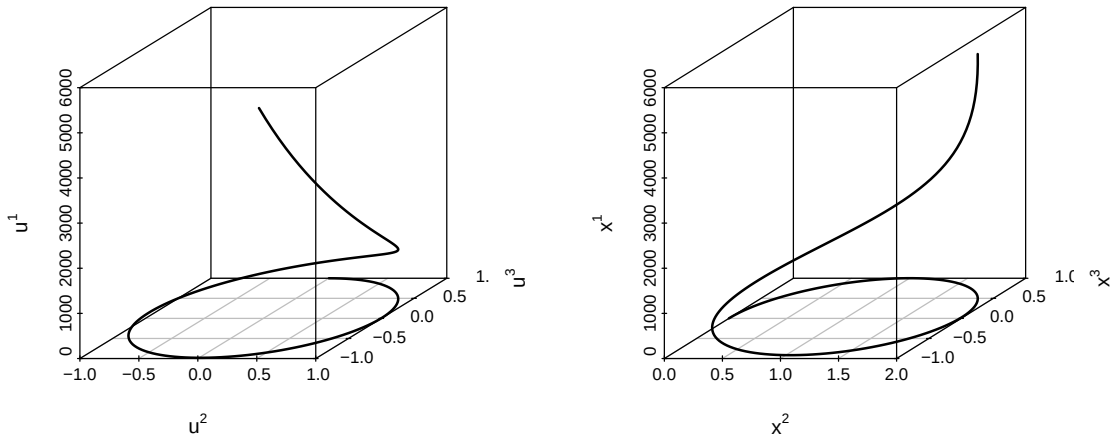

Figure 2.4: Left: Velocity, *Right:* Trajectory, for parallel fields ($E = 1$ and $B = 1$) in the x^1 direction.

for a charge in constant fields exactly. As expected we observe hyperbolic motion for a constant electric field, elliptic motion for a constant magnetic field, parabolic motion (for u^μ) for crossed fields and loxodromic/spiraling motion for parallel electromagnetic fields. Next we shall see how our new approach performs when the fields are no longer constant.

2.3.2 Time Dependent Fields

The numerical method will now be tested for a time dependent field. Using our pulsed plane wave defined in Section 2.2 and initially neglecting radiative reaction effects, we produce Figure 2.5, which shows our laser pulse function f from (2.45) as a function of invariant phase (left) and the velocity components u^0 and u^1 from (2.59) as a function of invariant phase, $\phi = s$ (right).

The numerical solution, using a step size $ds = 0.125$, is not visibly distinguishable from the analytic solution in the plots. To quantify the numerical error, we compare the numerical solution $u^\mu(s)$ to the exact solution $u^\mu_{ex}(s)$ using the Euclidean norm and a maximum norm. Looking firstly at the Euclidean norm, we have

$$\varepsilon_{eucl} = \sqrt{\left(\frac{1}{\Delta s}\int_{s_0-\Delta s}^{s_0+\Delta s} ds\, P^2(s) \sum_{\mu=0}^{4} \left[u^\mu(s) - u^\mu_{ex}(s)\right]^2\right)}, \tag{2.94}$$

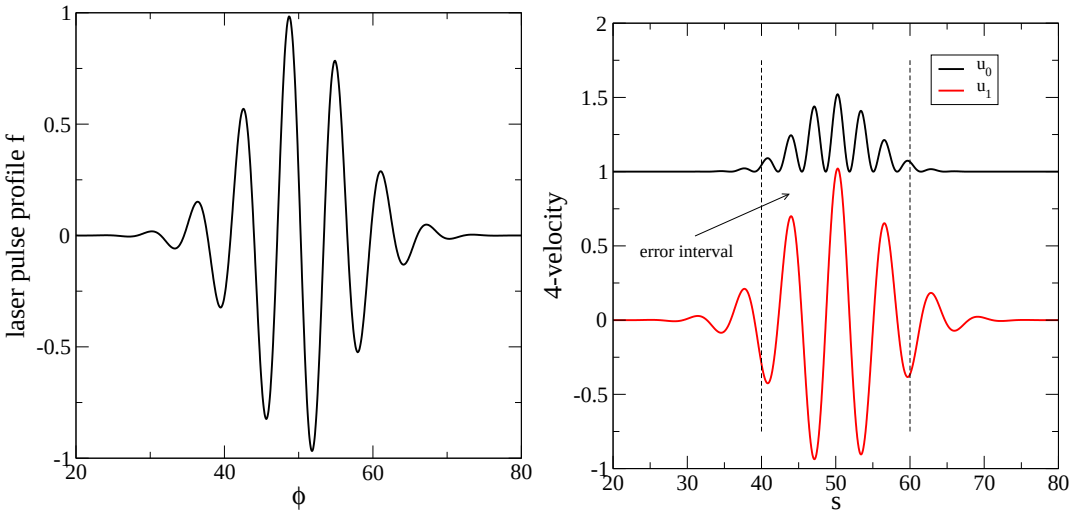

Figure 2.5: Left: Laser pulse function f as a function of invariant phase, ϕ. *Right:* Velocity components u_0 and u_1 as a function of invariant phase, $\phi = s$. These plots have been produced using the parameter values $\phi_0 = 50$, $N = 10$ and $a_0 = 1$.

where $P(s) = \exp\left\{-(s-s_0)^2/N^2\right\}$. Since $ds \longrightarrow \frac{\Delta s}{N_D}$, where N_D is the number of data points, the above may be equivalently written as

$$\varepsilon_{eucl} = \sqrt{\left(\frac{1}{N_D}\sum_{s_0-\Delta s}^{s_0+\Delta s} P^2(s) \sum_{\mu=0}^{4} \left[u^\mu(s) - u^\mu_{ex}(s)\right]^2\right)}\,. \tag{2.95}$$

Here, the Centre of mass s_0 and width Δs of the pulse are defined via

$$\begin{aligned} s_0 &= \frac{1}{C}\int_{-\infty}^{\infty} ds\, s\, P^2(s), \\ C &= \int_{-\infty}^{\infty} ds\, P^2(s), \\ \Delta s &= 2\sqrt{s_2 - s_0^2}, \\ s_2 &= \frac{1}{C}\int_{-\infty}^{\infty} ds\, s^2\, P^2(s). \end{aligned} \tag{2.96}$$

The error interval can be seen in Figure 2.5.

To calculate the maximum norm the following equation is used,

$$\varepsilon_{max} = \max\left[|u^\mu(s) - u^\mu_{ex}(s)|\right] \qquad \forall\ s, \mu\ , \tag{2.97}$$

which simply uses the maximum difference between exact and numerical results out of all the possible values of μ and s. Both error estimates are shown in Figure 2.6 as a function

of discretisation step size ds. They are well fitted by $\varepsilon_{eucl} \approx 0.32(1)\, ds$, $\varepsilon_{max} \approx 0.50(1)\, ds$ and are linearly proportional to ds (as expected since we are using a first-order scheme).

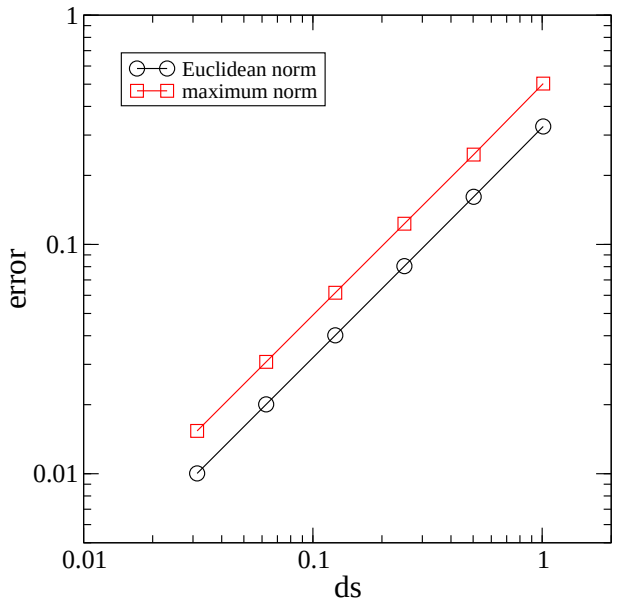

Figure 2.6: Numerical errors (2.94) and (2.97) as a function of the proper time discretisation step ds for a linearly polarised laser pulse using our first-order method.

2.3.3 Higher Order Numerics

We have seen that the covariant matrix approach is a powerful method that allows us to solve the LL equation for arbitrary fields whilst still preserving the on-shell condition. Now that we have a working first order scheme, the next logical step is to extend this method to higher orders of accuracy. Currently we have

$$U(s) \;=\; U_n(s) + \mathcal{O}(ds). \tag{2.98}$$

This is fine if ds is very small, however it is desirable to have a scheme that produces accurate results using even a coarse mesh. The current program approximates

$$L(s) \equiv \mathcal{T}\exp\left\{\int_0^s ds' \,\mathbb{E}^\dagger(s')\right\} \approx \exp\{\mathbb{E}_n^\dagger ds\} \times \ldots \times \exp\{\mathbb{E}_1^\dagger ds\} =: L_n\,, \quad L(0) = 1\,, \tag{2.99}$$

which has an error of order ds^2. We will find a more accurate approximation of $L(s)$ with an error of ds^5. To do this we take the derivative of L, $L^\dagger$ and x with respect to s and solve

the coupled ODEs using the fourth-order Runge-Kutta method (RK4). The derivative equations for L and $L^\dagger$ are implied by (2.62) and (2.64) as follows

$$\frac{dL(s)}{ds} = \mathbb{E}^\dagger \times L(s) \ , \quad \frac{dL^\dagger(s)}{ds} = L^\dagger(s) \times \mathbb{E} \ . \tag{2.100}$$

We form the vector $\mathscr{L}(s) = (L(s), X(s))$, where $X = x^\mu \sigma_\mu$, so that

$$\frac{d\mathscr{L}}{ds} = \begin{pmatrix} \dfrac{dL}{ds} \\ \dfrac{dX}{ds} \end{pmatrix} = \begin{pmatrix} \mathbb{E}^\dagger(X(s))\, L(s) \\ \\ L(s)\, U(0)\, L^\dagger(s) \end{pmatrix}, \tag{2.101}$$

since $dX(s)/ds = U(s)$. If we let $d\mathscr{L}/ds = f(s, \mathscr{L})$ subject to the initial conditions $L(0) = 1$, $X(0) = 0$ then we can apply RK4 as follows:

$$\mathscr{L}_{n+1} = \mathscr{L}_n + \frac{1}{6}\,(k_1 + 2k_2 + 2k_3 + k_4), \tag{2.102}$$

where $\mathscr{L}_n = \mathscr{L}(s_n)$ and $\mathscr{L}_{n+1} = \mathscr{L}(s_n + ds)$ and where

$$\begin{aligned} k_1 &= ds\ f(s_n, \mathscr{L}_n) \\ k_2 &= ds\ f(s_n + \frac{1}{2}ds, \mathscr{L}_n + \frac{1}{2}k_1) \\ k_3 &= ds\ f(s_n + \frac{1}{2}ds, \mathscr{L}_n + \frac{1}{2}k_2) \\ k_4 &= ds\ f(s_n + ds, \mathscr{L}_n + k_3)\ . \end{aligned} \tag{2.103}$$

We then read off our values of L and X from the vector $\mathscr{L}(s)$ and use them to calculate $U(s)$ according to $U(s) = L(s)U(0)L^\dagger(s)$ at each time step.

To check that our method is now fourth-order we use it to find the four-velocity for our pulsed plane wave and calculate the errors according to our definitions in Eq. (2.94) and (2.97) (Euclidean norm and maximum norm respectively). Results are shown in Figure 2.7. We find that the errors are proportional to ds^4 as expected for a fourth-order method. Comparing the slopes in Figures 2.6 and 2.7 we calculate for the first-order method that our gradient $= 1.0$ and for the fourth-order method the gradient $= 4.0$ as ex-

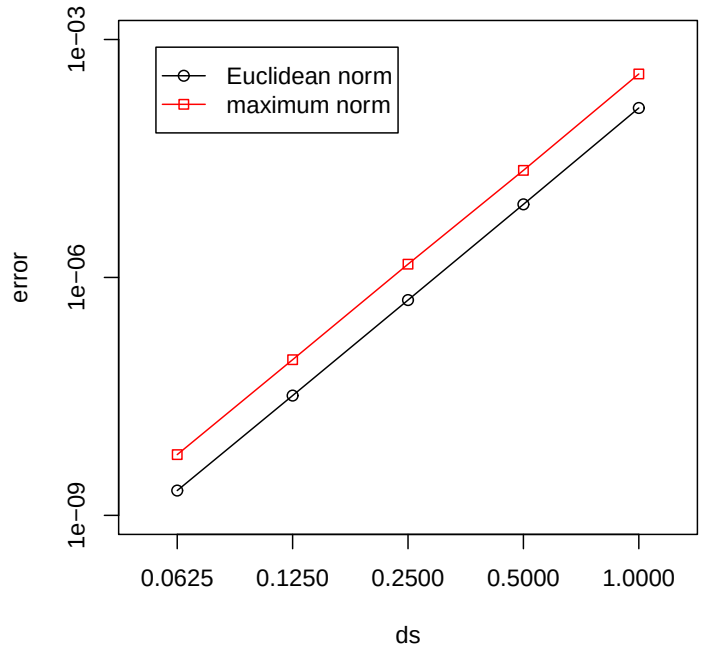

Figure 2.7: Numerical errors (2.94) and (2.97) as a function of the proper time discretisation step ds for a linearly polarised laser pulse using RK4. The errors are proportional to ds^4 as expected for this fourth-order method.

pected. By using this method we achieve a very high accuracy with a step size as large as $ds = 1$ (better than $ds = 0.03125$ using the first-order alternative). In Figure 2.7 we have an error of less than 10^{-3} for $ds = 1$ compared to an error of approximately 0.5 in Figure 2.6.

2.4 Impact of Radiation Reaction

Having found our method to be consistent with analytic results, we may now include the radiation reaction term. First we write the LL equation (2.46) in terms of an effective field strength tensor $G^{\mu}{}_{\nu}$,

$$\dot{u}^{\mu} = G^{\mu}{}_{\nu} u^{\nu} , \tag{2.104}$$

$$G^{\mu}{}_{\nu} = a_0 f f^{\mu}{}_{\nu} + r_0 a_0 u_{\parallel} \left\{ f' f^{\mu}{}_{\nu} + a_0 f^2 (n^{\mu} u_{\nu} - n_{\nu} u^{\mu}) \right\} . \tag{2.105}$$

Next we define an $su(2)$ matrix,

$$\mathbb{G} \equiv G^a \sigma_a \equiv \frac{1}{2}\left(G^{0a} + \frac{i}{2}\varepsilon^{abc} G^{bc}\right)\sigma_a \,, \tag{2.106}$$

so that the LL equation can be rewritten as

$$\dot{U} = \mathbb{G}^\dagger U + U\mathbb{G} \,, \tag{2.107}$$

in complete analogy with the $SL(2,\mathbb{C})$ Lorentz equation (2.62). We can replace $\mathbb{E}$ with $\mathbb{G}$ in the program used before.

The plots in Figure 2.8 show the numerical results for u^0 with and without radiative damping. Surprisingly u^0 is larger when radiation is accounted for; the electron gains energy from the radiation field produced by its acceleration. From these plots it is clear that radiative damping can have a significant effect.

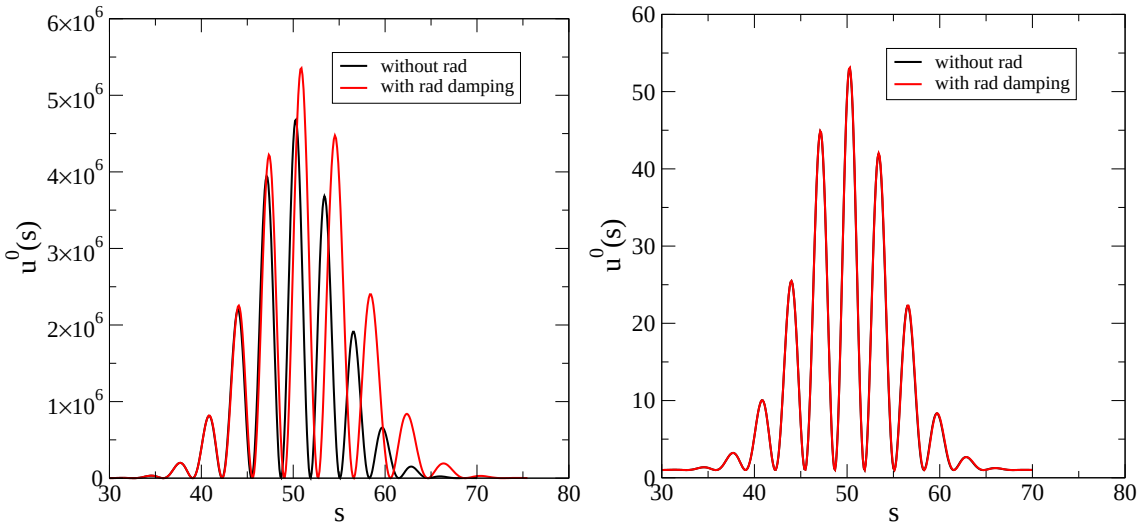

Figure 2.8: The γ factor u^0 of the particle as a function of the dimensionless proper time s without and with radiative damping. *Left:* $a_0 = 3\times 10^3$ and $v_0 = 10^{-6}$ (optical laser). *Right:* $a_0 = 10$ and $v_0 = 10^{-3}$ (XFEL).

As a_0 increases so does the effect of radiative back reaction. To quantify the deviation,

we use the maximum norm,

$$\delta = \frac{1}{N} \max_{s,\mu} \left| u^{\mu}\left[\alpha = 0\right](s) - u^{\mu}\left[\alpha = \frac{1}{137}\right](s) \right| ,$$
$$N = u^{\mu}\left[\alpha = 0\right](s_{\max}), \quad \text{for} \quad \left| u^{\mu}\left[\alpha = 0\right](s_{\max}) - u^{\mu}\left[\alpha = \frac{1}{137}\right](s_{\max}) \right| \to \max , \tag{2.108}$$

where $u^{\mu}\left[\alpha = 0\right](s)$ is the four-velocity of the particle without radiative damping and $u^{\mu}\left[\alpha = 1/137\right](s)$ is the four-velocity with damping. $s_{\max}$ represents the value of s where the maximum difference occurs. Hence the deviation δ can be interpreted as the maximum relative deviation between the full four-velocity and the four-velocity without the radiative back reaction. Figure 2.9 shows the deviation for varying a_0. From the plot it can be seen that for large values of a_0, the RR has a significant impact on the four-velocity. The results showed that RR is significant in the case of an optical laser, although it is negligible for an XFEL.

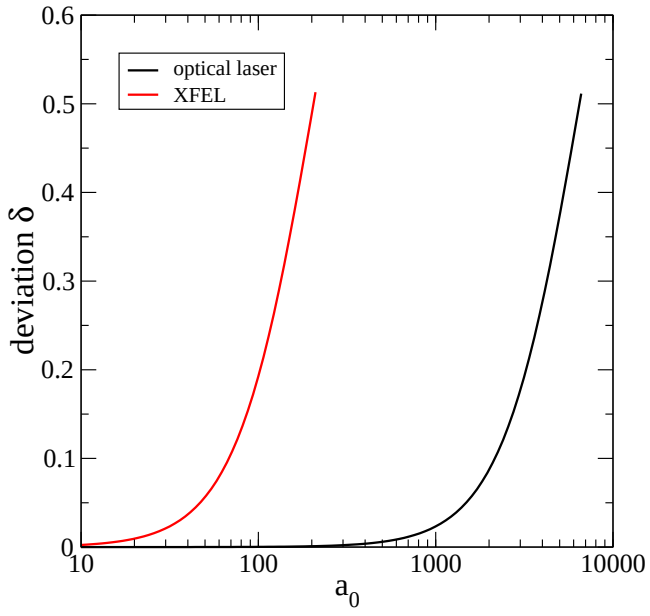

Figure 2.9: The deviation δ from (2.108) measuring the difference between the 4-velocities with and without radiative damping as a function of a_0 for the linearly polarised laser pulse. For an optical laser: $\nu_0 = 10^{-6}$; for an XFEL: $\nu_0 = 10^{-3}$.

We have seen that energy is radiated by an accelerated charge and how this impacts on the equations of motion. The LL equation provides a well behaved description of the motion of a charge taking into account RR. Using the numerical method outlined in Section 2.3,

we were able to include the RR of the particle and solve the LL equation for a pulsed plane wave. Due to its null-plane properties the results could be verified analytically and were consistent with the known analytic solution [33, 37]. Errors scaled as expected with the discretisation step size. Comparing and contrasting results with and without RR we have seen that the particle gains energy from the radiated fields. We note that our calculations are based on an initial γ factor of 1, i.e. starting with the particle at rest. However, radiation in one frame of reference may not necessarily look like radiation in another. It has been shown for example in [31] that for a head-on collision of the charged particle with the laser we get a net energy loss. We will continue to consider the impact of RR on our results in the next chapter, where we will be trying to achieve a net acceleration using laser fields.

Chapter 3

Vacuum Acceleration

Having studied the equations of motion and established methods of solution for these equations we can now look at applying our methods to the study of vacuum laser acceleration. We consider how we might accelerate a particle from rest with a laser pulse, without the use of plasmas. It has been greatly debated whether it is possible for electrons to obtain net energy gain from a plane wave laser pulse in vacuum, based on the Lawson-Woodward Theorem. The Lawson-Woodward Theorem states that the net energy gain of an electron interacting with an electromagnetic field in vacuum is zero under the following conditions: (i) the region of interaction is infinite, (ii) the laser field is in vacuum with no walls or boundaries present, (iii) the electron is highly relativistic along the acceleration path, (iv) no static electric or magnetic fields are present, (v) nonlinear effects like ponderomotive forces and RR forces are neglected [38]. It is discussed by Troha et al. that electrons can be accelerated by plane electromagnetic waves, whilst still being consistent with the theorem [39–41].

In this chapter we shall briefly review some of the suggested methods of vacuum laser acceleration and then study in detail a select few of these possibilities. The selected areas covered will be short pulse acceleration, using a sequence of pulses, pulse shaping and lastly using a “two-colour” laser to accelerate a charge. All cases considered in this chapter will assume the particle is initially at rest.

3.1 Existing Schemes for Vacuum Laser Acceleration

There are many suggestions in the literature as to how an electron may gain energy from a laser pulse in vacuum and there have also been experimental observations showing that vacuum acceleration is indeed possible in a real laser field [42]. The energy of an electron can be extremely high at the peak of a laser pulse, but generally averages out to zero, leaving zero net energy gain. To take advantage of the high peak energies, an electron can be separated from the laser pulse before it decelerates; it can therefore continue to move forward without much energy loss [43, 44]. A thin foil for example can be used to stop the laser pulse, allowing the electron to escape from the pulse with a nonzero net energy gain [8]. There have however been many studies that suggest a potential for high net energy gain, even up to the order of TeV using intensities of $10^{22}\mathrm{W/cm}^2$ [45], without extracting electrons from the laser fields.

In order to get net acceleration after the full pulse duration we need a pulse with a nonzero average field, a unipolar pulse [46]. This comes down to our choice of pulse shape and there have been a number of examples of potential pulse shapes that enable acceleration. Subcycle laser pulses with averagely positive or fully positive fields can be used to accelerate electrons [47]. There have in particular been many studies into using half-wavelength acceleration [48, 49], which provides a fully positive field so the electron is never decelerated. There are experimental limitations to producing such fields, but as noted in [50], the half-wavelength solution provides an upper limit to the potential energy that an electron can gain from a laser field. Wang et al [50] consider using 'shock-like' laser pulses as an alternative to the half-wavelength method. They found that by using an intense laser with sharply rising or falling edges in vacuum, an electron can reach energies close to those found using the half-wavelength approach.

Short pulses, including the types mentioned above, are known to accelerate electrons. Some research has gone into comparing standard shape profiles of short pulses to see which may maximise accelaration [51, 52], but these short pulses are not the only ones that can accelerate electrons. One interesting way of producing effective pulse shapes is the use of 'two-colour' lasers [53], two co-propagating waves of different frequen-

cies. The crossing [54, 55] or overlapping [56] of two laser beams can produce an overall pulse with nonzero average field, capable of giving electrons considerable net energy gain. Whichever method one chooses to employ, the idea of 'staging' a series of pulses results in even higher gains as net energies are added for each pulse. The staging of two laser accelerators has been demonstrated in [57, 58].

We shall consider four methods of accelerating a particle from rest in vacuum. First we will look at the effects of using a short pulse to achieve a net acceleration. Using a sequence of n pulses results in an increase in energy gain for increasing n as the net energy received from each pulse builds up. This idea is briefly considered in Section 3.3. We then look at ways of choosing an optimum shape for a laser pulse to achieve maximum acceleration. We conduct a search for the optimum shape where N can be reasonably large (i.e. not a short pulse). Although standard shape profiles have been compared (e.g. [51, 53]), such a search does not seem to feature amongst the existing research into vacuum laser acceleration. The final method that we will explore is to overlap two lasers of differing frequency. This type of method features frequently in the literature, however our choice of frequency difference provides particularly promising results.

3.2 Short Pulse Acceleration

Changing the laser pulse duration can affect the final velocity of the particle. For our test case in Chapter 2 we found that the particle returned to its original velocity after the duration of the pulse. However, for a sufficiently short pulse we shall show how energy gains may be achieved. The term 'short pulse' in this section refers to few cycle pulses ($N \lesssim 10$). When our parameter N takes on values below 1, the pulse shape does not contain a complete cycle; we obtain a subcycle pulse.

3.2.1 Method

We require a pulse that can transfer a net acceleration to a particle. As stated in [46], to achieve this we require a unipolar pulse, which contains a Fourier zero mode. Consider

for example a simple model for a pulse with a Gaussian envelope

$$f(\phi) = \sin(\phi)\mathrm{e}^{-\phi^2/N^2}. \tag{3.1}$$

The Fourier transform of the function is

$$\widetilde{f}(s) = \int d\phi\ \mathrm{e}^{is\phi}\sin(\phi)\ \mathrm{e}^{-\phi^2/N^2}\ . \tag{3.2}$$

Replacing $\sin(\phi)$ with its exponential identity and rearranging, we may rewrite this expression as

$$\widetilde{f}(s) = \frac{1}{2i}\int d\phi\ \mathrm{e}^{i(s+1)\phi-\phi^2/N^2} - \frac{1}{2i}\int d\phi\ \mathrm{e}^{i(s-1)\phi-\phi^2/N^2}\ . \tag{3.3}$$

We assign the exponents to the functions $g_\pm(\phi)$ such that

$$g_\pm(\phi) = -\frac{\phi^2}{N^2} + i(s\pm 1)\phi\ , \quad g'_\pm(\phi) = -\frac{2\phi}{N^2} + i(s\pm 1)\ . \tag{3.4}$$

The zeros of the gradient function are thus given by $\phi_\pm = N^2\ i(s\pm 1)/2$. We take a Taylor expansion about these points for $g_\pm(\phi)$ and obtain, after simplifying the expansion,

$$g_\pm(\phi) = -\frac{N^2}{4}(s\pm 1)^2 - \frac{1}{N^2}(\phi-\phi_\pm)^2\ . \tag{3.5}$$

Now, we use this result to rewrite our Fourier transform of $f(\phi)$,

$$\begin{aligned}\widetilde{f}(s) &= \frac{1}{2i}\int d\phi\ \mathrm{e}^{g_+(\phi)} - \frac{1}{2i}\int d\phi\ \mathrm{e}^{g_-(\phi)} \\ &= \frac{1}{2i}\exp\left(-\frac{N^2}{4}(s+1)^2\right)\int d\phi' \mathrm{e}^{-\frac{1}{N^2}\phi'^2} - \frac{1}{2i}\exp\left(-\frac{N^2}{4}(s-1)^2\right)\int d\phi' \mathrm{e}^{-\frac{1}{N^2}\phi'^2}\ .\end{aligned} \tag{3.6}$$

Since both of the terms on the RHS of the equation above contain an integral of a Gaussian distibution, we can reduce this equation significantly giving the final result

$$\widetilde{f}(s) = i\sqrt{\pi}\, N\, \mathrm{e}^{\frac{N^2}{4}(s^2+1)}\ \sinh(s\,\frac{N^2}{2})\ . \tag{3.7}$$

We see quickly that $\widetilde{f}(0) = 0$, i.e. the Fourier zero mode for $f(\phi)$ is zero. This type of pulse has a zero average field and hence regardless of our pulse width we cannot achieve a net acceleration.

We try adding a carrier phase [46] as with our plane wave test case in Chapter 2, now

$$f(\phi) = \sin(\phi)\ \exp\left\{-\frac{(\phi-\phi_0)^2}{N^2}\right\}\ . \tag{3.8}$$

The Fourier transform of this function is

$$\widetilde{f}(s) = \int d\phi\ \mathrm{e}^{is\phi}\sin(\phi)\ \mathrm{e}^{-(\phi-\phi_0)^2/N^2}\ . \tag{3.9}$$

Similarly we can find an expression for the Fourier zero mode, which in this case is nonzero,

$$\widetilde{f}(0) = \sqrt{\pi}\, N\ \sin(\phi_0)\ \mathrm{e}^{-N^2/4}\ . \tag{3.10}$$

Note that if ϕ_0 is zero we get back the $\widetilde{f}(0) = 0$ that we expect when there is no carrier phase. Taking the average of the field we see that it is also nonzero since it is proportional to the zero mode,

$$\bar{f} \equiv \frac{1}{2\pi N}\int_{\phi_0-N\pi}^{\phi_0+N\pi} d\phi\ f(\phi) \simeq \frac{1}{2\pi N}\,\widetilde{f}(0) = \frac{1}{2\sqrt{\pi}}\sin(\phi_0)\ e^{-N^2/4}. \tag{3.11}$$

This is exponentially small for large N. Interestingly the magnitude of the average field depends on the two parameters ϕ_0 and N. For an appropriate choice of ϕ_0 and with a small value of N (how small to be determined shortly), significant gains can be made.

In order to study the effect of altering the pulse size it is important to ensure that the total energy of the pulse remains constant for each of the sizes considered. Since exper-

imentally we begin with a finite amount of energy, which is formed into different pulse shapes [53], the energy should be fixed in order to compare the pulses of varying width. For the plane wave test case studied in Chapter 2, our electromagnetic fields may be written as

$$\mathbf{E} = \mathbf{B} = -\mathbf{E}_0 \, P(\phi) \sin(\phi) \tag{3.12}$$

where $P(\phi) = \exp\left\{-(\phi - \phi_0)^2/N^2\right\}$ and $\phi = k \cdot x = \omega t - \mathbf{k} \cdot \mathbf{x}$. We considered the case where the amplitude $E_0 = |\mathbf{E}_0|$ was fixed. Simply changing N (which controls the width of the pulse) alters the total energy; as N is reduced so is the energy. $\mathbf{E}_0$ must therefore be defined by a function of N such that the total energy is kept constant, i.e. independent of N.

The energy density, w, is given by the equation

$$w = \frac{1}{2}(\mathbf{E}^2 + \mathbf{B}^2) = \mathbf{E}^2 = E_0^2 \, P^2(\phi) \, \sin^2(\phi). \tag{3.13}$$

The total energy, W, is therefore given by

$$W = \int d^3x \, w = A \int dz \, E_0^2 \, P^2(kz - \omega t) \, \sin^2(kz - \omega t), \tag{3.14}$$

where we let $\int (dxdy) = A$. We require the transverse energy density to be a finite constant,

$$\frac{W}{A} = const \equiv \sigma_0 = E_0^2(N) g(N), \tag{3.15}$$

where $g(N) = \int dz \, P^2(kz - \omega t) \, \sin^2(kz - \omega t)$. Hence the expression $E_0(N) = \sqrt{\sigma_0 / g(N)}$ must be used to ensure constant energy. In fact $g(N)$ may be worked out analytically to give

$$g(N) = \frac{1}{2k}\sqrt{\frac{\pi}{2}} N \left(1 - \cos(2\phi_0) \, e^{-N^2/2}\right) \; ; \quad k = \omega/c. \tag{3.16}$$

We can now change the amplitude E_0 with N such that $\sigma_0 = const$. Note that for large N, E_0 is proportional to $N^{-1/2}$.

Table 3.1: Values of the maximum γ^f (the peak value occurs at $N = 0.48$ unless otherwise stated). Results are shown for varying a_0 without RR and (for two choices of the dimensionless energy variable ν_0) with RR.

	no RR	$\nu_0 = 10^{-3}$	$\nu_0 = 10^{-6}$
$a_0 = 1$	2.9980	2.9980	2.9980
$a_0 = 10$	2.0080×10^2	2.0065×10^2	2.0080×10^2
$a_0 = 100$	1.9981×10^4	1.9105×10^4 (at N = 0.43)	1.9980×10^4
$a_0 = 1000$	1.9980×10^6	-	1.9829×10^6

3.2.2 Results

To investigate the effects of changing N, we vary E_0 as a function of N. We choose σ_0 such that the total energy is consistent with the choice in (2.45). Firstly considering the case where RR is ignored and using a value of $a_0 = 1$, we obtain the results illustrated in Figure 3.1, using the numerical method introduced in Chapter 2. The left-hand plot shows the final γ factor after the laser field has vanished as a function of the parameter N (which roughly counts the number of cycles within the pulse). We use the superscript 'f' to denote final values. This plot tells us a lot about the impact of the pulse size on the net acceleration. We see evidence of subcycle acceleration, with the maximum γ^f occuring for values of N less than 1. The peak value occurs at $N = 0.48$ ($\approx$ half cycle), where we get the most positive contributions from a laser field. As N increases, γ^f exponentially decreases in the tail, consistent with the average field decreasing exponentially with increasing N ($\bar{f} \sim \exp(-N^2/4)$). For values of N more than around 4 the γ factor returns to its initial value after the laser field vanishes. The right-hand plot of Figure 3.1 shows the final values of u^1 and u^3 as we vary N (e.g. when $N = 0$ then $u^\mu = (1,0,0,0)$ and when $N = 0.48$ then $u^\mu = (3.0, 2.0, 0, 2.0)$). The direction of the final velocity is confined to the x-z plane, in fact all $(u^{1,f}, u^{3,f})$ lie on the curve shown in Figure 3.1 (right).

The effect of varying N was investigated for different values of the strength parameter, a_0, and the effects of including the RR terms were studied. The results are summarised in Tables 3.1 and 3.2. Neglecting RR we see from Table 3.1 that as a_0 increases, so does the maximum acceleration. The relationship between a_0 and the maximum value of γ^f is

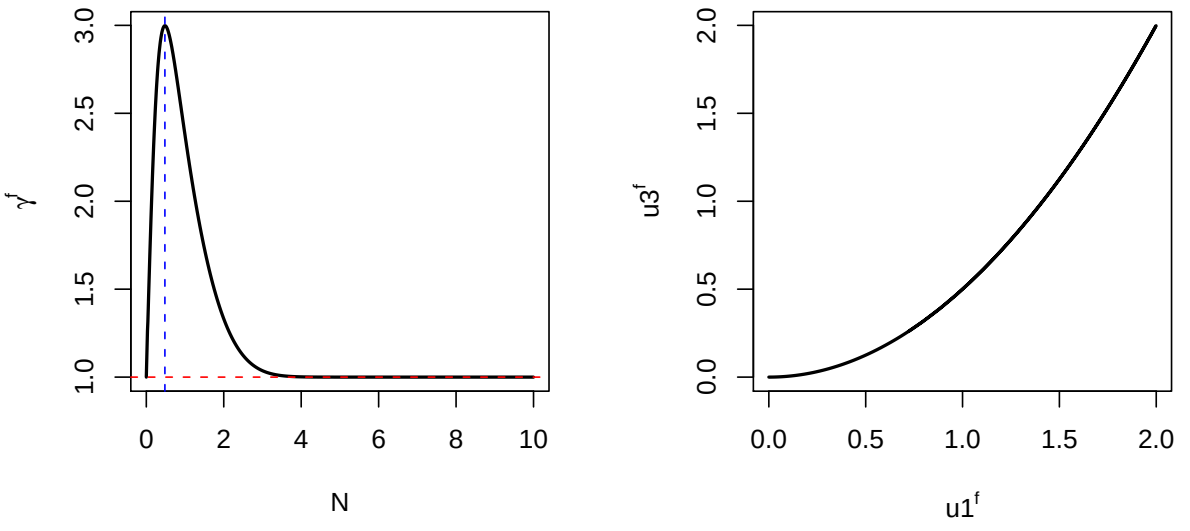

Figure 3.1: Left: final γ factor, *Right:* final velocity in the x-z plane, for varying N. A strength parameter $a_0 = 1$ and phase shift $\phi_0 = 50$ are used.

Table 3.2: Maximum difference between γ^f values with/without RR of u_0^{final}. The value of N indicates where this maximum occurs. Results shown for the two choices of ν_0 shown in Table 3.1.

	$\nu_0 = 10^{-3}$	N	$\nu_0 = 10^{-6}$	N
$a_0 = 100$	3411.418	1.21	4.503471	1.27
$a_0 = 1000$	-	-	43596.16	1.24

described by

$$\gamma^f_{max} = 1 + \frac{1}{2}\, a_0^2\, I^2_{1,max}\ , \quad I_{1,max} = I_1(N_{max})\ , \tag{3.17}$$

where I_1 is defined by

$$I_1(N) = \int_0^{s^f} d\varphi\, f(\varphi, N)\ , \tag{3.18}$$

and N_{max} is the value of N that gives maximum net energy gain. This is consistent with our analytic solution (2.59). The maximum γ^f also increases for increasing a_0 when damping is included, but at a slightly slower rate. The peak value of γ^f occurs at $N = 0.48$ for the majority of the parameters considered, however we see a slight shift to $N = 0.43$ for $a_0 = 100$, when $\nu_0 = 10^{-3}$. We note from the tables that the differences between

values obtained with and without RR are relatively small, but that where a difference does occur we find that γ^f is smaller when we account for RR. From Table 3.2 we note that the maximum difference between with and without RR does not occur at the peak. As observed in Chapter 2 we find that the impact of RR on the acceleration increases with increasing a_0.

The numerical results above are consistent with the analytic solutions. We have shown how using a short pulse one may accelerate a charge. For large values of a_0 the final velocities can reach huge values, although when N is more than around 4 or 5, γ^f is approximately equal to 1, regardless of the intensity of the field. For large values of N the positive and negative forces on the particle cancel each other out leaving zero acceleration overall, assuming a symmetric envelope. When a complete cycle is not contained within the pulse the acceleration and deceleration effects do not cancel and we are left with an overall acceleration - 'subcycle acceleration' [47]. In the case where N is approximately half of a cycle, the field is unidirectional or 'unipolar' [46] and there is no deceleration effect at all. For a perfectly symmetrical model the maximum final velocity should occur when $N \equiv 0.5$, the slight deviation found for the test case is likely due to the Gaussian envelope used. It appears that by using a half cylcle we can potentially accelerate charged particles to extremely high velocities, however we recall that there are potential experimental issues with producing such laser pulses [50]. In addition we note that we have used a pulsed plane wave to model our laser, ignoring any transverse effects such as the pondermotive forces trying to expel the charges in the transverse direction [59]. Clearly this will have some impact on our estimates of the net acceleration possible.

3.3 Sequence of Pulses

We have seen that by using a small pulse width we are able to generate acceleration. Now if we were to subject the particle to a series of these short pulses, each pulse would accelerate the particle a bit more each time. By using a series of n pulses, one can amplify the acceleration of a particle in the laser field. This concept of staging is demonstrated below. To simulate multiple laser pulses, we add a series of n phase shifted functions

together,

$$f(\phi) = -\sin(\phi) \sum_{i=1}^{n} \exp\left\{ -\frac{(\phi - (2n-1)\phi_0)^2}{N^2} \right\}. \tag{3.19}$$

To demonstrate the potential gains of this staging process, we choose a value of $N = 4$ and use a series of three pulses. We saw in Figure 3.1 that for such a choice of N, with a single pulse we achieve only minimal acceleration, in fact we obtain $\gamma^f = 1.01$. The left panel of Figure 3.2 shows a plot of $f(\phi)$ for $N = 4$ and $n = 3$, and the right panel shows the corresponding values of the γ factor. An increase in net energy is seen after each pulse duration leaving the final result, $\gamma^f = 1.03$. This is an overall improvement of three times as much energy gain than using a single pulse, which is to be expected since we have three pulses.

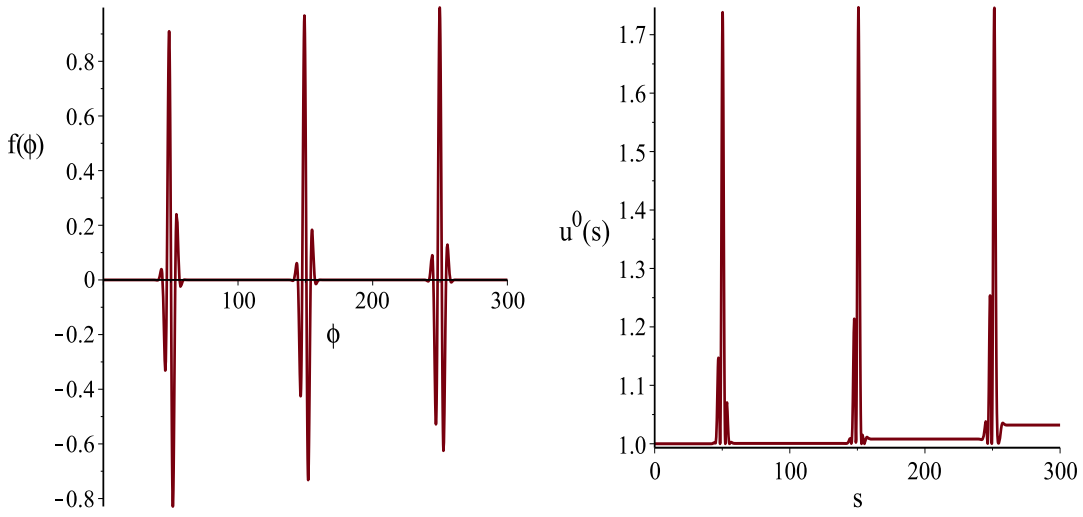

Figure 3.2: Left: Laser pulse function $f(\phi)$ from (3.19), *Right:* corresponding γ factor $u^0(s)$, for a choice of $N = 4$, $n = 3$ and $\phi_0 = 50$.

This same idea may be used even without short pulses. When we include RR terms we actually see a small amount of acceleration. We take for example the optical laser with parameters $a_0 = 3 \times 10^3$ and $\nu_0 = 10^{-6}$ used in Section 2.4. For a choice of $N = 10$ we obtain $\gamma^f = 1.042$, which was unobservable in Figure 2.8. This small γ^f may be magnified as above by using n successive pulses. We note however that our shape function (3.19) chooses the centre of each of the n pulses automatically without regard to an optimal choice of ϕ_0. In the previous section we saw how ϕ_0 is an influential parameter in determining the size of the average field. We now consider an optimum choice of the

pulse centre for each successive pulse to get maximum acceleration. Figure 3.3 shows the value of γ^f after one pulse, for varying $\phi_{0(1)}$ (where $\phi_{0(1)}$ is the centre of the first pulse) for an optical laser. The choice of carrier phase clearly has an impact on γ^f, which oscillates steadily within a fixed range. We choose our initial $\phi_{0(1)}$ such that γ^f is a maximum; for

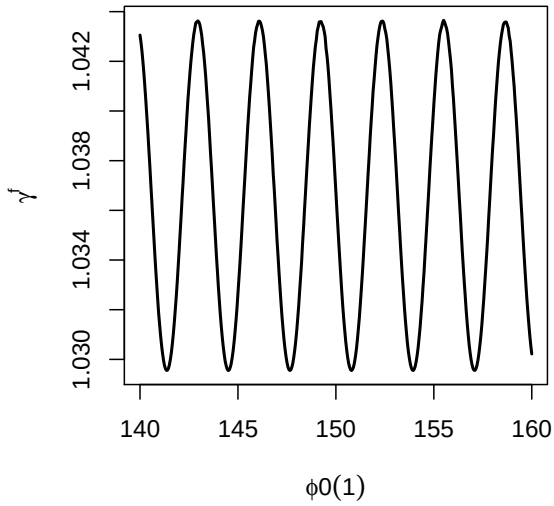

Figure 3.3: Value of γ^f for varying $\phi_{0(1)}$. Results are shown for $a_0 = 3 \times 10^3$ and $\nu_0 = 10^{-6}$, using (3.19) with $n = 1$.

our first pulse $\phi_{0(1)} = 155.5$. Let $\phi_{0(2)}$ and $\phi_{0(3)}$ be the centre of our second and third pulses respectively. The left hand panel of Figure 3.4 shows the value of γ^f expected given a range of $\phi_{0(2)}$ values for our second pulse. After choosing an appropriate peak, $\phi_{0(2)} = 124$, a fair distance from the centre of the first pulse, the process is repeated to find an optimum $\phi_{0(3)}$. The right hand panel of Figure 3.4 is a plot of γ^f against varying choices of $\phi_{0(3)}$, given our choices of $\phi_{0(1)}$ and $\phi_{0(2)}$; we choose $\phi_{0(3)} = 92.5$ for this third pulse. Using a series of three pulses with the chosen pulse centres we get a value of $\gamma^f = 1.275$ for our optical laser, achieving more than six times the gain when only one pulse was used. This idea can easily be extended to a longer chain of pulses.

Clearly this is an effective way to magnify our energy gains once an optimum pulse shape has been established, and this idea can be readily applied to the pulse shapes explored in the remaining sections of this chapter. Of course there is no reason why the n pulses must all be the same shape; there is potential for increased acceleration by using pulses

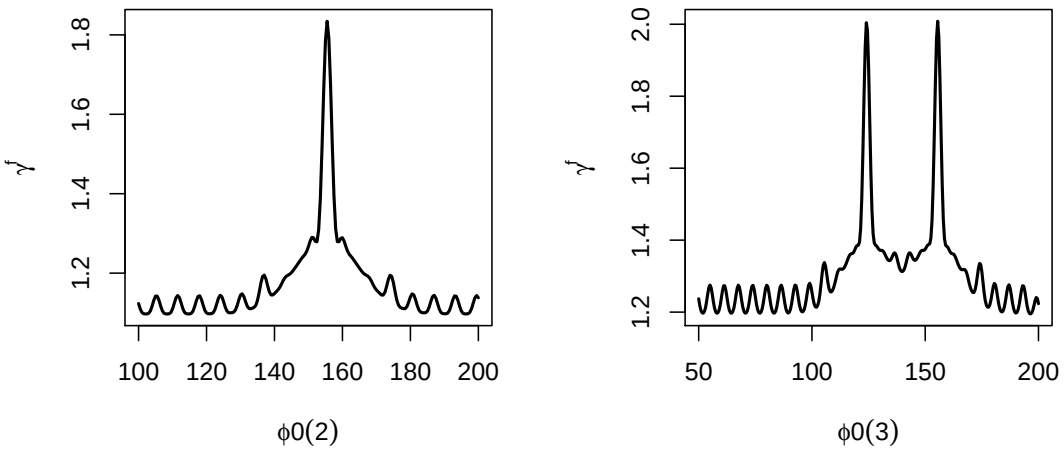

Figure 3.4: Left: Value of final γ factor for varying $\phi_{0(2)}$, given $\phi_{0(1)} = 155.5$; *Right:* Value of final γ factor for varying $\phi_{0(3)}$, given $\phi_{0(1)} = 155.5$ and $\phi_{0(2)} = 124$.

of varying shape in series too.

3.4 Pulse Shaping

In the previous sections it has been demonstrated how by using a small pulse width, a particle that is initially at rest can be accelerated to extremely high velocities. We shall now see whether this can be achieved by changing the shape of the pulse (whilst keeping N constant) even when N is reasonably large. Again, for acceleration we will require a pulse shape $f(\phi)$, such that there exists a nonzero Fourier zero mode of f, therefore a carrier phase ϕ_0 is again used below. A shape function $S(\phi)$ is introduced. We shall use

$$f(\phi) = S(\phi)\cos(\phi), \tag{3.20}$$

where

$$S(\phi) = S(a_n, b_n; \phi) = \mathrm{e}^{-\frac{(\phi-\phi_0)^2}{N^2}} \sum_{n=0}^{N} \left\{ a_n \cos\left(\frac{n(\phi-\phi_0)}{N}\right) + b_n \sin\left(\frac{n(\phi-\phi_0)}{N}\right) \right\}, \tag{3.21}$$

is the shape function. This Fourier expansion is chosen so that any shape can be made by changing a_n and b_n. We wish to find optimum values of a_n and b_n for maximum final γ

factor: $max(\gamma^f) = \gamma^f(a_n^{OPT}, b_n^{OPT})$.

Let us consider the terms in our shape function. Introducing values for the b_n terms has no effect on the overall acceleration since their positive and negative values cancel upon integration. Similarly the a_0 term does not contribute to the net acceleration. For maximum γ^f we require that $f(\phi)$ returns a positive value for as many values of ϕ as possible. Now we may form a function that only takes on positive values with a $\cos^2$ term. For example Figure 3.5 shows the pulse shape and corresponding γ factor for $f(\phi) = \exp(-(\phi-\phi_0)^2/N^2)\cos^2(\phi)$. We see that the charge is continuously accelerated and never decelerates hence huge gains can be made. In contrast to what we have seen earlier,

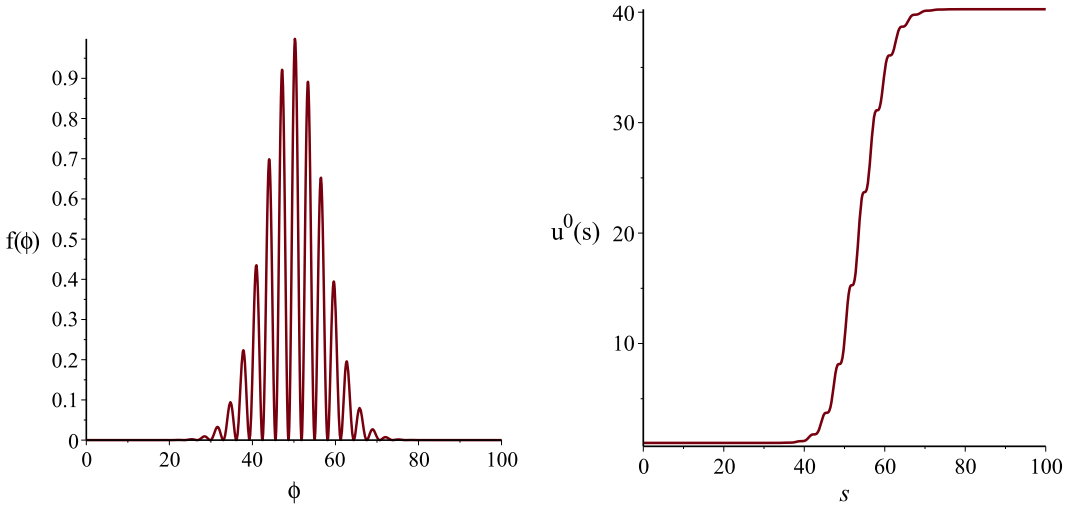

Figure 3.5: Left: Laser pulse profile $f(\phi)$ for the $\cos^2$ pulse, *Right:* corresponding γ factor $u^0(s)$.

by increasing N for this pulse shape, we get more acceleration. Taking this behaviour into account we see that if in our shape function $S(\phi)$, we choose a_N to be large then γ^f will be large. It is however unrealistic to use the $\cos^2$ pulse, since this is equivalent to having only a magnetic field, but it does give us an upper limit for potential acceleration.

Given the behaviour of the terms in our shape function (3.21), we make some minor modifications. We firstly limit our sum to stop at $n = N/2$ to avoid choosing an unrealistic pulse shape. To make life simpler we also remove the non-contributing a_0 and b_n terms, reducing our shape function to

$$S(\phi) = S(a_n, 0; \phi) = \exp\left(-\frac{(\phi-\phi_0)^2}{N^2}\right)\sum_{n=1}^{N/2} a_n \cos\left(\frac{n(\phi-\phi_0)}{N}\right). \tag{3.22}$$

Ideally to find the maximum γ^f one would test every possible combination of $a_1 = 0...K$, $a_2 = 0...K$, ..., $a_{N/2} = 0...K$, but even if only 10 possible values for each a_n were used (in reality there would be an infinite number) and $N = 10$ was used (ideally we would like to consider larger values of N), there would already be 10^{50} possible combinations! Instead we conduct a search using simulated annealing (the general method described in [60]). We search random combinations of a_n coefficients and try and improve on our γ^f result until a maximum has been found. This approach is chosen over alternative maximisation schemes as it has the advantage of searching globally for possible maxima instead of settling at local minima. Starting with the initial values a_n, we add a random number δ, sampled from the Gaussian distribution, to each of the a_n coefficients, giving $a_n^{NEW} = a_n + \delta_n$. The initial a_n coefficients are used to calculate γ and the a_n^{NEW} coefficients are substituted into our shape function to calculate γ^{NEW} (both of these being evaluated at s^f). We accept the change in the coefficients with probability $p = \min(1, \exp(\beta(\gamma^{NEW} - \gamma)))$. If γ^{NEW} is bigger than γ then we automatically accept the change since $\exp(\beta(\gamma^{NEW} - \gamma)) > 1$. If however γ^{NEW} is smaller than γ we accept the change only if $p > R$ where R is random number sampled from the uniform distribution $U(0,1)$. The method accepts these decreases in γ so as not get trapped at a local maximum. If a change is accepted then a_n becomes a_n^{NEW} and the process is repeated. The probability of accepting a worse solution decreases with time and this is controlled by reducing β after a predetermined number of steps. Depending on the number of accepted changes, we may also choose to change the size of δ, which controls the size of the search area.

After running our search for $N = 10$ our method returned the a_n coefficients shown in Table 3.3. Using these coefficients results in the laser pulse profile shown in Figure 3.6. For the parameters $a_0 = 3 \times 10^3$ and $\nu_0 = 10^{-6}$ this pulse shape generates a value of $\gamma^f = 2.63 \times 10^3$, considerable energy gain compared to our value of $\gamma^f = 1.042$ obtained using our original pulse profile (2.45). We notice that the $n = 3$ term is larger than the other terms, in fact when we altered our N we found consistently that the $n \approx N/4$ coefficient was larger than the others. This suggest that there is a particular type of pulse shape that is more effective than others at producing acceleration. Looking back at Figure 3.6 we

Table 3.3: Optimum coefficients for $N = 10$

n	a_n
1	0.190
2	0.316
3	0.991
4	0.373
5	-0.168

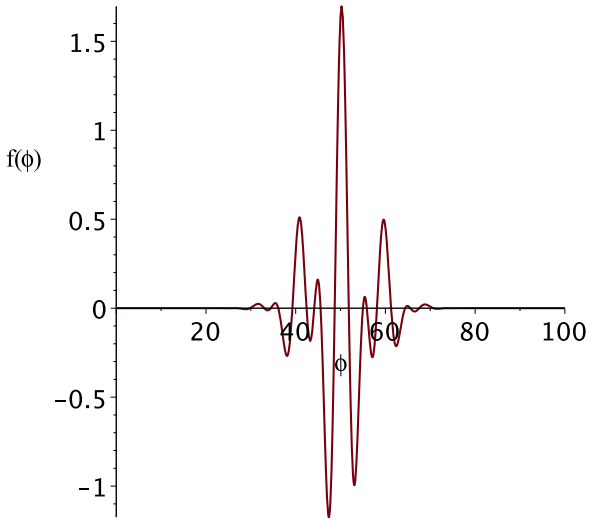

Figure 3.6: Laser pulse profile $f(\phi)$ using (3.22) and optimum coefficients for $N = 10$.

notice the beat like structure, observed when waves of slightly different frequencies are superimposed [61]. This observation leads us nicely to the final section of this chapter, where we create a pulse shape from two terms of differing frequencies.

3.5 Two-Colour Laser

Our search for an optimum pulse shape revealed that using a structure similar to a beat wave we can get acceleration. Two co-propagating laser beams are an experimentally feasible option [62] that we shall use to recreate the effect of our optimum pulse results. When two waves with slightly different frequencies are co-propagated they produce a beat structure. This breaks the symmetry of the individual waves and also allows for an overall field amplitude up to twice as large as that of the individual waves, assuming they are of the same amplitude. This feature is exploited in the design of vacuum beat wave

Table 3.4: Final γ factor values for two-colour lasers with and without RR for field stength $a_0 = 3000$.

r	$\nu_0 = 10^{-6}$	no RR
2	1.34	1.00
4	8.65×10^3	2.07×10^3
8	3.04×10^8	2.47×10^8
16	3.11×10^9	2.59×10^9

acceleration; examples are given in [63] and [64] where frequency differences $\omega_2 = 1.1\ \omega_1$ and $\omega_2 = 2\ \omega_1$ are used respectively. Our results suggest that even higher energy gains can be achieved by changing this frequency difference.

To simulate a two-colour laser we use the following function for our pulse shape,

$$f(\phi) = \exp\left(-\frac{(\phi-\phi_0)^2}{N^2}\right)\ \left(\cos(\phi) + \cos\left(\frac{\phi}{r}\right)\right), \tag{3.23}$$

where here we use the constant r as a measure of the ratio between the two frequencies. As in the previous section we use the carrier phase ϕ_0 to ensure a nonzero Fourier zero mode of f. Experimenting with different values of r we obtain the results in Table 3.4.

We note that γ^f increases as we go down the table. We also note that there is a huge difference between our results with and without RR. The electron gains a net acceleration much larger than we would expect if we neglect the RR terms. The pulse profiles for these two-colour lasers can be seen in Figures 3.7 to 3.10. For each of the pulse profiles considered we see that overall the sum of the two waves accelerate the particle more than they decelerate it giving a net acceleration. For the frequency difference $\omega_1 = 16\ \omega_2$, we see that the pulse profile approaches the $\cos^2$ result shown in Figure 3.5. The electron ends up with close to the peak energy. Using the frequencies $\omega_2 = 1.1\ \omega_1$ for comparison we obtain $\gamma^f = 1.09$ with RR accounted for, smaller than the results in Table 3.4. This method looks extremely promising for laser vacuum acceleration, it also highlights the significant impact of RR on particle motion.

The overarching theme in this chapter has been the search for a pulse shape with a nonzero

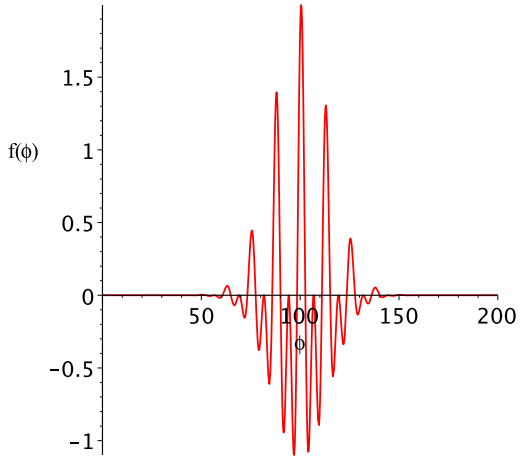

Figure 3.7: Laser pulse profile (3.23) using $r = 2$, $\phi_0 = 100$ and $N = 20$.

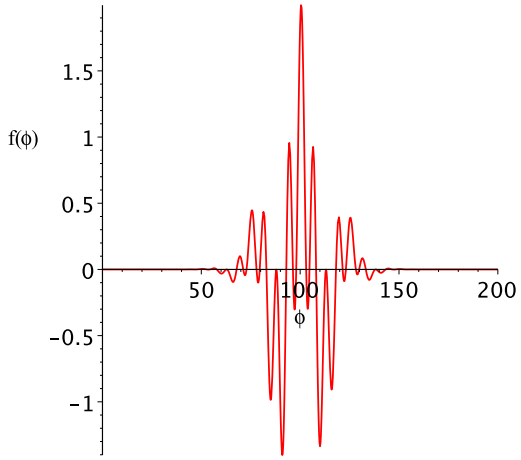

Figure 3.8: Laser pulse profile (3.23) using $r = 4$, $\phi_0 = 100$ and $N = 20$.

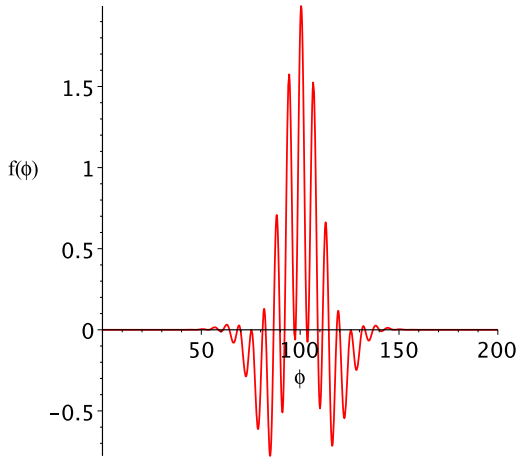

Figure 3.9: Laser pulse profile (3.23) using $r = 8$, $\phi_0 = 100$ and $N = 20$.

average field. We have seen that the two important parameters that enable a unipolar pulse are ϕ_0 and N. Choosing these wisely allows us to generate a net acceleration without the need to separate the electron from the pulse. The use of a staging process was explored,

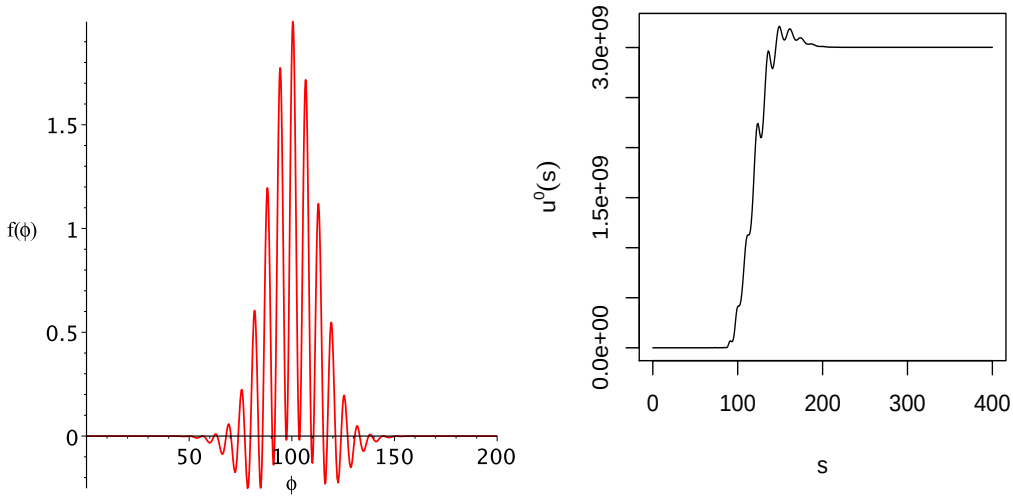

Figure 3.10: Left: Laser pulse profile (3.23) using $r = 16$, $\phi_0 = 100$ and $N = 20$. *Right:* Corresponding γ factor $u^0(s)$ when RR is accounted for.

which allowed our accelerated particle to gain more energy with the addition of each pulse. It was shown that two ways of achieving a unidirectional pulse were:

- making N so small that the pulse does not complete a full cycle; half a cycle or less allows us to get only positive contributions,
- using a $\cos^2$ pulse, a function of only positive values.

Alternatives to these two suggestions were studied in order to obtain experimentally feasible options. A search for the optimum pulse shape was conducted, which highlighted a beat like structure as a useful tool in gaining net acceleration. The idea of using beat waves was the basis of recreating an optimum pulse shape using two laser beams simultaneously. The interaction of the two different frequency pulses $\omega_2 = \omega_1/r$ resulted in highly significant energy gains for a particle initially at rest.

We note that the two individual waves that make up the two-colour laser are both unipolar and therefore the success of this method relies on the ability to produce unipolar pulses experimentally. It is still unclear as to whether a suitable pulse could be produced and there is certainly much debate around the possibility of vacuum laser acceleration. In [65] it is shown using energy conservation and Fourier analysis that a bounded source cannot create a unipolar pulse. However there are experimental results that show that by using a

unipolar-like pulse a free electron may extract energy from the electromagnetic field [42]. These unipolar-like pulses consist of a sharp tail of one polarity and a long tail of the opposite polarity. The dynamics of such a system is generally dictated by the sharp tail. Experimental results reported in [66] suggest that huge gains may be made in vacuum and despite some uncertainty over the interpretation of these results [67], they show promise in the area of vacuum laser acceleration. In fact notwithstanding concerns about producing unipolar pulses there is still on-going experimental interest in this area [10].

This chapter has focussed on the acceleration of a charged particle in electromagnetic fields. As we saw in Chapter 2, accelerating charges radiate, but we have not spent much time looking at *how* these charges radiate. This will be investigated in the following Chapter. It has also been observed in Chapters 2 and 3, that RR can significantly impact on the motion of a particle. Chapter 4 will consider how this impact may be detected experimentally.

Chapter 4

Radiation

We have established that our accelerated particles radiate and that this radiation can have significant impact on the motion of a particle. For relativistic laser matter interactions the scattered radiation is not just of the same frequency as the laser frequency. Instead we observe harmonics in the radiation [68], with each harmonic having its own angular distribution [12]. The spectrum of frequencies observed will depend on the intensity of the laser [69]. In this chapter we shall study the emitted radiation for a particle in crossed fields. We shall also attempt to identify how the spectrum of radiation may be used to observe RR effects for a pulsed plane wave. The effect of RR on nonlinear Thomson scattering was explored in [23] for an electron with an initial γ factor $\gamma_0 = 300$. Following on from our example in Chapter 2 we shall explore the effect of RR for an electron that is initially at rest.

4.1 Calculating the Spectrum of Radiation

In Chapter 2 we calculated the trajectory x^μ of a particle in an electromagnetic field, and its four-velocity u^μ. We may use these to calculate the current and thus the particle radiation. To calculate the radiation spectrum we begin with the radiation four-momentum P^μ_{rad}. Using the formula (2.28) for the energy radiated, $P^{rad}_\mu = P_\mu(A^{out}) - P_\mu(A^{in})$, it follows [29] by the use of advanced and retarded Green's functions that the four-momentum

of the radiated field may be written as

$$P_\mu^{rad} = -\frac{1}{2}\int \frac{d^4k'}{(2\pi)^3}\, sgn(k'^0)\delta(k'^2)k'^\mu\ j(k')\cdot j^*(k')\ , \tag{4.1}$$

where $j^\mu(k')$ is the Fourier transform of the current,

$$j^\mu(k') = e\int d\tau u^\mu(\tau)e^{-ik'\cdot x(\tau)}\ , \tag{4.2}$$

and $k' = \omega'(1,\mathbf{n}')$. The scattered frequency ω' and the scattering direction $\mathbf{n}'$ have been introduced. We are interested in the zero component of (4.1), the radiated energy. We therefore follow [70], and integrate (4.1) over k'^0. The energy P^0_{rad} can thus be written

$$\begin{aligned} P^0_{rad} &= -\frac{1}{16\pi^3}\int d\omega'\ d\Omega\ (\omega')^2\ j(k')\cdot j^*(k') \\ &= \int d\omega'\ d\Omega\ \omega'\ \rho(\omega',\mathbf{n}')\ , \end{aligned} \tag{4.3}$$

where we have introduced the spectral density ρ, which describes the number of photons radiated per unit frequency per unit solid angle,

$$\rho(\omega',\mathbf{n}') = \frac{d^2N_\gamma}{d\omega' d\Omega} = -\frac{\omega'}{16\pi^3}j(k')\cdot j^*(k')\ . \tag{4.4}$$

The radiation over all angles is found by integration of the spectral density over $d\Omega = \sin\theta d\theta d\phi$

$$\frac{dN_\gamma}{d\omega'} = \int d\Omega\ \rho(\omega',\mathbf{n}') = \int_0^{2\pi} d\phi\int_0^\pi d\theta\sin\theta\rho(\omega',\mathbf{n}')\ , \tag{4.5}$$

and the total radiation emitted is obtained by integrating again over ω'

$$N_\gamma = \int d\omega'\ d\Omega\ \rho(\omega',\mathbf{n}')\ . \tag{4.6}$$

The results calculated in the remaining sections will use the rescaled frequency $e^2\omega'/c\ \omega\to\omega'$, where ω is the laser frequency, so ω' will be measured in units of e^2/c. We will now study the properties of this radiation.

4.2 Analytic Investigation: Radiation for Crossed Fields

We may obtain analytic solutions for our spectrum of radiation if we consider the case of constant fields. This has been studied extensively for synchrotron radiation [71, 72] (motion on a circle [73]) and is referred to in many classical electrodynamics text books for example [22,30]. We choose to investigate the scattered radiation for motion in crossed fields, the long wavelength limit of our pulsed plane wave introduced in Chapter 2.

4.2.1 Method

The spectral density for crossed fields can be calculated by making use of Airy functions. This is possible since the trajectory of the particle in crossed fields is a cubic function. To calculate the spectral density, as defined by (4.4), we must first evaluate $j^\mu(k')$ given by (4.2). It is useful to work with lightcone coordinates since it simplifies the calculation of the spectrum considerably [74]. We use the notation

$$a^- \equiv a^0 - a^3 \; ; \quad a^+ \equiv a^0 + a^3 \; ; \quad \mathbf{a}_\perp \equiv (a_1, a_2) \; , \tag{4.7}$$

for an arbitrary four-vector a. Using this lightcone formalism allows us to equivalently write (4.2) as

$$j^\mu(k') = \frac{e}{u_0^-} \int dx^- u^\mu(x^-) \mathrm{e}^{-ik'\cdot X(x^-)}, \tag{4.8}$$

since $d\tau = dx^-/u_0^-$. Note that we now use the notation X to define the trajectory of the particle for clarity as it is a function of x^-. We find that for the $j^-(k')$ component the expression reduces to

$$j^-(k') = \frac{e}{u_0^-} \int dx^- u^-(x^-) \mathrm{e}^{-ik'\cdot X(x^-)} = e \int dx^- \mathrm{e}^{-ik'\cdot X(x^-)}, \tag{4.9}$$

since u^- is conserved. This is essentially the integral of the exponential $\exp\{-ik\cdot X(x^-)\}$. Ignoring the prime for convenience, we need to work out $k\cdot X(x^-)$.

For our choice of crossed fields we note that **E** and **B** are perpendicular and of equal strength, F. Neglecting radiation effects and using the solution of the Lorentz equation

given in (2.57) we have in terms of lightcone components

$$u^\mu = u_0^\mu - Fx^- \varepsilon^\mu + \frac{F^2 (x^-)^2}{2u_0^-} n^\mu . \tag{4.10}$$

Assuming $x_0^- = 0$, we obtain the following expression for x^μ:

$$x^\mu = \frac{1}{u_0^-} \left\{ u_0^\mu x^- - \frac{1}{2} F (x^-)^2 \varepsilon^\mu + \frac{F^2 (x^-)^3}{6u_0^-} n^\mu \right\} . \tag{4.11}$$

With the following choice of polarisation vectors, ε^μ, and propagation vectors, n, $\bar{n}$,

$$\begin{aligned} &\varepsilon^\mu = (0,1,0,0) \;\; ; \quad \varepsilon^2 = -1 \;\; ; \\ &n^\mu = (1,0,0,1) \;\; ; \quad n^2 = 0 \;\; ; \\ &\bar{n}^\mu = (1,0,0,-1) \;\; ; \quad \bar{n}^2 = 0 \;\; ; \\ &\varepsilon^\pm = 0 \; ; \; \boldsymbol{\varepsilon}_\perp = \hat{\mathbf{e}}_x \; ; \; n^+ = 2 \; ; \; n^- = 0 = \mathbf{n}_\perp \; ; \; \bar{n}^+ = 0 \; , \end{aligned} \tag{4.12}$$

we can write out the simplified equations for the components of the four-velocity of the particle,

$$u^- = u_0^- \; ; \quad u^+ = u_0^+ + \frac{F^2 (x^-)^2}{u_0^-} \; ; \quad \mathbf{u}_\perp = -Fx^- \hat{\mathbf{e}}_x \; . \tag{4.13}$$

Specialising to the case of a head-on collision, where the laser moves in the z direction and the particle in the $-z$ direction, we have the initial conditions $u_0^- = \gamma_0 (1+\beta_0)$ and $u_0^+ = \gamma_0 (1-\beta_0)$. To simplify our equations somewhat, we introduce the rapidity ζ so that $\mathrm{e}^{\pm\zeta} \equiv \gamma_0 (1 \pm \beta_0)$. Hence the components of the trajectory are

$$x^- = x^- \; ; \quad x^+ = \mathrm{e}^{-2\zeta} x^- \left(1 + \frac{1}{3} F^2 (x^-)^2 \right) \; ; \quad \mathbf{x}_\perp = -\frac{1}{2} \mathrm{e}^{-\zeta} F (x^-)^2 \hat{e}_x \; . \tag{4.14}$$

We can now calculate $k \cdot X(x^-)$,

$$k \cdot X(x^-) = \frac{k^+ x^-}{2} + \frac{k^- \mathrm{e}^{-2\zeta} x^- \left(1 + \frac{1}{3} F^2 (x^-)^2 \right)}{2} + \frac{k_x \mathrm{e}^{-\zeta} F (x^-)^2}{2} \; . \tag{4.15}$$

Let the exponent $-ik \cdot X(x^-) = -if(x^-)$ then after grouping the various powers of x^-, we

may write

$$2f(x^-) = \frac{1}{3}k^- e^{-2\zeta}F^2 \left\{ (x^-)^3 + \frac{3k_x}{k^- e^{-\zeta}F}(x^-)^2 + 3\frac{k^+ + k^- e^{-2\zeta}}{k^- e^{-2\zeta}F^2}x^- \right\}. \tag{4.16}$$

In order to make use of Airy functions we need to get rid of the quadratic term so we let $x^- \equiv y^- - k_x/k_- e^{-\zeta}F$, giving the transformed function of (4.16), $\bar{f}$, in terms of y^-

$$\begin{aligned}\bar{f}(y^-) = \frac{1}{6}k^- e^{-2\zeta}F^2 \Bigg\{ &\left(y^- - \frac{k_x}{k^- e^{-\zeta}F} \right)^3 + \frac{3k_x}{k^- e^{-\zeta}F}\left(y^- - \frac{k_x}{k_- e^{-\zeta}F} \right)^2 \\ &+ 3\frac{k^+ + k^- e^{-2\zeta}}{k^- e^{-2\zeta}F^2}\left(y^- - \frac{k_x}{k^- e^{-\zeta}F} \right) \Bigg\}.\end{aligned} \tag{4.17}$$

After careful manipulation this may be simplified to

$$\bar{f}(y^-) = \frac{1}{3}\xi^3 + \mu\xi - \lambda, \tag{4.18}$$

where we have used the following definitions for ξ, μ and λ:

$$\xi = (k^- e^{-2\zeta}F^2/2)^{1/3}y^- \ , \quad \mu = \left(\frac{k^- e^{-2\zeta}}{2F} \right)^{2/3} \ , \quad \lambda = \frac{1}{6}\frac{k_x}{(k^-)^2 e^{-\zeta}F}(k_x^2 + 3(k^-)^2 e^{-2\zeta}) \ . \tag{4.19}$$

We may write the current in terms of this transformed function

$$j^-(k) = e\int dy^- e^{-i\bar{f}(y^-)} = e\int dy^- \exp\left\{ -i\left(\frac{1}{3}\xi^3 + \mu\xi \right) \right\} \exp\{i\lambda\}. \tag{4.20}$$

Let $\kappa = (k^- e^{-2\zeta}F^2/2)^{1/3}$ then $\xi = \kappa y^-$ and $d\xi/\kappa = dy^-$, hence

$$\begin{aligned} j^-(k) &= \frac{e}{\kappa}e^{i\lambda}\int d\xi \exp\left\{ -i\left(\frac{1}{3}\xi^3 + \mu\xi \right) \right\} \\ &= \frac{2e\sqrt{\pi}}{\kappa}\,\mathrm{Ai}(\mu)e^{i\lambda} \quad \sim \mathrm{K}_{1/3} \ , \end{aligned} \tag{4.21}$$

where the standard identity for the Airy function Ai (see e.g. [75]) has been used. The modified Bessel functions $K_{1/3}$ and $K_{2/3}$ are sometimes preferred to the use of these Airy functions (see e.g. [30]), where they are directly proportional to Ai and Ai$'$ respectively.

Using what we know about $j^-(k)$ we can now calculate $j_x(k)$ too. We have

$$j_x(k) = \frac{e}{u_0^-}\int dx^- u_x(x^-)\mathrm{e}^{-if(x^-)}. \tag{4.22}$$

Now after substituting our expression for $u_x(x^-)$ in (4.22) we may rewrite $j_x(k)$ in terms of y^-

$$j_x(k) = -\frac{eF}{\mathrm{e}^{\zeta}}\int dy^- y^- \mathrm{e}^{-i\bar{f}(y^-)} + \frac{ek_x}{k^-}\frac{2\sqrt{\pi}}{\kappa}\mathrm{e}^{i\lambda}\ \mathrm{Ai}(\mu). \tag{4.23}$$

Consider the first term on the RHS of this equation,

$$-\frac{eF}{\mathrm{e}^{\zeta}}\int dy^- y^- \mathrm{e}^{-i\bar{f}(y^-)} = -\frac{eF}{\mathrm{e}^{\zeta}}\frac{\mathrm{e}^{i\lambda}}{\kappa^2}\int d\xi\ \xi \exp\left\{-i\left(\frac{1}{3}\xi^3+\mu\xi\right)\right\}. \tag{4.24}$$

Note the similarity between (4.21) and (4.24), the only difference between the integrands being the additional ξ term in (4.24). Partially differentiating the integral in (4.21) with respect to μ we see that

$$\frac{\partial}{\partial\mu}\int d\xi \exp\left\{-i\left(\frac{1}{3}\xi^3+\mu\xi\right)\right\} = \int d\xi(-i\xi)\exp\left\{-i\left(\frac{1}{3}\xi^3+\mu\xi\right)\right\}. \tag{4.25}$$

It follows therefore that

$$\int d\xi\ \xi \exp\left\{-i\left(\frac{1}{3}\xi^3+\mu\xi\right)\right\} = 2\sqrt{\pi}i\ \mathrm{Ai}'(\mu)\ , \tag{4.26}$$

where the prime denotes partial differentiation with respect to μ. We hence find the following expression for $j_x(k)$,

$$j_x(k) = \frac{2e\exp(i\lambda)\sqrt{\pi}}{\kappa}\left\{\frac{k_x}{k^-}\ \mathrm{Ai}(\mu) - \frac{iF}{\mathrm{e}^{\zeta}\kappa}\ \mathrm{Ai}'(\mu)\right\} \quad \sim \mathrm{K}_{2/3}\ . \tag{4.27}$$

Now we have expressions for both $j^-(k)$ and $j_x(k)$ we have enough information to calculate the spectral density. We need to calculate the scalar product $j\cdot j^*$, which using light-cone coordinates can be written

$$j\cdot j^* = \frac{j^+ j^{-*}}{2} + \frac{j^- j^{+*}}{2} - \mathbf{j}_\perp\cdot\mathbf{j}_\perp^*\ . \tag{4.28}$$

However we can make life simpler by eliminating j^+ using the continuity equation in k-space, $k \cdot j = 0$,

$$j^+ = \frac{2\mathbf{k}_\perp \cdot \mathbf{j}_\perp - k^+ j^-}{k^-} \ . \tag{4.29}$$

We obtain

$$j \cdot j^* = 2\frac{\mathbf{k}_\perp}{k^-} \cdot \Re[\mathbf{j}_\perp \ j^{-*}] - \frac{k^+}{k_-}|j^-|^2 - |\mathbf{j}_\perp|^2 \ . \tag{4.30}$$

Noting that $j_y = 0$ for our choice of $\boldsymbol{\varepsilon}_\perp = (1,0)$, we have the following expression for the spectral density,

$$\rho(\omega', \mathbf{n}') = \left(-\frac{\omega'}{16\pi^3}\right)\left(2\frac{k_x}{k^-} \cdot \Re[j_x \ j^{-*}] - \frac{k^+}{k_-}|j^-|^2 - |j_x|^2\right) \ . \tag{4.31}$$

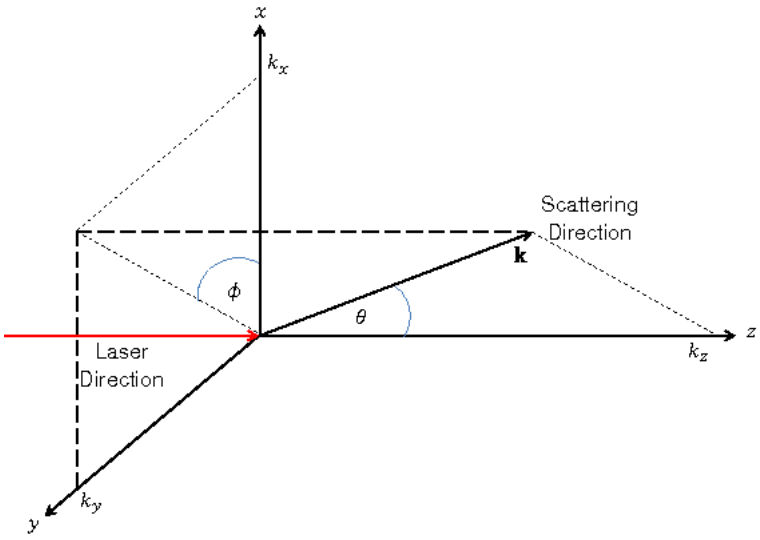

Figure 4.1: Geometry of the scattered radiation.

Our choice of scattering angles is illustrated in Figure 4.1, showing

$$\begin{aligned} k_x &= \omega' \sin(\theta)\cos(\phi) \\ k^- &= \omega'(1-\cos(\theta)) \\ k^+ &= \omega'(1+\cos(\theta)) \ . \end{aligned} \tag{4.32}$$

We can see that setting $\theta = \pi$ simplifies things somewhat. This means that $k^+ = k_x = 0$

and $k^- = 2\omega'$, hence

$$\rho(\omega', \theta = \pi) = \frac{\omega'}{16\pi^3}|j_x|^2 \,, \tag{4.33}$$

where ρ is now independent of j^-. This is the spectral density in the opposite direction of the laser (back scattering). If we choose to look in the direction of the laser (forward scattering), $\theta = 0$, then $k^+ = 2\omega'$ and $k_x = k^- = 0$; we find that ρ tends to infinity due to division by zero. This observation is consistent with [46] where they saw 'soft and collinear' divergence (usually associated with massless particles) when $k'_\mu \propto k_\mu$. The reason for such divergence in these crossed fields is due to the infinite constant electric field, which will accelerate the incoming particle to the speed of light, hence its final state being effectively 'massless' [46]. We note however that for the purpose of experiment one would not be looking at this region since any detector placed in front of the laser would be destroyed anyway.

4.2.2 Results

We begin by looking at the distribution of radiation over a range of frequencies, holding our angle fixed. Figure 4.2 shows the spectral density for various initial γ factors, γ_0. We see that as γ_0 increases the amount of radiation increases. The peak emitted frequency is also Doppler shifted to higher frequencies as γ_0 is increased. This shift is expected when the electron moves towards the laser and is an important source of X-rays and gamma rays [76]. For all three choices of γ_0 we see the same general type of behaviour for varying ω', the familiar curve as seen for synchrotron radiation [30].

Next we choose a fixed frequency and angle ϕ and study the spectrum for varying angle θ. Results are shown in Figure 4.3 (left) and suggest that most of the photons are radiated in the direction of the laser (note that the horizontal axis starts at $\pi/8$ due to the infinity at zero). We repeat our calculation for fixed frequency and angle θ and this time vary ϕ. Figure 4.3 (right) shows the symmetrical distribution of photon scattering in the transverse directions. The plot is vertically stretched for increasing γ_0, showing more spread for higher γ factors. Maxima and minima however, occur in the same place (in the *y*-*z* plane) for each γ_0 considered. We may integrate over all ϕ to see the effect of varying θ. Figure

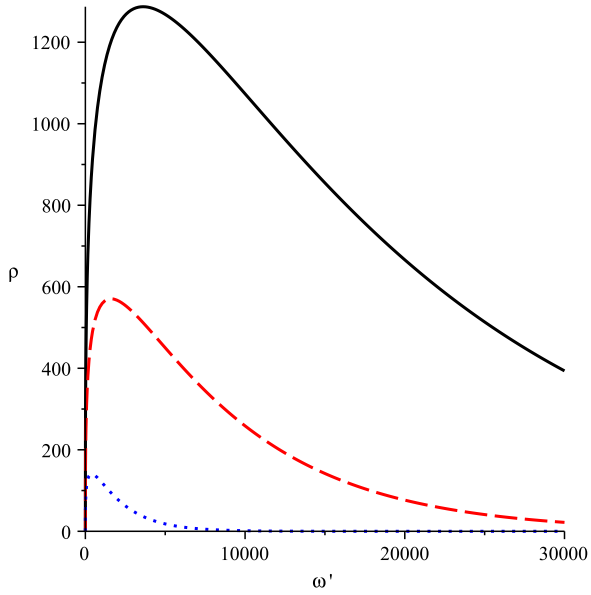

Figure 4.2: Spectral density, ρ, for varying ω' and fixed angles $\theta = \pi/8$ and $\phi = \pi/2$. The solid black line represents results for $\gamma_0 = 15$, the dashed red line for $\gamma_0 = 10$, and the dotted blue line for $\gamma_0 = 5$.

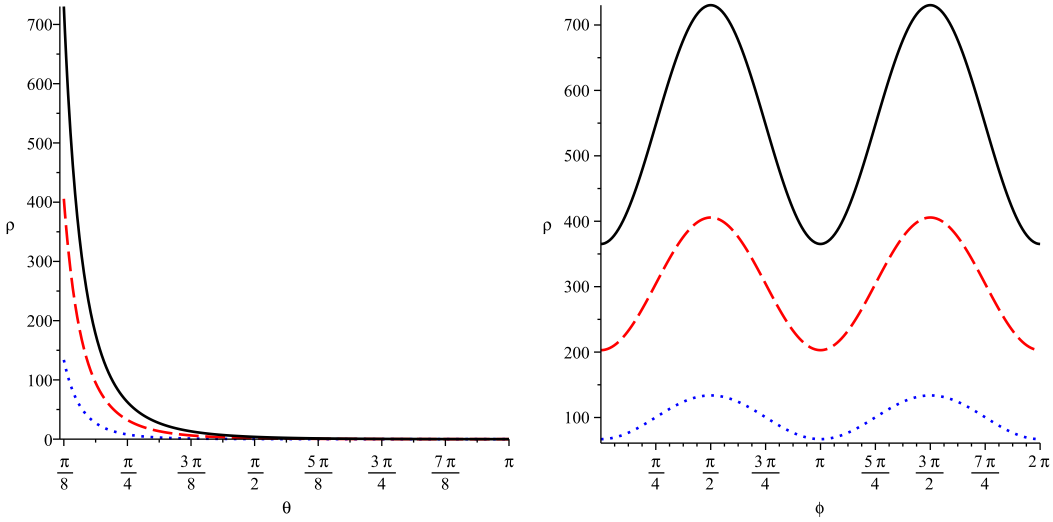

Figure 4.3: Left: Spectral density, ρ, for varying θ and fixed $\omega' = 200$ and $\phi = \pi/2$. *Right:* Spectral density for varying ϕ and fixed $\omega' = 200$ and $\theta = \pi/8$ (colours and line types as in Figure 4.2).

4.4 shows the integrated spectral density for a fixed frequency. This plot differs from Figure 4.3 (left) only by the fact that we have a larger number of radiated photons since we have summed over all ϕ.

In order to establish how ρ changes as we change frequency and angle together, we produce the surface plots shown in Figures 4.5 and 4.6 . In Figure 4.5 we hold the angle θ fixed and consider the spectral density as a function of ω' and ϕ. We see that the shape

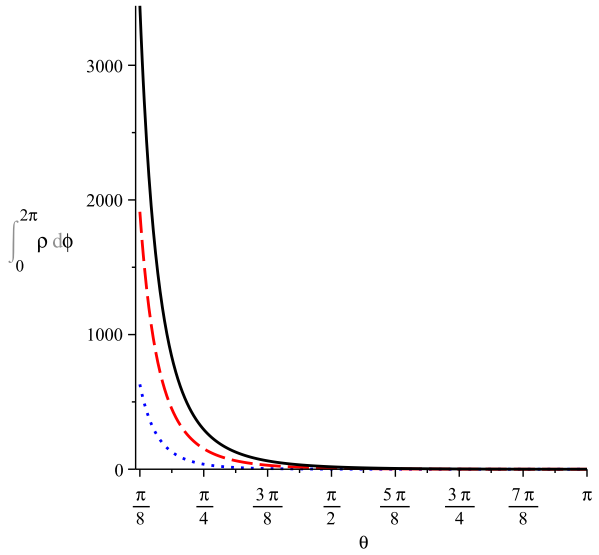

Figure 4.4: Spectrum of radiation (over all ϕ), for varying θ and fixed $\omega' = 200$ (colours and line types as in Figure 4.2).

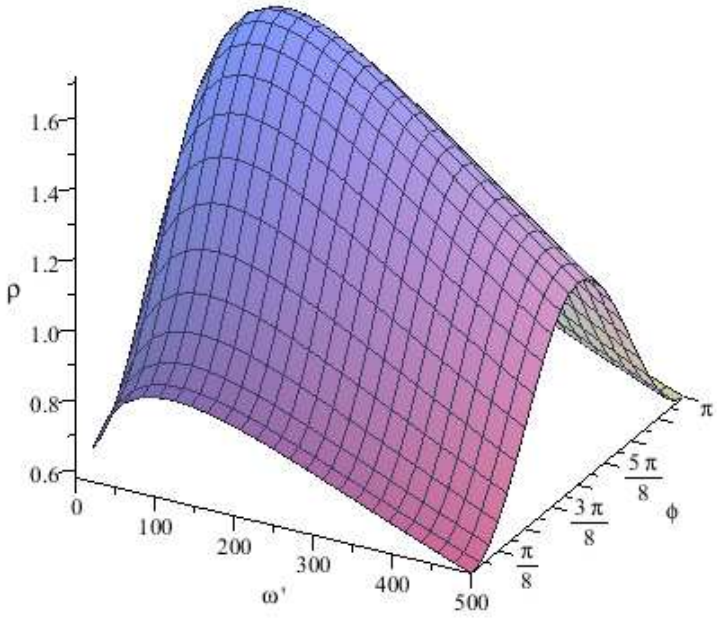

Figure 4.5: Spectral density, ρ, for varying ω' and ϕ ($\theta = \pi/2$).

of the distribution of radiated photons for vaying ϕ is unchanged for changing frequency. Similarly in Figure 4.6, where we fix ϕ and vary ω' and θ, we see as before that as θ tends to zero we get larger values, but the radiation has the same shaped distribution for all θ as ω' varies. If we choose to look at a fixed scattering frequency, we may investigate

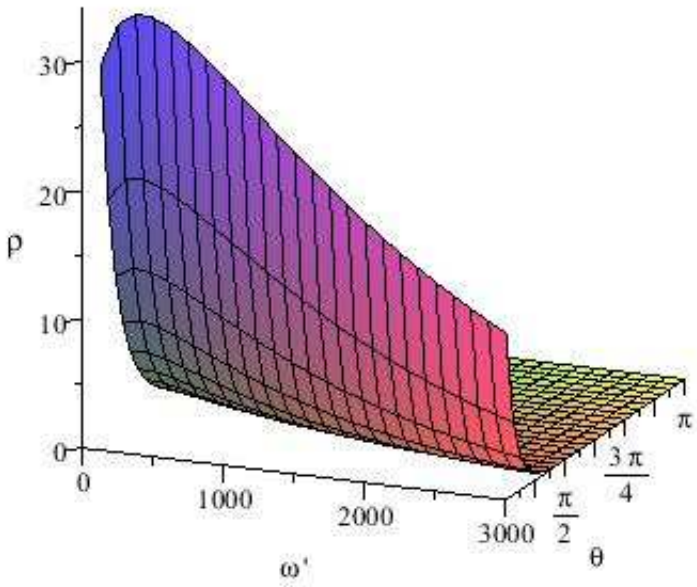

Figure 4.6: Spectral density, ρ, for varying ω' and θ ($\phi = \pi/2$).

how ρ changes as we vary the two angles together. This is shown in Figure 4.7. Again we

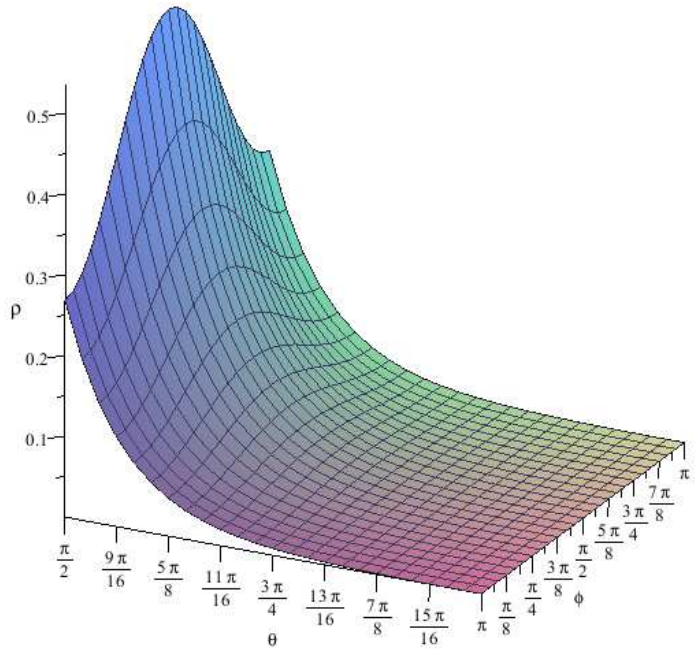

Figure 4.7: Spectral density, ρ, for varying θ and ϕ ($\omega' = 1000$).

see that varying the angle θ does not impact on the shape of the distribution of radiation

over ϕ.

Since we are looking at the distribution of photons radiated over the angles θ and ϕ it is useful to look at our results in polar plots. The left hand panel of Figure 4.8 shows the distribution of radiation over θ for fixed ω' and ϕ. Again we see how the spectral

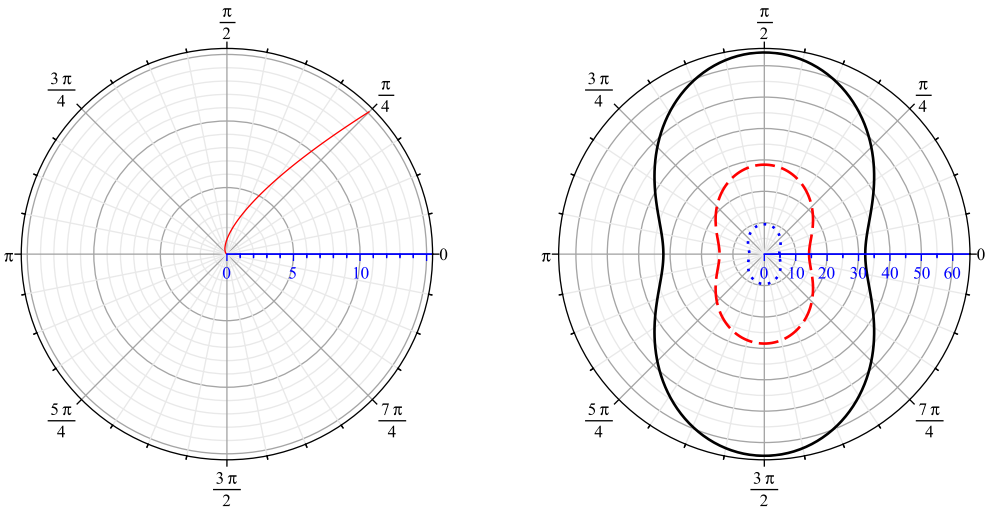

Figure 4.8: Left: Polar plot of the spectral density, ρ for varying θ and fixed $\omega' = 0.1$ and $\phi = \pi/2$. *Right:* Polar plot of the spectral density, ρ for varying ϕ (fixed $\omega' = 100$). The solid black line represents results for $\theta = \pi/5$, the dashed red line for $\theta = \pi/4$, and the dotted blue line for $\theta = \pi/3$.

density increases as θ decreases. Looking at the radiation over ϕ for a fixed frequency we produce the plot shown in Figure 4.8 (right). Here we see the radiation for three choices of θ: $\theta = \pi/5, \pi/4, \pi/3$. Most photons are radiated where ϕ is close to $\pi/2$ or $3\pi/2$ and the least photons are radiated where ϕ is close to zero or π. We get the same structure for each of the choices of θ, but as before we see that the magnitude of ρ is larger for a smaller choice of angle θ.

This analytic approach has allowed us to explore in quite some detail the spectrum of radiation for a charged particle in constant crossed fields. However if we are to learn more about the spectrum for our model of a laser pulse, we must resort to numerics to evaluate our integrals.

4.3 Numerical Investigation

Using the Gauss-Legendre method (see e.g. [75]) to numerically integrate the nested integrals contained in (4.4) it is possible to evaluate the spectrum for time dependent fields such as a pulsed plane wave, considered in the previous chapters. Radiative reaction can also be accounted for with the same method.

4.3.1 Current Conservation

When calculating $j^{\mu}(k')$ as defined by (4.2), the choice of limits of integration have to be carefully chosen to comply with current conservation. The integrand should be integrated over all time, however if we select cut-off points (which we need to do for the numerical approximation) we need to ensure that current is conserved at the start and end points. If the limits are not chosen appropriately then we define a situation where a particle comes into existence at a certain point in time with a particular current and vanishes again with another current. We require

$$\begin{aligned} \exp(-ik'\cdot x(\tau_U)) &= \exp(-ik'\cdot x(\tau_L)) \\ \Rightarrow k'\cdot x(\tau_U) &= k'\cdot x(\tau_L) + 2n\pi \ , \end{aligned} \tag{4.34}$$

where τ_L and τ_U are the lower and upper limits for τ. If we let $\tau_L = 0$ then $k'\cdot x(\tau_L) = 0$ and so we must ensure that $k'\cdot x(\tau_U) = 2n\pi$. Using the bisection method (see e.g. [60]), τ_U is varied until it satisfies $k'\cdot x(\tau_U) = 2n\pi$. The continuity equation, $k'\cdot j(k') = 0$, can be employed to eliminate j^0 [70] in (4.4) to give

$$\rho(\omega', \mathbf{n}') = \frac{\omega'}{16\pi^3}|\mathbf{n}'\times\mathbf{j}(k')|^2 \geq 0 \ . \tag{4.35}$$

This alternative expression imposes current conservation on our results and also requires less computational effort to calculate since j^0 no longer needs evaluating. In fact by using (4.35) the bisection method is not required and for this reason this simplified definition for spectral density will be used for the numerical calculations. The limits are restricted to the duration of the pulse since there is no acceleration outside of this range and hence

no radiation. An alternative way of dealing with the issue of the limits of integration and current conservation is outlined in [46] where values in the range $[-\infty, \tau_L]$ and $[\tau_U, \infty]$ cancel, leaving $j^\mu(k')$ as an integral over the pulse duration only.

4.3.2 Crossed Fields

Having evaluated the spectral density for crossed fields analytically, ideally we would wish to compare our analytic solutions to results obtained numerically as we did with our solutions of the LL equation. However, the infinite extent of the constant crossed fields presents problems for our numerical calculations - we need limits for our integrals.

A finite analytical solution to the unbounded integrals was possible because the crossed fields effectively decelerated the particle from the speed of light in the infinite past, and then re-accelerated it in the infinite future [46]. This leads to cancellations that do not occur for our numerical approach.

The infinite limits however are somewhat unphysical. We instead choose to use our numerical method to model crossed fields of finite duration T, starting from time $= 0$. The results for a choice of increasing T are shown in Figure 4.9. As T is increased, the amount of radiation increases. The spectral density is therefore scaled down by the $max(\rho)$ in the figure. We see an increased spread of the frequencies and a shift of the peak towards higher frequencies as the duration decreases.

4.3.3 Pulsed Plane Wave

We use our numerical approach to calculate the spectrum of radiation for the linearly polarised pulse with field strength $F^{\mu\nu}(\phi) = a_0 f(\phi) f^{\mu\nu}$, where

$$f = -\exp\left\{-\frac{(\phi-\phi_0)^2}{N^2}\right\} \sin(\phi)\,, \tag{4.36}$$

i.e. the pulse studied in Section 2.2. The angles θ and ϕ are defined by Figure 4.1 as with the analytic investigation. To get an idea of the basic properties of the spectrum for our laser pulse we begin by neglecting RR and use the strength parameter $a_0 = 1$. Throughout this section we will assume that the particle is initially at rest. We start by looking at the

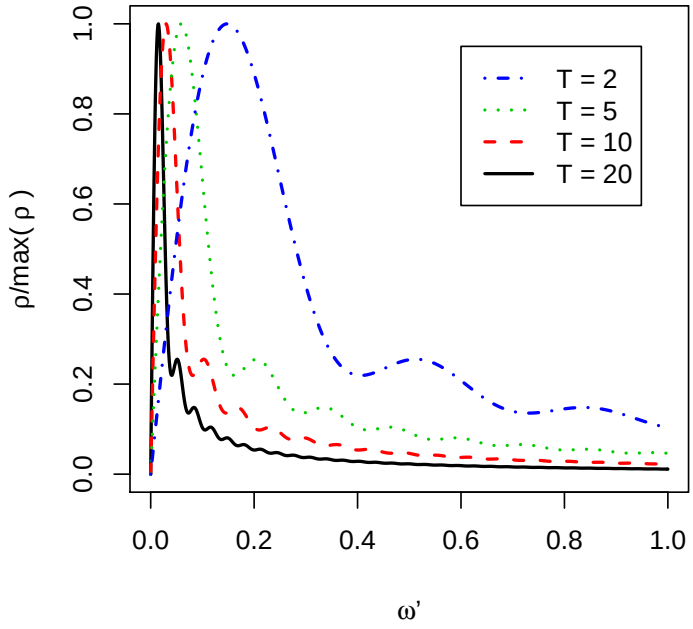

Figure 4.9: Rescaled spectral density as a function of scattered frequency ($\gamma_0 = 5$, $\theta = \pi/8$, $\phi = \pi/2$).

distribution of radiation over the frequencies, for fixed emission angles. In Figure 4.10 we set the angles to zero and observe a clear peak in the spectral density at $\omega' = 1$. ρ disappears outside of the range roughly $0.5 < \omega' < 1.5$. This single peak for the forward direction of the laser suggests that radiation scattered in this direction is emitted with the laser frequency, consistent with the results in [11].

We look at the spectral density as a function of θ in Figure 4.11 (left) and ϕ in Figure 4.11 (right). We find as expected, and as we saw in the analytic crossed field example, that ρ is highest as we get closer to the forward direction ($\theta = 0$). However we see in this case that the number of photons radiated tends to be relatively large in the backward direction too. In Figure 4.11 (right) we see that a maximum occurs when $\phi = \pi/2$, a feature that we observed when looking at the spectrum for crossed fields also.

By looking at surface plots of the spectral density we can get a clearer picture of how the spectrum changes as we vary its parameters simultaneously. We see in Figure 4.12 how the number of peaks for varying frequency increase as θ approaches π. We compare our results with Figure 2 in [77] and Figure 6 in [78], which demonstrate similar qualitative

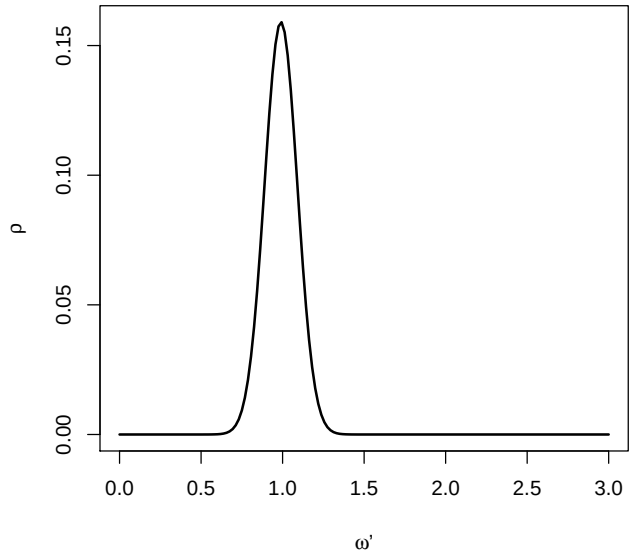

Figure 4.10: Spectral density, ρ, for varying ω' ($\phi = 0, \theta = 0$).

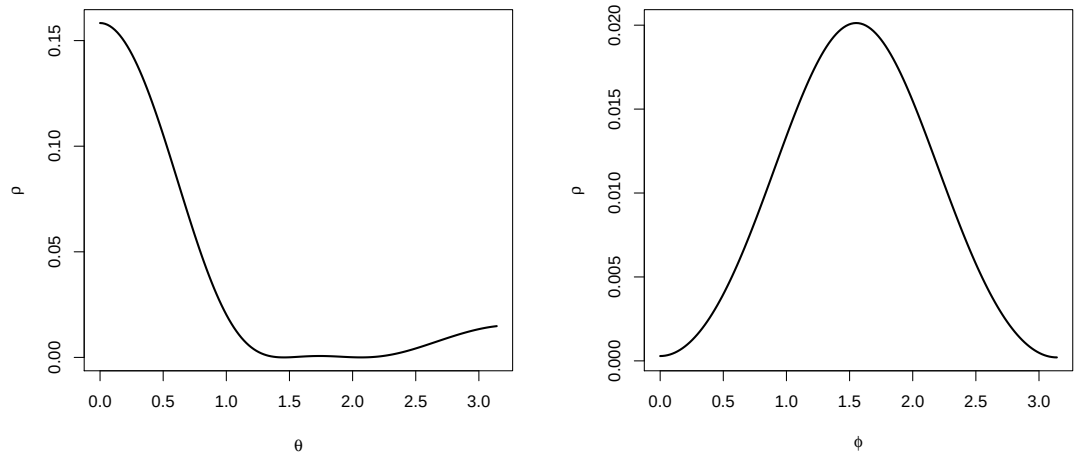

Figure 4.11: Left: Spectral density, ρ, for varying θ ($\phi = 0, \omega' = 1$). *Right:* Spectral density, ρ, for varying ϕ ($\theta = \pi/2, \omega' = 1$).

features for their choice of linearly polarised laser pulse. In Figure 4.13 we see clearly a symmetrical distribution of radiated photons for varying ϕ for all frequencies. The basic distribution of radiation over the angle θ remains largely unchanged by varying ϕ as we observe in Figure 4.14.

We wish to look for radiative reaction in the spectrum and so we must now look at larger values of a_0 where RR is expected to have a significant impact. Using the values consid-

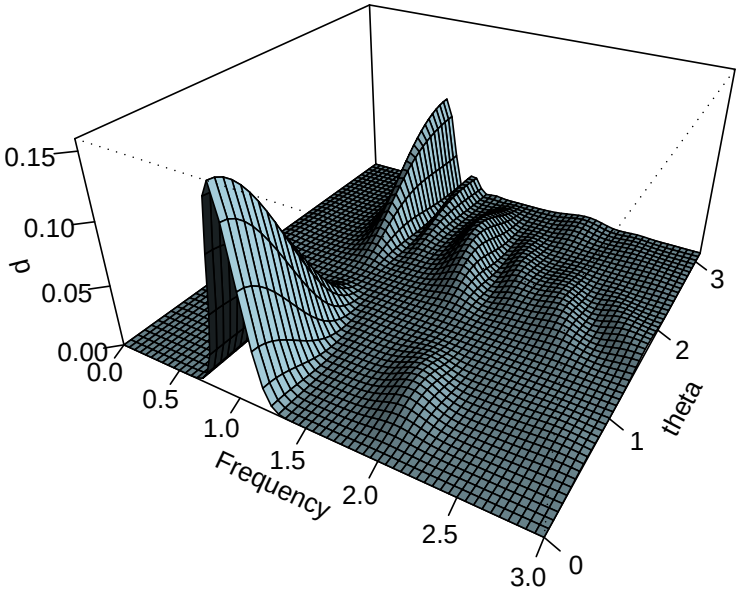

Figure 4.12: Spectral density, ρ, for varying ω' and θ ($\phi = 0$).

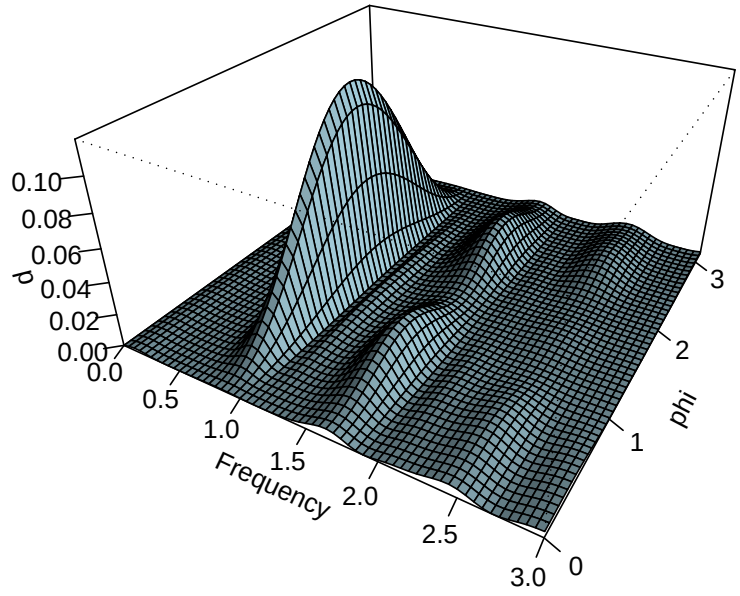

Figure 4.13: Spectral density, ρ, for varying ω' and ϕ ($\theta = \pi/2$).

ered previously, we look at the spectral density when $a_0 = 10$ and $a_0 = 3000$ both with and without RR. Plots of $\rho(\omega', \mathbf{n}')$ against frequency are shown in Figure 4.15, where $\phi = 0$ and $\theta = 0$. We see that there is little impact of RR for $a_0 = 10$, but that the maximum difference occurs at the peak. There is a significant effect seen when we look at the optical laser; again the maximum difference occurs at the peak where we see a significant

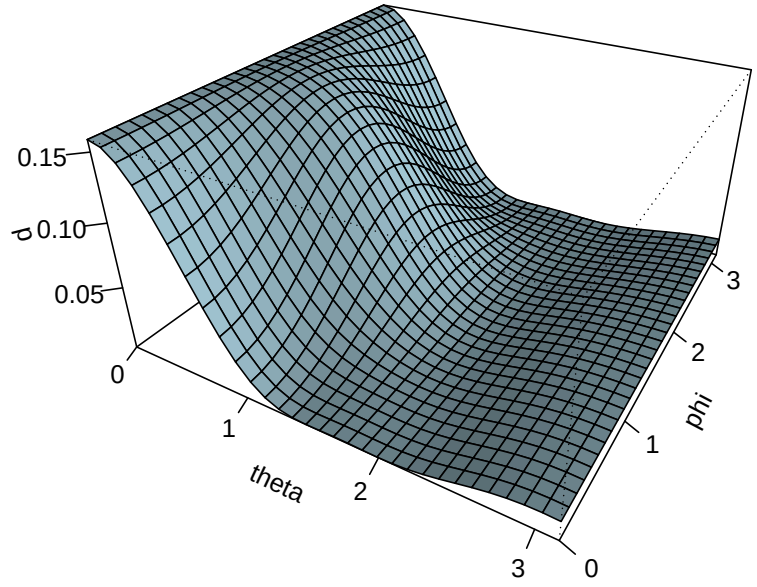

Figure 4.14: Spectral density, ρ, for varying θ and ϕ ($\omega' = 1$).

increase in the calculated number of photons radiated. We also observe a slight redshift of the scattered frequency with respect to the laser frequency when we account for RR as detected in [79].

Our results appear to contradict those found in [23] where the RR effect was seen to reduce the scattered radiation. However the results in their paper concern a head on collision rather than the electron initially at rest. As noted in Section 2.4, such a difference is to be expected for these different initial conditions. We convince ourselves that the results make sense physically by recalling our observations in Section 2.4. When RR was included in our calculations we saw the electron accelerate more than when RR was neglected. Larmor's formula tells us that radiation is proportional to the acceleration squared; we therefore expect more radiation when we include the radiative terms. For the purpose of experiment these results will not help us to establish the RR effect on the spectrum. In practice it would not be possible to put a detector directly in front of the laser to observe these results since, as stated earlier, the detector would just be destroyed. We therefore must consider alternative angles to investigate.

Choosing $\theta = \pi/4$ and $\omega' = 1$, the spectral density for $a_0 = 10$ has been plotted as a function of ϕ in Figure 4.16 (left). Interestingly for this choice of θ we get less photons radi-

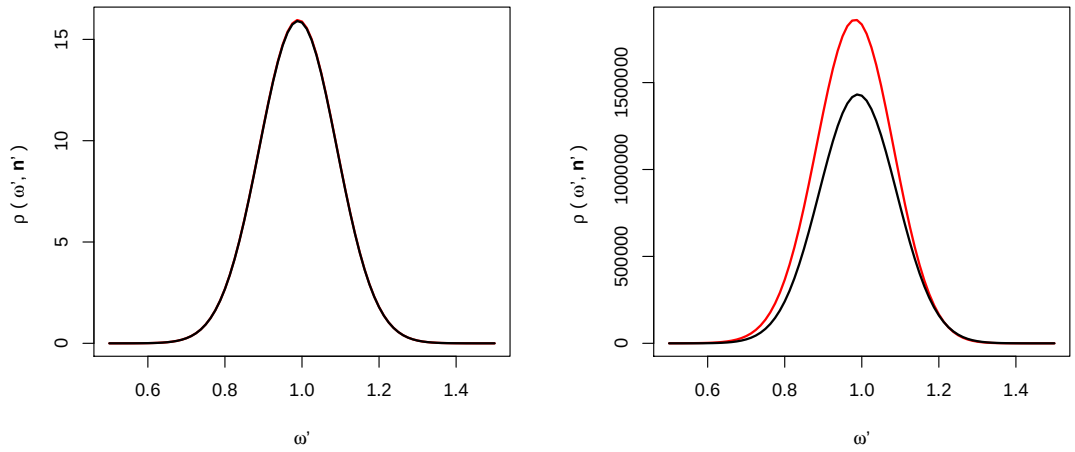

Figure 4.15: Left: Plot of spectral density against frequency for $a_0 = 10$, red line = with RR ($\nu_0 = 10^{-3}$), black line = without RR. *Right:* Plot of spectral density against frequency for $a_0 = 3000$, red line = with RR ($\nu_0 = 10^{-6}$), black line = without RR. ($\phi = 0$ and $\theta = 0$)

ated when we include the radiative reaction terms than when they are ignored. Although

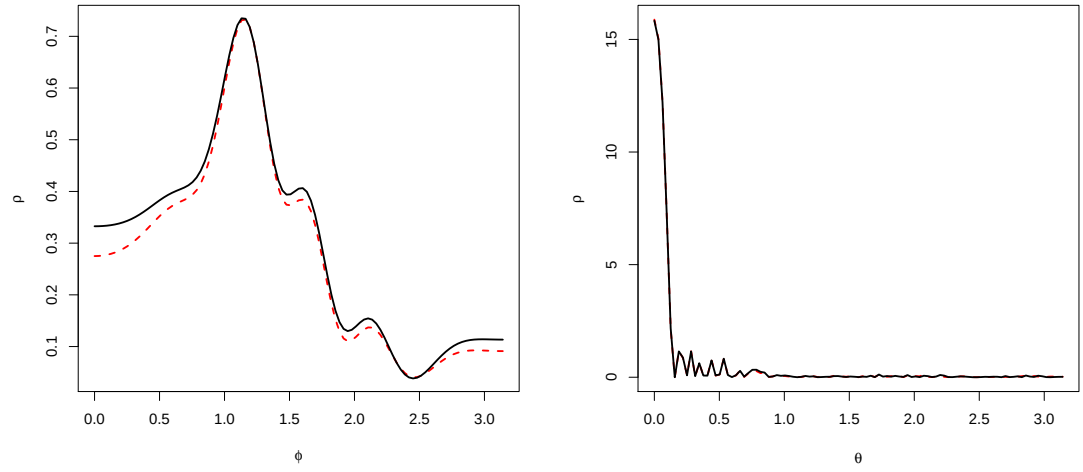

Figure 4.16: Left: Plot of spectral density against ϕ for $a_0 = 10$ (using $\theta = \pi/4$, $\omega' = 1$). *Right:* Plot of spectral density against θ for $a_0 = 10$ (using $\phi = 0$, $\omega' = 1$). Red dashed line = with RR ($\nu_0 = 10^{-3}$), black solid line = without RR.

no obvious effect of radiative backreaction can be observed from the right hand panel of Figure 4.16 (the lines with and without RR in the plot are indistinguishable), we see that even at $a_0 = 10$ the plot of spectral density as a function of θ becomes extremely oscillating. We compare this observation to the results in [77] where an increased structure is

seen as a_0 is increased; this is seen even for small values of a_0 ($a_0 \leq 2$). [76] suggests that for a high intensity laser we should expect strong oscillations in the spectrum. Looking at the results in [23] it would seem that indeed for larger a_0 values such as $a_0 = 15$ and $a_0 = 30$ the spectrum becomes extremely oscillatory. Our results for $a_0 = 10$ do not seem to have any obvious structure, which shows signs of potentially chaotic behaviour. This will be investigated further before we attempt to identify RR effects.

4.3.3.1 Chaotic Behaviour

If we look at the spectral density as a function of θ in the range $[0, \pi]$ when $\omega' = 1$ and $\phi = 0$ we see that there is an increased structure in the spectrum for larger values of a_0. Even increasing a_0 from 1 to 5 allows us to see a dramatic change in the number of oscillations. Figure 4.17 shows the transition from the smooth curve where $a_0 = 1$ to the oscillating curve when $a_0 = 5$.

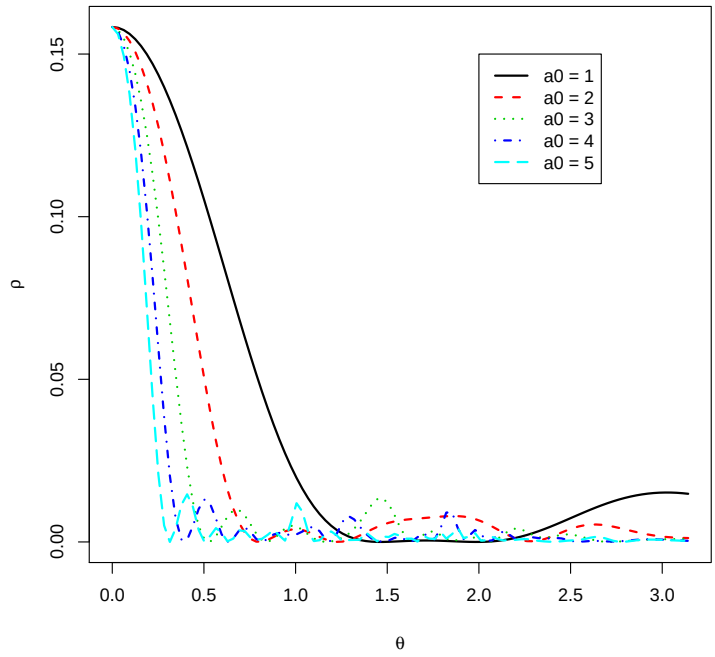

Figure 4.17: Spectral density, ρ (scaled down by a factor of a_0^2), as a function of the angle θ, shown for $a_0 = 1, 2, 3, 4, 5$.

When we set $\theta = 0$ and vary ω', we do not get any oscillating behaviour even when a_0 is increased to very large values. We just get a single peak centred around $\omega' = 1$. It can be seen that the only change is an increase by a scale factor of a_0^2 in the spectral density;

after scaling, the results are identical for all choices of field strength. Our observation is consistent with the statement in [11], which says that the radiation spectrum observed for $k' \propto k$ i.e. exactly in the forward direction of the laser, has one peak at $\omega' = \omega$, regardless of the velocity of the electron or the laser intensity.

Upon studying the spectrum of radiation for a range of a_0 values it was seen that as the strength of the laser increased so did the number of oscillations in the spectral density (for $\theta \neq 0$). When a_0 is particularly large, $a_0 = 100$ say, the spectral density appears to show signs of chaotic behaviour. Choosing a value of $a_0 = 100$ and exploring the spectral density for fixed $\phi = 0$ and $\theta = \pi/4$, we produce the results shown in Figure 4.18. The spectral density when RR is both ignored and accounted for is shown on the left hand panel; both lines in the figure show chaos-like fluctuations even over the small range of ω' values shown. The results obtained with and without RR seem to be completely unrelated

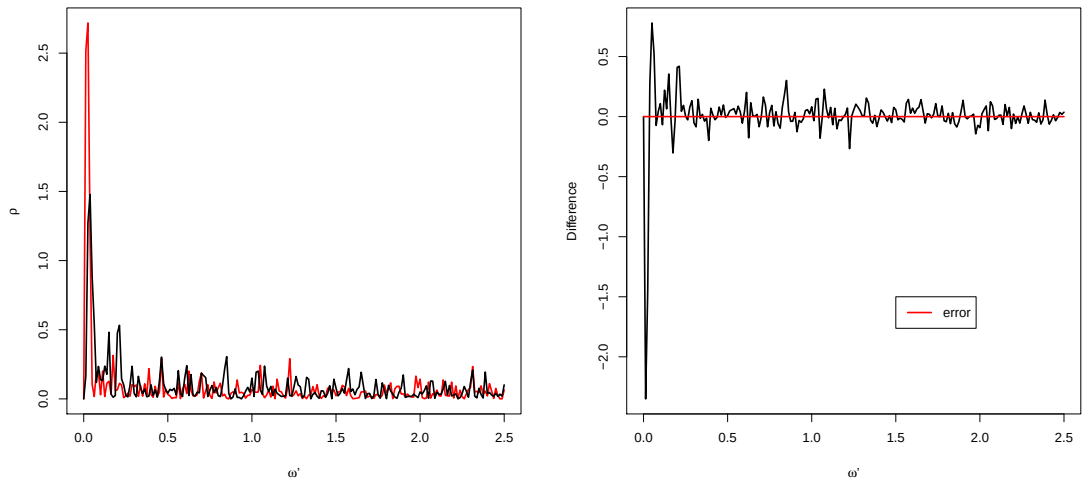

Figure 4.18: Left: The spectral density as a function of ω'. The red line represents the results with radiation terms included and the black line without. Right: The difference in spectral density, as a function of ω', with and without RR ($\rho_{noRR} - \rho_{RR}$). ($\phi = 0$, $\theta = \pi/4$ and $a_0 = 100$).

and a plot of the difference (result without RR - result with RR), shown in the right hand panel of Figure 4.18, seems to support this view. There is no obvious relationship between the spectral density with and without RR, in fact the difference plot appears completely random. The plot does however seem to show a larger difference for values of ω' that are closer to zero. If the spectrum becomes chaotic when RR is accounted for then this could

explain why there does not appear to be any clear structure when looking at the difference as a function of ω'.

The most obvious cause for these seemingly random oscillations would be random noise caused by numerical instability, after all, the integrals are all being evaluated numerically. Improving the accuracy of the numerical integration (achieved by decreasing the step sizes used in the algorithm), we find that the method does produce stable results. The errors, which are defined by the difference in results using the two levels of accuracy, are smaller than the actual values concerned. Figure 4.18 (right) shows the error values relative to the oscillating results. Compared with the actual results, the errors are small enough to be considered as zero and do not account for the fluctuations shown.

Another possible explanation for the chaos-like oscillations is related to the limits of integration. The definition of ρ involves integrating over infinite limits. This is not possible numerically and so instead the limits $[0, 100]$ were chosen since the laser field disappears outside of this range. As a check to see whether in fact there was any radiation outside of this range that had been ignored, we increased the range of τ over which we integrate. There was no change, which was to be expected given that there is no acceleration outside of the chosen range and hence no radiation.

Having looked at these possible sources of error and ruled out these numerical issues, we can now look for chaos. We use the widely accepted signature for chaotic behaviour, 'sensitive dependence on initial condition' [80], to decide whether there is evidence of chaos in the spectrum. We will investigate whether the spectrum of radiation becomes chaotic at some critical value of a_0. If the behaviour identified is indeed chaotic, this would be seen in the trajectory since the calculation of the spectral density is essentially just integration over the velocity and trajectory of the particle.

As a consequence of the conditions for chaos, a slight change in initial conditions leads to a very different outcome. To decide whether or not we have chaos, we consider the velocity four-vector. If we consider the velocity of the particle over all τ and then adjust the initial values very slightly we would expect the velocity to change very slightly unless the behaviour of the particle was chaotic, in which case this small change would result

in a completely different velocity. Let the vector u^μ and v^μ represent the velocity four-vectors for a particle with gamma factor $\gamma_0 = 1$ and $\gamma_0 = 1+\varepsilon$ respectively. For these given vectors we will take a measure of the difference in velocity four-vector defined by

$$D = \frac{1}{2T}\int_{-T}^{T} d\tau (u_\mu - v_\mu)^2 \tag{4.37}$$

We expect D to be of order ε and therefore if the velocity becomes chaotic after some critical value, we will see D increasing after this point. Choosing $\varepsilon = 10^{-2}$ (numerical error for integration $\ll \varepsilon$) and considering τ in the range $[0, 100]$, the difference is actually constant $D = 2.0 \times 10^{-2}$, of order ε as expected for non-chaotic behaviour. The test for chaos was repeated for the case where RR was included; again looking at D we see the same value obtained as when radiation was ignored.

If we instead measure our difference D by the difference between the spectral density, ρ, when $\gamma_0 = 1$ and when $\gamma_0 = 1+\varepsilon$:

$$D = \rho_{\gamma_0=1} - \rho_{\gamma_0=1+\varepsilon}\ , \tag{4.38}$$

we may determine the actual change in the spectral density for a small change in initial velocity. Again choosing $\varepsilon = 10^{-2}$ from Figure 4.19 we see that D is of order ε, thus supporting the argument above. Therefore despite the seemingly random behaviour of the spectrum we find the results are in fact stable, just highly oscillating. For large a_0 our spectral density plots have 'quasicontinuous' character [22] sharing the qualitative features shown in the quasiperiodic spectrum of Figure 10 in [81]. We shall later remove these fluctuations by integrating ρ over the angles.

4.3.3.2 Signatures of Radiation Reaction

Having established that the results are stable, to see where the largest differences between results with and without radiative damping lie, it is useful to look at a contour plot of the spectral density for a larger range of ω' values and θ values. We choose to use fixed $\phi = 0$ since this is where we saw the biggest disagreement between with and without radiative

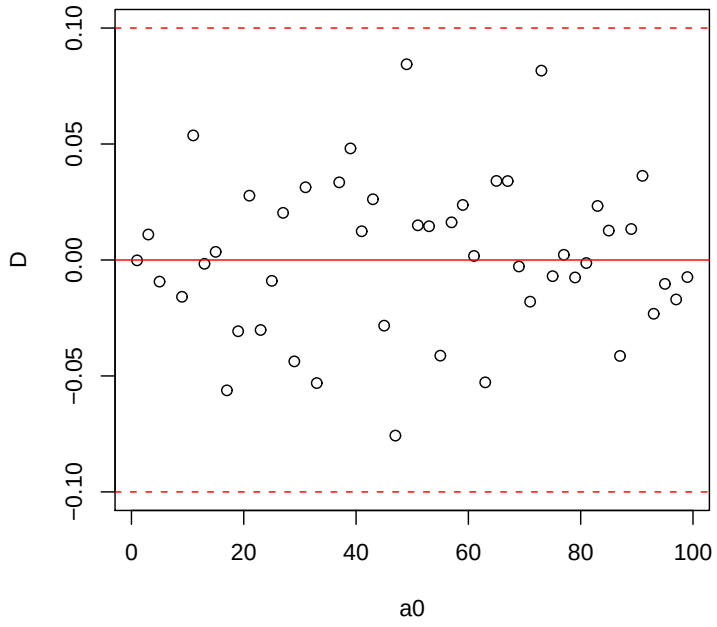

Figure 4.19: The difference between the spectral density when $\gamma_0 = 1$ and when $\gamma_0 = 1+\varepsilon$ as measured by D, Eq. (4.38), as a function of a_0 ($\omega' = 1$, $\theta = \pi/2$, $\phi = 0$).

terms in Figure 4.16. Due to the highly oscillatory nature of the spectrum, using a high resolution for the plots will allow us to see more of the structure of the spectrum.

Using contour plots to represent the spectral density also allows us to compare the changing structure as the laser intensity is increased. Figures 4.20 to 4.23 were produced with the aid of parallel programming using the high performance computing (HPC) facility at the University of Plymouth. The structure of the spectrum for $a_0 = 0.1, 1, 10, 20$ is shown, all neglecting the radiation terms. We see the common feature of the primary peak at $\omega' = 1$ and an introduction of smaller peaks as the strength parameter is increased. We compare these plots to Figure 4 in [82], which shows these same qualitative features. The plots with radiation terms included are very similar to the contour plots without the RR terms, so instead of reproducing these plots, in order to see more clearly where the differences lie we plot the difference in spectral density, $\rho_{noRR} - \rho_{RR}$. Results are shown in Figures 4.24 and 4.25 (Note that although the scale in Figure 4.25 is limited to ± 0.7 so that the structure can be seen more clearly, the largest difference when $a_0 = 20$ is approximately -70). From these difference plots, we can see that the differences seem to

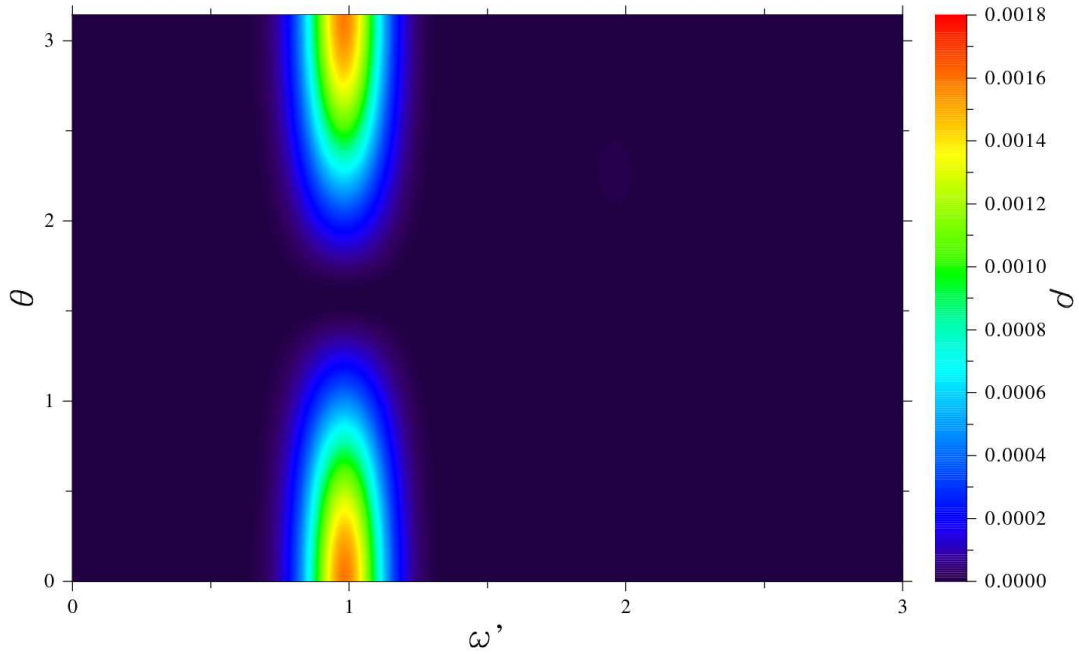

Figure 4.20: Contour plot showing the spectral density for $a_0 = 0.1$ as we vary θ and ω' ($\phi = 0$).

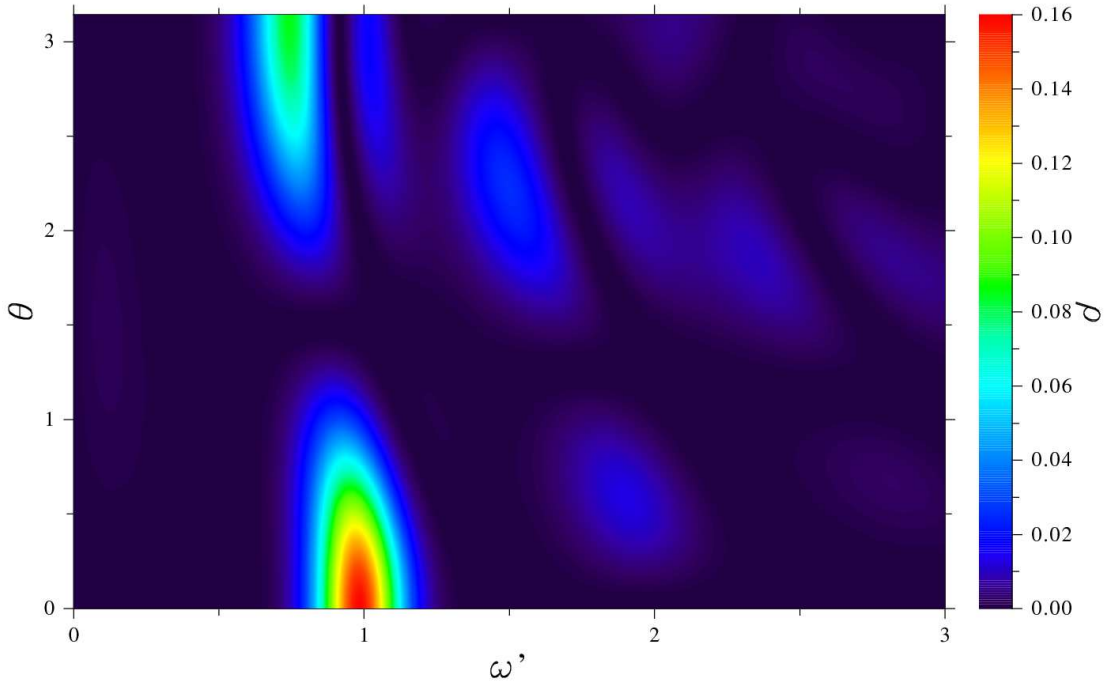

Figure 4.21: Contour plot showing the spectral density for $a_0 = 1$ as we vary θ and ω' ($\phi = 0$).

occur in bands, which gives the impression of a shift effect of the RR. A shift towards the lower frequencies is observed in [23] when RR is included. The differences oscillate from positive to negative and it is not clear from the plots whether there is an overall difference. If we calculate the average difference in the region considered we get a negative result in

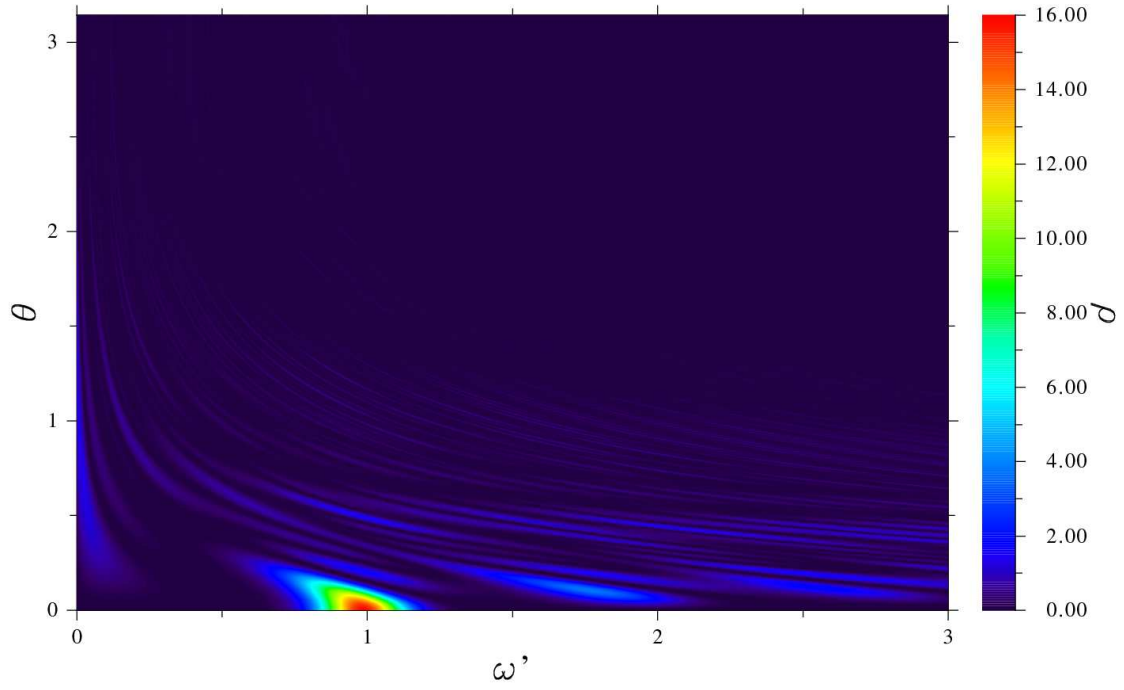

Figure 4.22: Contour plot showing the spectral density for $a_0 = 10$ as we vary θ and ω' ($\phi = 0$).

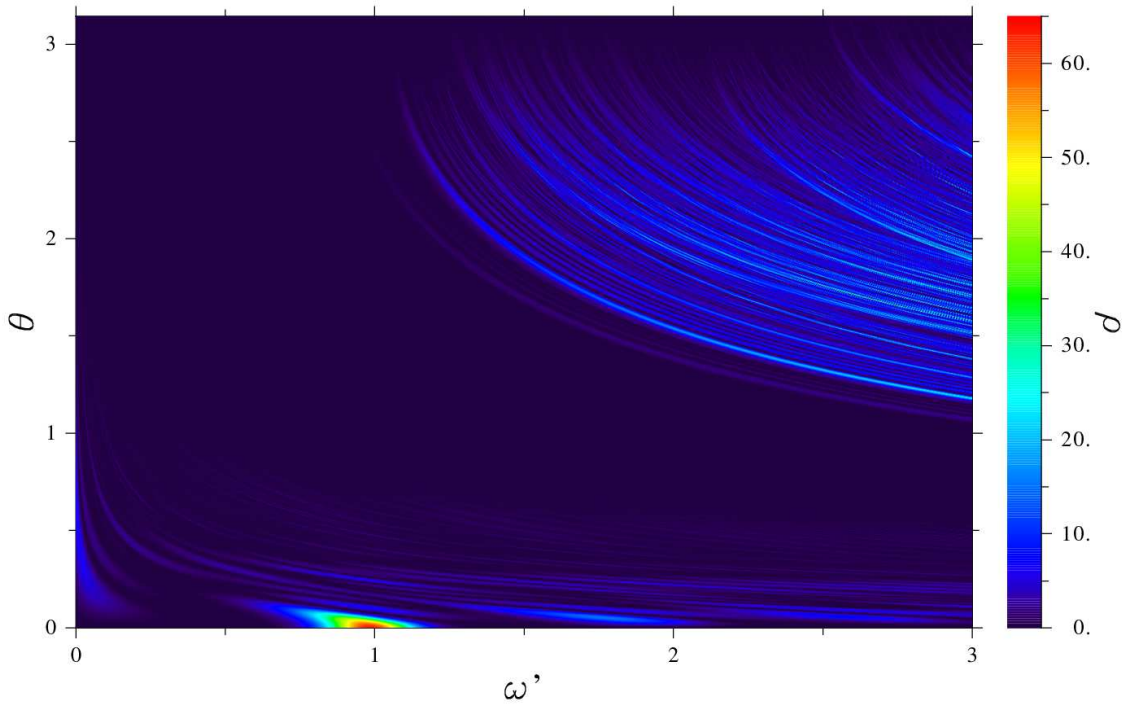

Figure 4.23: Contour plot showing the spectral density for $a_0 = 20$ as we vary θ and ω' ($\phi = 0$).

both cases implying that RR gives more radiation than if this effect was not present. A summary of the differences in shown in Table 4.1. We see that the biggest differences tend to occur when ω' is larger. This is in agreement with the results shown in [23]. The

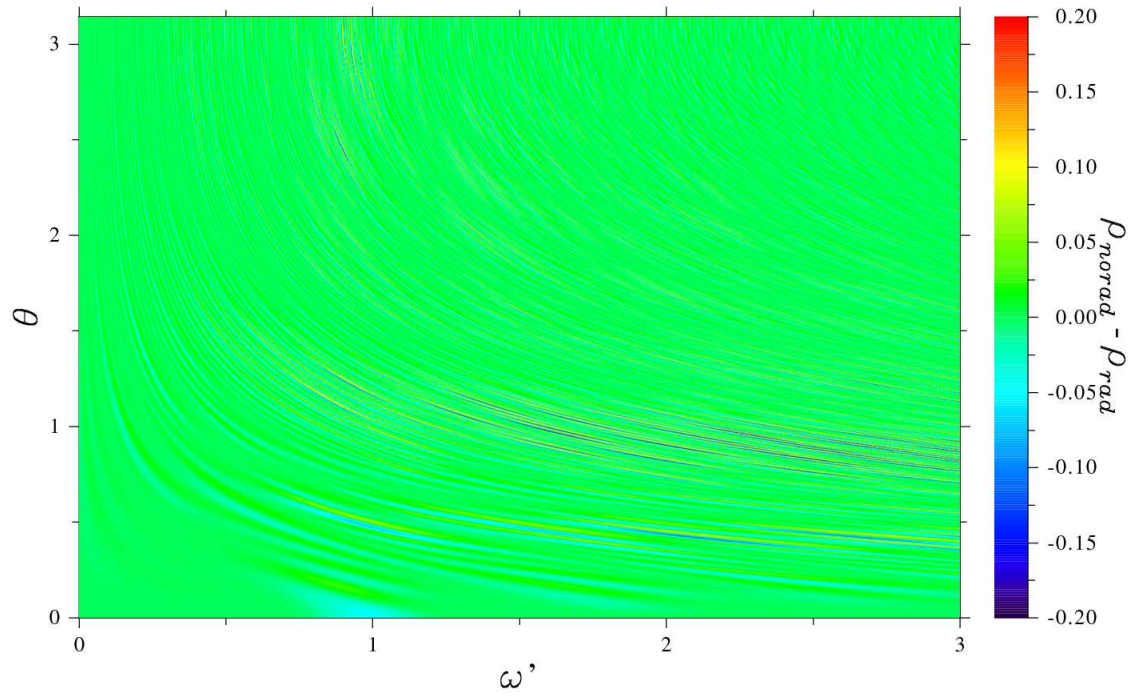

Figure 4.24: Difference in spectral density, $\rho_{noRR} - \rho_{RR}$, for $a_0 = 10$ for varying θ and ω' ($\phi = 0$).

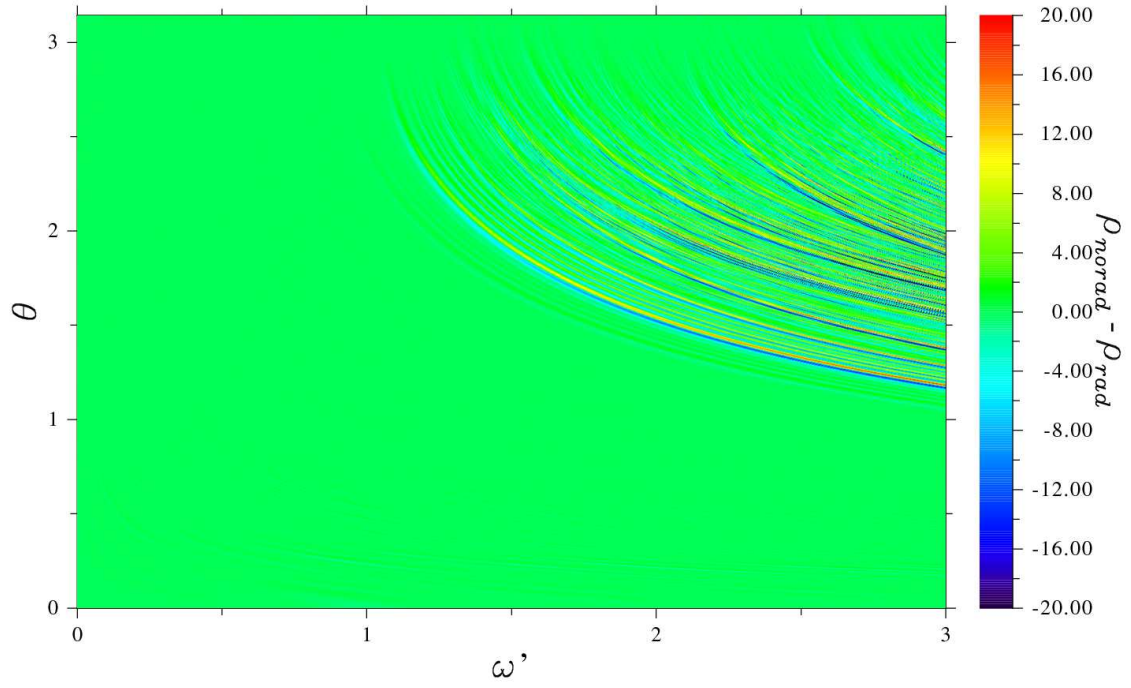

Figure 4.25: Difference in spectral density, $\rho_{noRR} - \rho_{RR}$, for $a_0 = 20$ for varying θ and ω' ($\phi = 0$).

angle of largest difference seems to shift for different a_0, for $a_0 = 10$ we find the maximum difference occurs around $\pi/4$ whereas for $a_0 = 20$ the maximum difference occurs closer to $\pi/2$.

In order to look for the overall effect of RR, the spectrum integrated over both angles

Table 4.1: Summary of differences ($\rho_{noRR} - \rho_{RR}$) in spectral density for $a_0 = 10$ and $a_0 = 20$. This table contains the maximum and minimum differences, the choice of parameters for which these maxima and minima occur (which.max / which.min), the sum of the differences and the average of the differences over the range shown in Figures 4.24 and 4.25 ($\phi = 0$).

	$a_0 = 10$	$a_0 = 20$
maximum	0.221	55.7
minimum	-0.207	-70.7
which.max	$\omega' = 2.997$, $\theta = 0.877$	$\omega' = 2.673$, $\theta = 1.69$
which.min	$\omega' = 2.988$, $\theta = 0.873$	$\omega' = 2.943$, $\theta = 1.78$
sum	-217.1	-44127.3
average	-0.000217	-0.0441

will be calculated. This should magnify its impact as well as smooth out some of the oscillations that occur in the spectrum for large a_0. We begin with small a_0 values and start by integrating over ϕ since there are less oscillations in the spectrum as we vary this angle and hence less calculations are required for accurate integration over ϕ than over θ. Integrating the function again with respect to θ we produce the spectrum over all angles as a function of frequency. Results for $a_0 = 1$ and $a_0 = 2$ are shown in Figure 4.26. We see that the basic shape is similar with a large peak where the frequency is just less than $\omega' = 1$. The plot for $a_0 = 2$ shows a few more oscillations than for $a_0 = 1$ and also the number of photons radiated is higher for the larger laser strength.

Figure 4.27 is the spectrum integrated over all angles as a function of ω' when we choose $a_0 = 10$. We again find similarities in the overall shape, for example the peak around $\omega' = 1$ and decrease in radiation for higher frequencies. We also get a large amount of radiation for frequencies close to zero; there was a slight increase from $a_0 = 1$ to $a_0 = 2$ in the radiation for these smaller frequencies although nowhere near as large as what we find for $a_0 = 10$. As expected the number of radiated photons is increased for this larger laser strength. As predicted, integration over the angles seems to have smoothed out the oscillatory behaviour. Comparing the results with and without RR we find that there is little difference between the two results, not visible from the plot in Figure 4.27, but this is not surprising given our earlier results for $a_0 = 10$. However, if we now plot the

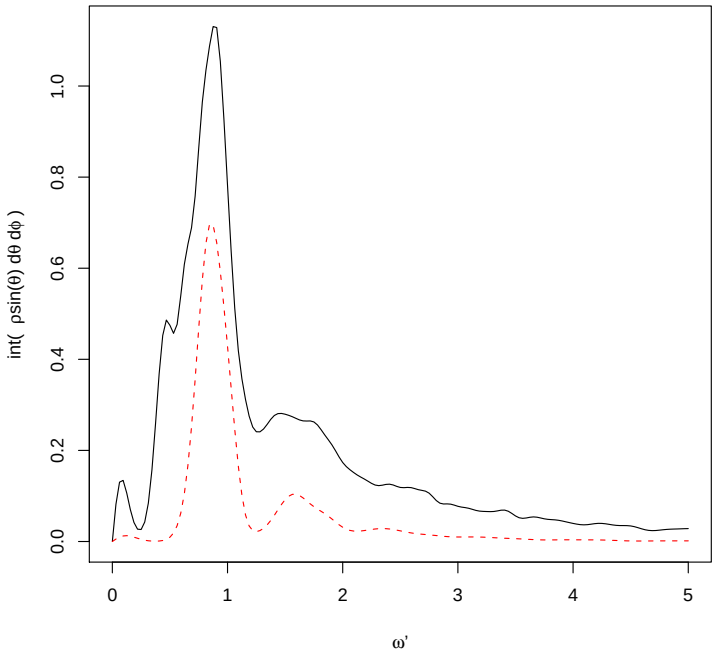

Figure 4.26: Spectrum of radiation integrated over all angles for varying ω'. Red dashed line represents $a_0 = 1$, and Black solid line $a_0 = 2$.

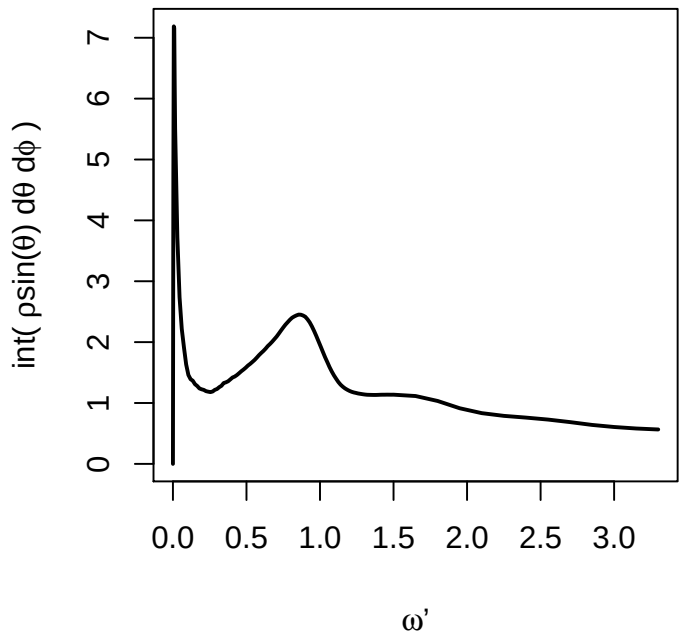

Figure 4.27: Spectrum of radiation integrated over all angles for varying ω' when $a_0 = 10$.

difference as a function of the frequency (see Figure 4.28) we find that there is a difference (larger than the numerical error). Despite no obvious pattern in the difference plot, we see on average that the difference, without RR - with RR, is negative. This indicates that the overall number of radiated photons is larger in the case where RR is accounted for. Although we would not expect to be able to easily detect such a small difference for an

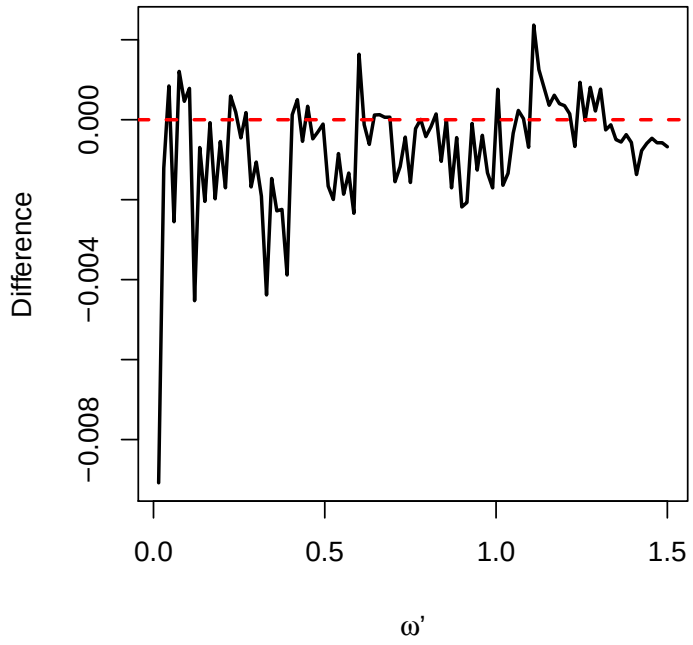

Figure 4.28: Difference between spectrum of radiation integrated over all angles for varying ω' when $a_0 = 10$ without RR - with RR ($\nu_0 = 10^{-3}$).

intensity of this magnitude, it suggests that for higher intensities there would be more radiation detected than expected when RR effects are ignored. The overall amplitude of the spectra is larger when we account for RR due to the energy gain of the electron from the radiation field. In the case of no RR the electron does not gain (or lose) energy and so continues to radiate at the initial energy [23]. However in the case when there is RR the electron, which begins initially at rest, radiates while continually gaining energy.

In this chapter we have observed the spectrum of radiation for crossed fields and for a pulsed plane wave. In our analytic investigation of the spectral density for crossed fields we were able to determine the impact of the initial gamma factor on the spectrum. We

saw that for larger initial values we got more radiation. A shift towards higher scattering frequencies was also observed for larger γ_0. It was also possible to explore the effect of the duration of the field when we numerically calculated the spectrum for crossed fields of finite duration. For increased duration we saw that the spectrum was red shifted, but also that there was more radiation emitted for the longer durations. When exploring the spectrum for the pulsed plane wave we were able to study the impact of a_0 on the spectrum. If $a_0 \gg 1$, the harmonics dominate the spectrum [83]. In particular we were interested in the RR effects. Since the radiation spectrum provides a sensitive way of revealing RR [79] we compared the spectrum with and without radiative terms included. Overall we found an increase in emitted radiation when RR was accounted for due to the energy gain of the electron from the radiation field.

Chapter 5

Conclusions and Outlook

Since its invention in 1960, the laser has come a long way. Lasers have developed rapidly, now used worldwide in areas from entertainment to fundamental science. With lasers now able to accelerate particles close to the speed of light and with plans for further increases in laser intensity, the theory behind laser matter interactions has required some attention. This thesis sought to simulate the interaction of these intense lasers with charged particles, taking into account the relativistic nature of these interactions. In particular we wished to determine the impact of radiation reaction (RR) on the behaviour of electrons in high-intensity laser beams, a topic that has received much attention due to the continuing advances in laser technology. We also looked to find an effective mechanism for vacuum laser acceleration for a particle initially at rest. The use of lasers as table-top particle accelerators has been an area of great interest since the intensities now achievable by modern lasers have continued to rise. These developments have seen a renewed interest in Thomson scattering, a process which becomes nonlinear when intensities exceed the relativistic threshold. We looked to the scattered radiation spectrum as a way of detecting evidence of RR.

5.1 Summary

We used a pulsed plane wave model to simulate our laser field, chosen since it provided a reasonable description of the laser field and still allowed us to solve the Landau-Lifshitz (LL) equation analytically. This choice was therefore useful in providing a benchmark

for our numerical calculations. We began by laying the groundwork for our investigations, first considering Maxwell's equations and the Lorentz force law in their familiar 3-dimensional notation and then rederiving them using a convenient covariant formalism. We looked at the power radiated and saw that it was proportional to the acceleration squared. Having established this link between acceleration of charges and emitted electromagnetic radiation, we explored the impact that this has on the equations of motion. For high intensities RR needs to be included. The inclusion of radiation terms in the equations of motion has a long history with issues arising such as runaway solutions and preacceleration in the Lorentz-Abraham-Dirac (LAD) equation. The LL equation provided us with a good solution to such problems.

A novel numerical scheme was introduced, which can be used to solve the equations of motion for arbitrary field configurations. The method was thoroughly tested and as well as being exact for constant fields maintains explicit covariance; in particular, it precisely preserves the on-shell condition. Some of the conventional finite difference schemes can introduce discretisation errors that lead to Lorentz violations. In addition, the method can include the radiative back-reaction on the particle motion. The LL equation was therefore solved analytically and numerically to find the trajectory and the velocity of an electron in the laser field. Comparing the numerical results to the analytic solution for a pulsed plane wave, the errors were seen to scale as expected for a first order method. The method was extended to a fourth order method and the errors scaled accordingly. The higher order method was shown to be extremely accurate even for a large discretisation step size.

We successfully identified differences in the particle motion when RR was accounted for. For a particle initially at rest in a pulsed plane wave, a charged particle is accelerated by the external field. The particle radiates so we see a larger gamma factor when RR is accounted for. We note however that this is not the case for a head-on collision of an electron and laser beam [31]. Our results showed that radiation reaction plays an important role for an optical laser with $a_0 = 3 \times 10^3$, but is negligible for an XFEL with $a_0 = 10$.

Armed with our method of solution to the equations of motion and a general model for our

laser pulse we went on to look at the idea of accelerating a charge using a laser in vacuum. Despite concerns that acceleration in vacuum could not provide substantial energy gain, we reviewed examples in the literature of possible methods of vacuum laser acceleration. We found that if we wanted a net energy gain we would require a unipolar pulse. We were able to identify the important parameters in vacuum laser acceleration - the phase shift and the pulse width. We found that without a carrier phase the pulse had a zero average field. For a nonzero average field we observed a nonzero final velocity, but for a zero average field there is no net acceleration. It was also shown how staging a series of laser pulses could magnify the effects of these unipolar pulses to give even larger energy gains. Our investigation into short pulse acceleration indicated that if we were to use an incomplete cycle, the average field would be non zero, hence allowing a net acceleration. The half-cycle pulse provided an upper limit to the potential energy gain achievable using subcycle acceleration.

A search for an optimum pulse shape indicated that a beat-like structure was effective in providing a net acceleration. We therefore proceeded to investigate the two-colour laser, where two copropagating lasers of differing frequencies are superimposed to a form an effective overall pulse profile. The overall pulse profile exhibits the beat wave structure found in our shape function search. By using a choice of frequency $\omega_2 = \omega_1/16$ we saw the charge leaving with close to peak energy, the type of energy gain expected when separating the electron from the laser before it decelerates. The two-colour laser gave a similar pulse profile to the $\cos^2$ pulse, which again provided an upper limit to potential gains, this time when larger values of N are used. The two-colour laser for an optimum choice of frequency difference showed highly significant energy gains, suggesting that there may be potential for vacuum laser acceleration to compete with plasma laser acceleration. Our study into vacuum laser acceleration also showed further evidence of the impact of RR. The electron achieves a net acceleration much larger than we would expect if the RR terms are neglected. We therefore underestimate the net acceleration when we ignore the effects of RR.

The effect of RR was also observed when we studied the spectrum of radiation. We

initially carried out an analytic investigation based on the radiation in crossed fields. Here we observed the effect of the initial gamma factor on the spectrum. We saw that for larger initial values we got more radiation and a shift towards higher scattering frequencies. We observed soft and collinear divergence when we looked at forward scattering. A numerical study of the crossed fields for the more physical scenario of the fields with finite duration allowed us to explore the effect of changing the duration, T. For increasing T we saw that the spectrum was red shifted and the overall emitted radiation was higher.

We then went on to explore the spectrum of radiation for our original plane wave with Gaussian envelope. We used this to study the impact of intensity on the spectrum. For large a_0 we observed increased oscillations. Despite the chaotic like fluctuations however, we did not find evidence of chaos in the particle trajectory. We compared the spectrum with and without radiative terms included. For forward scattering we saw a significant effect of RR for $a_0 = 3 \times 10^3$, with RR increasing the amount of radiation. Using parallel programming, we were able to look at contour plots of the difference with and without RR for $a_0 = 10$ and $a_0 = 20$; we noticed a shift effect of RR. When observing the spectrum over all angles for $a_0 = 10$ we found an increase in emitted radiation when RR was accounted for due to the energy gain of the electron from the radiation field.

The effect of RR was seen consistently throughout Chapters 2-4; we saw that for a charged particle initially at rest, when accelerated the charge gains energy from the radiation fields.

5.2 Outlook

Up to now the laser has been modelled by a plane wave $\mathbf{E}(k\cdot x)$, a null-field that is infinite in transverse directions. Now we have established a strong method of solution for the equations of motion we may apply it to more complex field configurations. Standing waves could be considered,

$$\mathbf{E}\left(k\cdot x\right)+\mathbf{E}\left(\bar{k}\cdot x\right), \quad k=(k_0,\mathbf{k}),\ \bar{k}=(k^0,-\mathbf{k})\ . \tag{5.1}$$

In the case of standing waves, which do not correspond to null-fields, there is no analytic solution available and so numerical methods must be used here. This alternative model is still infinite in the *x*-*y* plane, when in reality the laser beam is finite. For a more realistic model of a laser beam that is finite in transverse directions, we could look at Gaussian beams; this has been explored by Narozhny and Fofanov [25, 26].

We made the assumption in our work with the pulsed plane wave model that the electron only interacts with the centre of the laser focus. We mentioned in Section 1.2 that if we use Gaussian functions to model our laser beam we obtain plane wave fields in the limit where the beam waist becomes large. However if an electron beam radius is no longer narrow compared to the laser waist size, the transverse size effects become important. The pondermotive force trying to move electrons from the beam centre was shown in [70] to lead to measurable effects only for a very small beam radius. It would be interesting to investigate whether our results for the acceleration of charged particles from rest still hold for Gaussian beams with a small waist size. Using a more realistic model, we could also verify our results on the impact of RR.

Our work on the spectrum of radiation could also be developed in a few different ways. It would be useful to extend the work done for $a_0 = 10$ on the spectrum over all angles, to higher a_0 values where the impact of RR has been seen to be more significant. Problems arise with the oscillatory behaviour of the spectrum, but if the numerical method were developed to overcome such issues, the total spectrum for large a_0 could be investigated. It would also be useful to provide an exact comparison of the analytic and numerical approaches for the spectral density for constant fields. Using a bounded trajectory such as circular motion, for which the analytic result for the spectrum can be calculated, this kind of comparison would be possible.

As laser intensities continue to rise quantum effects may also become apparent. Differences between classical and quantum results for an intense laser pulse are investigated by Boca and Florescu in [84] when RR is neglected. It would be interesting to compare the results from our spectra, which include radiative effects, with nonlinear Compton scattering. A closely related idea is to identify signatures of quantum radiation reaction in

Compton scattering spectra [85].

Once we have a realistic model for the laser beam, the numerical model can be extended to look at multi-particle scattering. One option would be to develop cascade codes using high performance computers to look at how particles behave with realistic beams when they are able to interact with each other. This can incorporate Compton scattering and pair production [86] for example, and could be used for determining the energy gained from laser beams.

This thesis has provided the tools needed to simulate relativistic laser matter interactions, promising results in the application of these interactions, and a way to detect differences occurring during the interactions when RR effects become significant. There are still developments that can be made to our simulations, but much of the content in this thesis may be used as a basis for future work in this exciting and ever evolving area of physics.

List of references

[1] A. Einstein, "On the Quantum Mechanics of Radiation," *Phys. Z.* **18** (1917) 121–128.

[2] Encyclopedia of Laser Physics and Technology. http://www.rp-photonics.com/stimulated_emission.html.

[3] The Council for Scientific and Industrial Research (CSIR) in South Africa. http://www.csir.co.za/lasers/basics_of_lasers.html.

[4] The Central Laser Facility (CLF) website. http://www.clf.stfc.ac.uk.

[5] The Engineering and Physical Sciences Research Council (EPSRC) website. http://www.epsrc.ac.uk.

[6] Y. I. Salamin, S. Hu, K. Z. Hatsagortsyan, and C. H. Keitel, "Relativistic high-power laser-matter interactions," *Phys. Rept.* **427** (2006) 41–155.

[7] R. T. Hammond, "Relativistic Particle Motion and Radiation Reaction in Electrodynamics," *EJTP* **7** no. 23, (2010) 221–258.

[8] K. P. Singh, "Laser induced electron acceleration in vacuum," *Phys. Plasmas* **11** (2004) 1164.

[9] V. Marceau, A. April, and M. Piche, "Electron acceleration driven by ultrashort and nonparaxial radially polarized laser pulses," arXiv:1204.5726 [physics.acc-ph].

[10] X. Ding, L. Shao, D. Cline, I. Pogorelsky, K. Kusche, M. Fedurin, V. Yakimenko, Y.K. Ho, Q. Kong, and J. J. Xu, "Vacuum laser acceleration experiment perspective at brookhaven national lab-accelerator test facility," in *Proceedings of IPAC2012*, pp. 2735–2737. 2012.

[11] Y. Y. Lau, F. He, D. P. Umstadter, and R. Kowalczyk, "Nonlinear Thomson scattering: A tutorial," *Phys. Plasmas* **10** no. 5, (2003) 2155–2162. http://link.aip.org/link/?PHP/10/2155/1.

[12] S. Y. Chen, A. Maksimchuk, and D. Umstader, "Experimental observation of relativistic nonlinear Thomson scattering," *Nature* **396** (1998) 653–655.

[13] T. Z. Esirkepov and S. Bulanov, "Fundamental Physics and Relativistic Laboratory Astrophysics with Extreme Power Lasers," `arXiv:1202.4552 [astro-ph.HE]`.

[14] A. Einstein, "On the electrodynamics of moving bodies," *Annalen Phys.* **17** (1905) 891–921.

[15] H. A. Lorentz, *The Theory of Electrons*. B.G. Teubner, Leipzig, 1906; reprinted by Dover Publications, New York, 1952 and Cosimo, New York, 2007.

[16] M. Abraham, *Theorie der Elektrizität*. Teubner, Leipzig, 1905.

[17] P. A. M. Dirac, "Classical Theory of Radiating Electrons," *Proc. Roy. Soc. A* **167** (1938) 148–169.

[18] H. Spohn, *Dynamics of Charged Particles and their Radiation Field*. Cambridge University Press, Cambridge, 1905.

[19] F. Rohrlich, *Classical Charged Particles*. World Scientific, Singapore, 3rd ed., 2007.

[20] G. Ares de Parga, R. Mares, and S. Dominguez, "An unphysical result for the Landau-Lifshitz equation of motion for a charged particle," *Revista Mex. Fisica* **52** (2006) 139–142.

[21] H. Spohn, "The Critical manifold of the Lorentz-Dirac equation," *Europhys. Lett.* **49** (2000) 287.

[22] L. D. Landau and E. M. Lifshitz, *The Classical Theory of Fields (Course of Theoretical Physics, Vol. 2)*. Butterworth-Heinemann, Oxford, 1987.

[23] J. Koga, T. Z. Esirkepov, and S. V. Bulanov, "Nonlinear Thomson scattering in the strong radiation damping regime," *Phys. Plasmas* **12** (2005) 093106.

[24] C. Harvey and M. Marklund, "Radiation damping in pulsed Gaussian beams," *Phys. Rev. A* **85** (2012) 013412. `http://link.aps.org/doi/10.1103/PhysRevA.85.013412`.

[25] N. B. Narozhny and M. S. Fofanov, "Scattering of relativistic electrons by a focused laser pulse," *JETP* **90** (2000) 753–768.

[26] N. B. Narozhny and M. S. Fofanov, "Anisotropy of electrons accelerated by a high-intensity laser pulse," *Phys. Lett. A* **295** (2002) 87–91.

[27] V. Yanovsky, V. Chvykov, G. Kalinchenko, P. Rousseau, T. Planchon, T. Matsuoka, A. Maksimchuk, J. Nees, G. Cheriaux, G. Mourou, and K. Krushelnick, "Ultra-high intensity- 300-TW laser at 0.1 Hz repetition rate," *Optics Express* **16** (2008) 2109.

[28] S. Bulanov. Private communication, 2012.

[29] S. Coleman, *Electromagnetism, Paths to Research*. Plenum, New York, 1982. ed. Teplitz, D.

[30] J. D. Jackson, *Classical Electrodynamics*. John Wiley & Sons, New York, 3rd ed., 1998.

[31] C. Harvey, T. Heinzl, and M. Marklund, "Symmetry breaking from radiation reaction in ultra-intense laser fields," *Phys. Rev. D* **84** (2011) 116005, arXiv:1110.0628 [physics.class-ph].

[32] R. M. Wald, *General Relativity*. University of Chicago Press, 1984.

[33] A. Di Piazza, "Exact solution of the Landau-Lifshitz equation in a plane wave," *Lett. Math. Phys.* **83** (2008) 305.

[34] C. Harvey, T. Heinzl, N. Iji, and K. Langfeld, "Covariant Worldline Numerics for Charge Motion with Radiation Reaction," *Phys. Rev. D* **83** (2011) 076013, arXiv:1012.3082 [physics.class-ph].

[35] A. H. Taub, "Orbits of charged particles in constant fields," *Phys. Rev.* **73** (1948) 786–798. http://link.aps.org/doi/10.1103/PhysRev.73.786.

[36] C. Itzykson and J. B. Zuber, *Quantum Field Theory*. Dover, New York, 2005.

[37] Y. Hadad, L. Labun, J. Rafelski, N. Elkina, C. Klier, *et al.*, "Effects of Radiation-Reaction in Relativistic Laser Acceleration," *Phys. Rev. D* **82** (2010) 096012, arXiv:1005.3980 [hep-ph].

[38] E. Esarey, P. Sprangle, and J. Krall, "Laser acceleration of electrons in vacuum," *Phys. Rev. E* **52** (1995) 5443–5453.

[39] A. Troha, J. Van Meter, E. Landahl, R. Alvis, K. Li, *et al.*, "Vacuum electron acceleration by coherent dipole radiation," *Phys. Rev. E* **60** (1999) 926–934.

[40] J. Wang, W. Scheid, M. Hoelss, and Y. Ho, "Comment on 'Vacuum electron acceleration by coherent dipole radiation'," *Phys. Rev. E* **65** (2002) 028501.

[41] A. Troha and F. Hartemann, "Reply to comment on 'Vacuum electron acceleration by coherent dipole radiation'," *Phys. Rev. E* **65** (2002) 028502.

[42] P. Bucksbaum, M. Bashkansky, and T. McIlrath, "Scattering of electrons by intense coherent light," *Phys. Rev. Lett.* **58** (1987) 349–352.

[43] J. Hus, T. C. Katsouleas, W. Mori, C. Schroeder, and J. Wurtele, "Laser acceleration in vacuum," *Conf. Proc.* **C970512** (1997) 684–686.

[44] F. Wang, B. Shen, X. Zhang, X. Li, and Z. Jin, "Electron acceleration by a propagating laser pulse in vacuum," *Phys. Plasmas* **14** no. 8, (2007) 083102. http://link.aip.org/link/?PHP/14/083102/1.

[45] W. Scheid and H. Hora, "On electron acceleration by plane transverse electromagnetic pulses in vacuum," *Laser and Particle Beams* **7** no. 02, (1989) 315–332.

[46] V. Dinu, T. Heinzl, and A. Ilderton, "Infra-red divergences in plane wave backgrounds," arXiv:1206.3957 [hep-ph].

[47] H. Hojo, B. Rau, and T. Tajima, "Particle acceleration and coherent radiation by subcycle laser pulses," *Nucl. Instrum. Meth. A* **410** (1998) 509–513.

[48] M. P. Liu, H. C. Wu, B. S. Xie, and M. Y. Yu, "Electron acceleration in vacuum by subcycle laser pulse," *Phys. Plasmas* **15** no. 2, (2008) 023108. http://link.aip.org/link/?PHP/15/023108/1.

[49] T. Haeuser, W. Scheid, and H. Hora, "Acceleration of electrons by intense laser pulses in vacuum," *Phys. Lett. A* **186** (1994) 189–192.

[50] J. X. Wang, W. Scheid, M. Hoelss, and Y. K. Ho, "Electron acceleration by intense shock-like laser pulses in vacuum," *Phys. Lett. A* **275** (2000) 323–328.

[51] H. Malav, K. P. Maheshwari, and V. Senecha, "Analytical and numerical investigation of the effect of pulse shape of intense, few-cycles TM_{01} laser on the acceleration of charged paricles," *IJPAP* **49** no. 4, (2011) 251–256.

[52] D. H. Torchinsky, T. Feurer, and K. A. Nelson, "Electron acceleration through spatiotemporal shaping of ultrashort light pulses," in *Ultrafast Phenomena XIV*, vol. 79 of *Springer Series in Chemical Physics*, pp. 152–154. Springer Berlin Heidelberg, 2005. http://dx.doi.org/10.1007/3-540-27213-5_47.

[53] C. Harvey, T. Heinzl, A. Ilderton, and M. Marklund, "The intensity dependent mass shift: existence, universality and detection." 2012, arXiv:1203.6077 [hep-ph], to appear in Phys. Rev. Lett.

[54] D. N. Gupta and H. Suk, "Electron acceleration to high energy by using two chirped lasers," *Laser and Particle Beams* **25** no. 01, (2007) 31–36.

[55] Y. I. Salamin, "Electron acceleration from rest in vacuum by an axicon Gaussian laser beam," *Phys. Rev. A* **73** (2006) 043402.

[56] S. Takeuchi, "Electron acceleration by longitudinal electric field generated by colinearly overlapped two laser beams," in *AIP Conference Series*, vol. 369, pp. 695–700. 1996.

[57] W. Kimura, A. van Steenbergen, M. Babzien, I. Ben-Zvi, L. Campbell, *et al.*, "First staging of two laser accelerators," *Phys. Rev. Lett.* **86** (2001) 4041–4043.

[58] W. Kimura, L. Campbell, C. Dilley, S. Gottschalk, D. Quimby, *et al.*, "Detailed experimental results for laser acceleration staging," *Phys. Rev. ST Accel. Beams* **4** (2001) 101301.

[59] K. Sakai, S. Miyazaki, S. Hasumi, T. Kikuchi, and S. Kawata, "Electron Acceleration by a Focused Intense Short-Pulse TEM(1, 0) + TEM(0, 1) - Mode Laser in Vacuum," *Laser Physics* **15** no. 12, (2005) 1706–1709.

[60] W. H. Press, S. A. Teukolsky, W. T. Vetterling, and B. P. Flannery, *Numerical Recipes 3rd Edition: The Art of Scientific Computing*. Cambridge University Press, 3rd ed., 2007.

[61] Encyclopedia of Laser Physics and Technology. `http://www.rp-photonics.com/beat_note.html`.

[62] W. W. Hsiang, W. C. Chiao, C. Y. Wu, and Y. Lai, "Direct observation of two-color pulse dynamics in passively synchronized Er and Yb mode-locked fiber lasers," *Opt. Express* **19** no. 24, (2011) 24507–24515. `http://www.opticsexpress.org/abstract.cfm?URI=oe-19-24-24507`.

[63] Y. I. Salamin, "Electron acceleration in a tightly-focused vacuum laser beat wave," *Phys. Lett. A* **335** (2005) 289–294.

[64] B. Hafizi, A. Ting, E. Esarey, P. Sprangle, and J. Krall, "Vacuum beat wave acceleration," *Phys. Rev. E* **55** (1997) 5924–5933. `http://link.aps.org/doi/10.1103/PhysRevE.55.5924`.

[65] K.-J. Kim, K. T. McDonald, G. V. Stupakov, and M. S. Zolotorev, "A bounded source cannot emit a unipolar electromagnetic wave," *ArXiv Physics e-prints* (Mar., 2000) , `arXiv:physics/0003064`.

[66] G. Malka, E. Lefebvre, and J. L. Miquel, "Experimental Observation of Electrons Accelerated in Vacuum to Relativistic Energies by a High-Intensity Laser," *Phys. Rev. Lett.* **78** (Apr, 1997) 3314–3317. http://link.aps.org/doi/10.1103/PhysRevLett.78.3314.

[67] K. T. McDonald, "Comment on "Experimental Observation of Electrons Accelerated in Vacuum to Relativistic Energies by a High-Intensity Laser"," *Phys. Rev. Lett.* **80** (Feb, 1998) 1350–1350. http://link.aps.org/doi/10.1103/PhysRevLett.80.1350.

[68] Vachaspati, "Harmonics in the scattering of light by free electrons," *Phys. Rev.* **128** (1962) 664–666. http://link.aps.org/doi/10.1103/PhysRev.128.664.

[69] N. Sengupta, "On the scattering of electromagnetic waves by free electron-1 : Classical theory," *Bulletin of Cal. Math. Soc.* **41** no. 1, (1949) 187–198.

[70] T. Heinzl, D. Seipt, and B. Kampfer, "Beam-Shape Effects in Nonlinear Compton and Thomson Scattering," *Phys. Rev. A* **81** (2010) 022125, arXiv:0911.1622 [hep-ph].

[71] J. Schwinger, L. DeRaad, K. Milton, and W. Tsai, *Classical Electrodynamics*. Perseus Books, Massachusetts, 1998.

[72] P. J. Duke, *Synchrotron Radiation Production and Properties*. Oxford University Press, Oxford, 2000.

[73] G. Schott, *Electromagnetic Radiation and the Mechanical Reactions Arising from it*. Cambridge University Press, Cambridge, 1912.

[74] T. Heinzl, "Light cone quantization: Foundations and applications," *Lect. Notes Phys.* **572** (2001) 55–142, arXiv:hep-th/0008096 [hep-th].

[75] M. Abramowitz and I. A. Stegun, *Handbook of Mathematical Functions with Formulas, Graphs, and Mathematical Tables*. Dover, New York, ninth Dover printing, tenth GPO printing ed., 1964.

[76] C. A. Brau, "Oscillations in the spectrum of nonlinear Thomson-backscattered radiation," *Phys. Rev. ST Accel. Beams* **7** (2004) 020701. http://link.aps.org/doi/10.1103/PhysRevSTAB.7.020701.

[77] E. Esarey, S. K. Ride, and P. Sprangle, "Nonlinear Thomson scattering of intense laser pulses from beams and plasmas," *Phys. Rev. E* **48** (1993) 3003–3021.

[78] A. Thomas, "Algorithm for calculating spectral intensity due to charged particles in arbitrary motion," *Phys. Rev. ST Accel. Beams* **13** (2010) 020702, arXiv:0906.0758 [physics.comp-ph].

[79] C. H. Keitel, C. Szymanowski, P. L. Knight, and A. Maquet, "Radiative reaction in ultra-intense laser - atom interaction," *J. Phys. B* **31** no. 3, (1998) L75. http://stacks.iop.org/0953-4075/31/i=3/a=002.

[80] C. S. Poon, C. Li, and G. Q. Wu, "A unified theory of chaos linking nonlinear dynamics and statistical physics," *ArXiv e-prints* (2010) , arXiv:1004.1427 [nlin.CD].

[81] J. P. Eckmann and D. Ruelle, "Ergodic theory of chaos and strange attractors," *Rev. Mod. Phys.* **57** (1985) 617–656. http://link.aps.org/doi/10.1103/RevModPhys.57.617.

[82] A. Debus, S. Bock, M. Bussmann, T. E. Cowan, A. Jochmann, T. Kluge, S. D. Kraft, R. Sauerbrey, K. Zeil, and U. Schramm, "Linear and non-linear Thomson-scattering x-ray sources driven by conventionally and laser plasma accelerated electrons," in *SPIE Conference Series*, vol. 7359. 2009.

[83] S. K. Ride, E. Esarey, and M. Baine, "Thomson scattering of intense lasers from electron beams at arbitrary interaction angles," *Phys. Rev. E* **52** (1995) 5425–5442.

[84] M. Boca and V. Florescu, "Thomson and Compton scattering with an intense laser pulse," *EPJ D* **61** (2011) 449–462, arXiv:1110.4951 [physics.atom-ph].

[85] A. Di Piazza, K. Hatsagortsyan, and C. Keitel, "Quantum radiation reaction effects in multiphoton Compton scattering," *Phys. Rev. Lett.* **105** (2010) 220403, arXiv:1007.4914 [hep-ph].

[86] A. R. Bell and J. G. Kirk, "Possibility of prolific pair production with high-power lasers," *Phys. Rev. Lett.* **101** (2008) 200403. http://link.aps.org/doi/10.1103/PhysRevLett.101.200403.